ACCESSIBILITY
Open

MASTER THESIS 2010

SUBJECT AREA:	DATE: 14.06.2010	NO. OF PAGES:
Structural/Mechanical Engineering		10+112+18

TITLE:

Blast loading on square steel plates; A comparative study of numerical methods

Eksplosjonslast på kvadratiske stålplater; En sammenligning av numeriske metoder

BY:

Christian Mæhle Kaurin,
Magnus Olaf Varslot

SUMMARY:
During the recent years, several promising finite element solutions have been presented for finding the response of structures subjected to blast loading. This thesis gives as a comparative study on 3 major solution strategies, and their implication on the response on constrained plates of varying standoff distances. The strategies chosen are the Lagrangian method using load blast function in LS-DYNA, in which the plate nodes are subjected directly to forces attained from empirical ConWep data. The Arbitrary Lagrangian Eulerian (ALE) method in LS-DYNA, where an initial charge is detonated within an air medium and impulse transferred through contact algorithms. Finally a particle method, where air and soil are treated as discrete particles. This novel approach gives faster calculations than the ALE method and possible more reliable results than the Lagrangian method.

Dharmasena et.al (2009) performed experiments where final deflection of steel plates was recorded for a charge off constant mass with varying standoff distances. These results were used to validate the models.

It was found that the Lagrangian analysis provided conservative results at short standoff distances, and very accurate predictions at greater distances.

An ALE analysis was performed under the same assumptions. Even though the analysis gave accurate final deflections at short standoff distances, it was found to be giving increasing impulse with standoff distance, for fine meshes. This resulted in increasing final deflection with standoff distance, which was unsupported by experimental data.

Finally, a discrete particle method has been applied using the IMPETUS code. It gave the most accurate prediction in terms of final deflections. It was found to give almost equal results as the ALE analysis for short standoff distances, and equal results as the Lagrangian analysis for the longer stand off distances. The computational times were also greatly reduced compared to the ALE method.

RESPONSIBLE TEACHER: Tore Børvik

SUPERVISOR(S): Knut Gaarder Rakvåg, Tore Børvik and Odd Sture Hopperstad

CARRIED OUT AT: NTNU

Institutt for konstruksjonsteknikk

FAKULTET FOR INGENIØRVITENSKAP OG TEKNOLOGI

NTNU – Norges teknisk-naturvitenskapelige universitet

MASTEROPPGAVE 2010

for

Christian Kaurin og Magnus Varslot

Eksplosjonslast på kvadratiske stålplater; En sammenligning av numeriske metoder

Blast loading on square steel plates; A comparative study of numerical methods

Både sivile og militære beskyttelseskonstruksjoner kan usettes for kombinert fragment- og eksplosjonsbelastning. Fragmentene kan behandles som sand generert av miner. Fram til nå har man dimensjonert slike konstruksjoner uten å ta hensyn til den mulige interaksjonseffekten mellom lastene. Hensikten med denne oppgaven er å undersøke forskjellige numeriske metoder og analysere deres effekt på responsen til platekonstruksjoner. Først ønsker man å simulere effekten av eksplosjonslast alene, så effekten av sand alene. Med bakgrunn i analysene skal det foreslås løsningsstrategier for platekonstruksjoner ved rene eksplosjonsbelastninger og eksplosjoner med sand. Hensikten er å legge til rette for videre arbeid med kombinert lastvirkning. Analysene skal valideres opp mot eksisterende forsøksdata på plater i AL6XN rustfritt stål.

Oppgaven inneholder følgende aktiviteter:

1. Litteraturstudium: Eksplosjonslast; penetrasjon og perforering; fragmenter, ulike numeriske metoder og modeller; material- og bruddmodeller.
2. Materialforsøk: Det er utført noen materialforsøk på AL6061-T6. Disse skal studeres og aktuelle material- og bruddmodeller skal kalibreres. Det er og av interesse å gjøre dynamiske materialforsøk på AL6061. Materialdata for AL6XN finnes i litteraturen.
3. Komponentforsøk: Eksplosjonsforsøk både med og uten virkning av sand på de aktuelle materialene er allerede utført. Disse forsøkene skal beskrives og rapporteres i detalj.
4. Numeriske simuleringer: Komponentforsøkene skal modelleres i LS-DYNA (vha Lagrange-analyser og Lagrange/ALE-analyser) og i IMPETUS (vha en partikkelbasert metode). Simuleringer skal utføres og resultatene skal sammenlignes og valideres mot forsøksdata. Parameterstudier vha de ulike metodene skal gjennomføres.
5. Rapportering.

Besvarelsen organiseres i henhold til gjeldende retningslinjer.

Veileder(e): Knut Gaarder Rakvåg, Tore Børvik og Odd Sture Hopperstad

Besvarelsen skal leveres til Institutt for konstruksjonsteknikk innen 14. juni 2010.

NTNU, 24. januar, 2010

Tore Børvik, faglærer

Acknowledgements

There are plenty of easier subjects for a master thesis than numerical simulation of blast loading on structures. The last five months have indeed been very challenging, but at the same time very educational. The ALE method used in this thesis was found to be extremely complex and hard to calibrate for accurate blast loading. It certainly slowed down the progression of the thesis a great deal.

Contents

x

Chapter 1

Introduction and motivation

The motivation for this thesis is experiments performed on fully clamped square steel plates performed by Dharmasena et.al (2009) [9]. The plates were constructed of AL6XN steel, and exposed to blast loading from C4 at varying stand off distances. Three different test configurations were performed; test with bare charge, test with dry sand and test with wet sand.

Figure 1.1: Photo from experiment prior to detonation [9]

The main focus in this thesis, is to use the results from the bare charge and dry sand experiments to validate computational models utilized in blast load analysis. For this purpose three different methods will be used:

- The lagrangian LS-DYNA load blast function, where empirical pressure data from ConWep is applied as nodal forces.

- The Arbitrary Lagrangian Eulerian framework in LS-DYNA, where the explosive, air and resulting pressure wave are modeled within a mesh using a multi material element formulation. The impulse from the blast is then consequently imparted on the plate using a contact algorithm.

- The corpuscular method in the IMPETUS code, where the air and explosive are treated as perfectly elastic particles, and sand is treated according to a rheological model [12].

It was originally intended that this paper would consider blast on a honeycomb truss strucuture in alloy AL6061-T6. Material tests were therefore performed to determine the strain and strain-rate dependency, and was fitted for the Johnson Cook model. As it turned out, the neccecary blast experiments needed to validate the truss model was not performed. It is thus left for further investigation.

The thesis is separated into the following parts:

- **Chapter 2:** Brief summary of previous work in the study of blast loading on plates. Special emphasis is given to fluid structure interaction FSI effects and previous ALE blast studies.

- **Chapter 3:** Brief overview of the theory of explosions, pressure definitions, ground effects and structural response.

- **Chapter 4:** Theoretical study of the numerical methods used in this thesis, with main focus on the Arbitrary-Lagrangian-Eulerian ALE method.

- **Chapter 5:** Material testing, modelling, and Split Hopkinson test description.

- **Chapter 6:** Description of blast experiments done by Dharmasena et.al (2009).

- **Chapter 7:** Blast modelling using the Lagrangian method.

- **Chapter 8:** Blast modelling using the Arbitrary-Lagrangian-Eulerian method.

- **Chapter 9:** Discrete particle method using the IMPETUS code, for bare charge and charge surrounded by dry sand.

- **Chapter 10:** Comparison study, permanent central deflection and permanent state of deformation.

Chapter 2

Previous work

The early work of Taylor in the 1960's [34] showed that the transmitted impulse to a free standing plate could be signifcantly reduced through fluid structure iteraction FSI. This reduction, is caused by the plates moving relative to the fluid, and was found to be even more significant as the mass of the plate was reduced. Taylor derived a relation which expressed the relative transmitted impulse to a free standing plate as a function of the non dimensional FSI time scale. This parameter is computed as the relative ratio between the mass of the plate and the mass of the compressed gas volume. Since Taylors analysis was done assuming linear blast waves with exponential pressure functions and constant fluid density, its effects were effectively confined to underwater explosions where significant non linear compressional effects are not observed.

The theory of Taylor was extended by N. Kambouchev et.al [18] to consider the nonlinear compressibility which occurs during air blasts. In his extension the previously FSI time scale is given by the ratio of the plate mass and the product of the peak density, shock speed, and blast decay time, which leads to a compressible FSI nondimensional parameter analog to Taylor's, but dependent on the blast intensity. As a practical consequence of this work, it was shown that the effects of gas compressibillity acted to further reduce the the transmitted impulse to structures.

During the 1970's a number of experiments were performed on clamped plates suspended using ballistic pendelums. The intention of these experiments was to determine the underlying physics, and validate recent models for determining the failure modes in plates given blast loading. Typically, this loading was performed using sheet explosives applied to the surface of the plates. The first of these experiments were performed at MIT, department of Naval architecture and Marine engineering, by Norman Jones e.t al [17]. The intention of this experiment was to investigate the effect of an uniform velocity field with analytical solutions for plastic behaviour in plates. It was found to be appropriate to only consider plate bending if the permanent deflection was less than half of the plate thickness.

Further experiments were done on clamped beams in aluminium T6061 by Menkes et.al [20] at the City College of New York. In this case the amount

of sheet explosvies was varied, and the transfered impulse was measured using a ballistic pendulum. Three distinct failure modes were observed for increasing impulse. Namely an intial mode consisting of severe inelastic deformation for low impulses, tensile tearing at beam supports for intermediate impulses, and finaly shear failure for high impules. The data from the experiments were correlated with a finite difference model, assuming Timoshenko beam theory. After studying this model it was determined that the onset of shear failure was primarily dependent on beam velocities rather than shear stress.

These same failure modes were later confirmed for thin square plates by G.N Nurick et.al [24] of The University of Cape town in South Africa. The details of this experiment is given in section 3.6.

M.S Chafi et.al [10] did validation studies considering the response on round steel plates exposed to blast loading from TNT. Explosives and air continuum were modeled in LS-DYNA using the multi material ALE framework, with the equation of state determining the blast pressures from the explosion. The multi material air mesh was refined with the explosive charge, allowing for a good approximation of the initial detonation. The LS-DYNA displacement time histories were compared to experimental data with varying stand off distances of 0.065m and 0.1m, and varying TNT charge masses between 1.094kg and 0.468kg. The experimental data and the LS-DYNA model was found to be in good agreement over the whole range of stand off distances and explosive masses.

A similar study was performed by A.Bouamoul et.al [5]. The ALE multi material framework was used. In this article, experimental pressure data from sensors were used to validate the pressures obtained by the LS-DYNA simulation. A mesh convergence study was performed on the incident pressures, and it was found that the numerical results indicated significantly lower pressures than the results obtained from the sensors and ConWep data. The initial study was performed considering a spherical air mesh, so an attempt was done on a square mesh of roughly equal refinement. The obtained results were almost exactly the same, indicating that both meshes were equally sucsessful. Parametric studies were therefore performed on the bulk viscosity and the mesh contraction. This yielded only a slight improvement, so mass scaling of the charge was finally used to obtain agreement with experiments. Since the meshes considered were quite coarse, it is possible that better results would be obtained with increased mesh refinement.

Recent work at Livermore software coorporation [30] has resulted in a new approach, which combines the FSI capabilities of the ALE method with the speed of the ConWep blast function. The basic premises of this method is that only air adjacent to the structure is considered. The adjacent ALE elements are loaded using the blast function, and FSI is handeled by the ALE framework. This method was shown to be superior both in accuracy and computational time, as less elements need to be considered and less numerical attenuation occurs as the expansion wave travels through the mesh.

Lagrangian, uncoupled Eulerian-Lagrangian, and coupled Eulerian-Lagrangian simulations were done by Børvik et.al [7], to simulate blast loading on a 20ft container, corresponding to 4000 kg of TNT at a stand off distance of 120m. Their work was one of many steps in a project, where the major objective was to

develop a cost-effective and lightweight protection concept for a 20ft standard ISO container, to be used as shelter in international operations. The uncoupled Eulerian-Lagrangian simulation was divided into 3 steps. A 1D flow was considered to calibrate a model which gave the same pressure as ConWep when hitting the container. This model was implemented in a 3D model, to obtain the pressure history on each side of a rigid container. Finally the average pressure-time curves were applied to the flexible container. It was demonstrated, by using the uncoupled and coupled Eulerian-Lagrangian approaches, that the structural flexibility reduces the pressure loads, and thus the structural response. A pure Lagrangian simulation with pressure provided by ConWep based on corresponding finite rigid wall reflected pressures, will therefore lead to conservative design. More experimental data was needed to draw any clear conclusions.

Lars Olovsson et.al [28] conducted a study considering the air as perfectly elastic particles using the LS-DYNA Corpuscular air bag function. In this study a circular plate was exposed to a close stand off distance blast. The numerical results were compared to a ALE continuum model, and it was concluded that the Corpuscular method gave robust accurate results, low computational times, and a simple approach for the blast problem.

A constitutive model for interaction between sand particles was developed by Deshpande et.al [12]. The contact between sand particles may be treated as collisions analogous to molecules in a liquid or gas, or, as the packing density of the sand increases, semi-permanent contact. The goal of their work was to propose a model that covered both regimes. Their model was validated with experiments on steel plates exposed to blast loading done by Dharmasena et.al (2009).

Further work was conducted on the Corpuscular method, which resulted in the particle blast function in IMPETUS. Tore Borvik et.al [9] are currently working on an article which compares experimental data with results obtained by IMPETUS. The experiments were performed on square steel plates exposed to blast from 150g C4 at different stand off distances, and final deflections were measured. The IMPETUS code gave very accurate predictions in terms of final deflections, and good agreement with the ALE method in terms of plate impulse.

Chapter 3

Theory I - Explosion

Baker [1] defines explosion as a process by which a pressure wave of finite amplitude is generated in air by a rapid release of energy.

An explosion initiates a supersonically moving shock wave. The properties of air as a compressible gas together with the high velocity of explosive detonation, rises the disturbance at the shock front until it is nearly discontinuous. This is a nonlinear process which differs markedly from an acoustic wave [1]. The magnitude and distribution of the blast load on a structure is dependent on:

- Explosive properties - type and mass

- Casing effects - a free air blast gives a more important peak pressure than an air blast from a cased charge. On the other hand, cased charge leads to fragments.

- Distance between detonation and protective structure

- Interaction with ground plane or structure

For military explosives the velocity of the detonation/shock wave ranges from 6700 to 8840 m/s, the pressure ranges from 18620 to 38620 MPa, while the temperatures range from about 3800 to 5700 K [31].

3.1   Pressure generated by explosions

It is important to start of this section with stating the differene between the group velocity and particle velocity in terms of gas dynamics. One can illustrate this by considering a number of equal pendulums connected in series such that inclement angle is zero. If it is decided to drop one of the pendulums, one can observe that the propagation of the motion through the suspended balls is of much greater speed than the velocities of the end pendulums. By this fact the conclusion must be that the speed of the motion must be far larger than the speed of the induvidual pendulums.

This can be extended to gases by thinking of air as a dense net of particles. Energy is initially created by the explosion at the source of the blast. The energy will then set the nearest particles in motion such that particle collisions propagate in radial direction. The individual particles will collide and deflect resulting in a random pattern of moving particles with an average velocity away from the source. Thus we have two components of the motion one hydrostatic arising from random particle movements, and one dynamic component arising from the average velocity away from the blast source.

One differs between :

- Side-on pressure P_s (also called hydrostatic and incident pressure)

- Dynamic pressure

- Reflected pressure P_r

- Stagnation pressure

Side-on pressure is the pressure on a surface parallell to the radial direction of the shock wave within the region of overpressure [31].

In accordance with the bernoulli equation the particle velocity u and its density ρ leads to the **dynamic pressure** q. This pressure, equation 3.2, can be thought to be the increase in pressure one should expect, if a fluid in motion is brought to a standstill.

$$\rho \frac{u^2}{2} + \rho g z + P = C \tag{3.1}$$

$$q = \rho \frac{u^2}{2} \tag{3.2}$$

The reflected pressure occurs when a shock wave hits an object or a structure. If a finite surface is hit by a shock wave, the high reflected pressure seeks relief toward the lower pressure regions, the edges. The reflected pressure will decrease to the **stagnation pressure**, which is the sum of the side-on pressure and the dynamic pressure. On the other hand, the reflected pressure will last for the duration of the wave, if the wave strikes an infinite surface [31].

The easiest way to explain the pressure distrubution is to look at an **ideal shock wave**, figure 3.1. The shape of an ideal shock wave is only a function of the distance from the center of the source R, and time t. The explosion occurs in a still, homogeneous atmosphere, the source is spherically symmetric, and there are no groundeffects, free-air burst [1].

One can see from figure 3.1 the instantaneous rise from the atmospheric pressure P_0, to a peak side-on overpressure, $P_0 + P_s^+$. After the positive phase duration, t_0, one have a negative phase until the pressure goes back to the atmospheric. Smaller shocks can appear and effect the duration. The reflected pressure curve is simular, only with higher peaks.

The positive phase of the pressure can be approximated with the modified Friedlander equation 3.3, where b is a time constant of pressure wave form. The
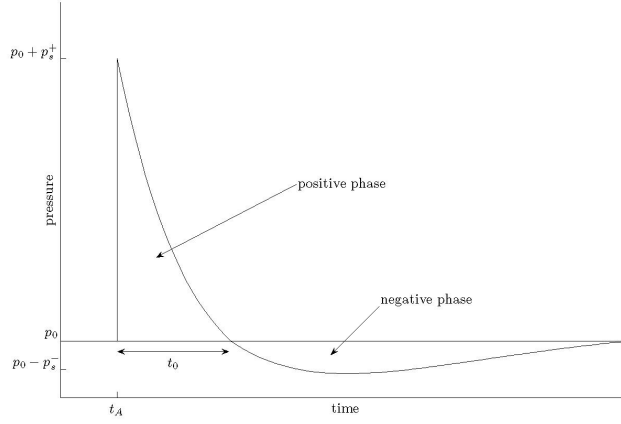
Figure 3.1: Ideal shock wave [29]

incident impulse is determined from equation 3.4. In most blast studies, the negative phase of the blast wave is ignored, hence only the equations for the positive phase are included [1] [31].

$$P_s(t) = P_0 + P_s^+(1 - \frac{t}{t_0})e^{\frac{-bt}{t_0}} \qquad (3.3)$$

$$i_s = \int_{t_A}^{t_A+t_0} P_s(t)dt \qquad (3.4)$$

One can find an expression for the reflected pressure, equation 3.5, by using the Rankine-Hugoniot equations. This gives a maximum value equal to $8P_s$. For an acoustic wave the reflected pressure is two times the side-on overpressure. γ is the ratio between heat capacities at constant pressure and volume, normally equal to 1.4 for air. Ideal gas is assumed, in other words it is only reliable for weak shock waves. It has been shown that the reflected pressure can reach as much as $20P_s$. For design purposes the parameters from reflected pressure may be taken, but the duration of the wave should correspond to the duration of the free-air pressure [2] [31].

$$P_r = 2P_s + \frac{(\gamma + 1)P_s^2}{(\gamma - 1)P_s + 2P_0\gamma} \qquad (3.5)$$

$$i_r = \int_{t_A}^{t_A+t_0} P_r(t)dt \qquad (3.6)$$

The reflected pressure depends on the angle of incidence α, shown in figure 3.2. The peak reflected pressure can be calculated by multiplying the pressure coefficient C_r by the peak side-on/incident pressure P_{so}.
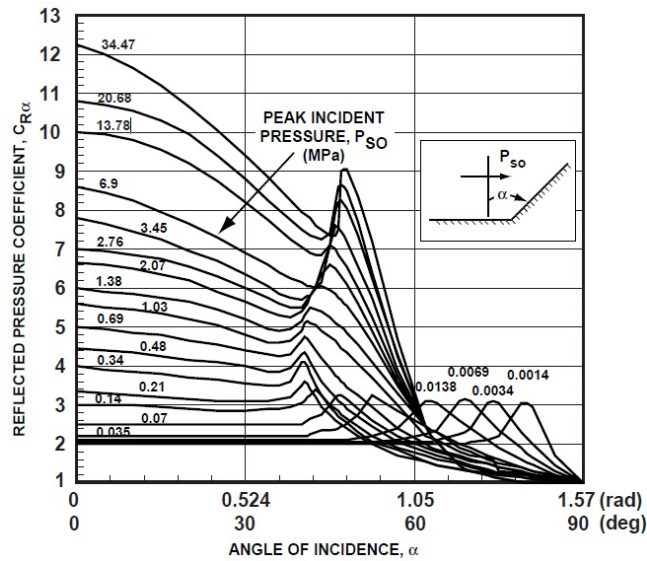
Figure 3.2: Peak reflected pressure as a function of angle of incidence [31]

3.2   Ground effects

In real life the shock wave is affected by weather conditions, atmosperic pressure and ground effects. An explosion which occurs on a perfectly smooth, rigid plane will reflect all energy at the ground plane, and effectively double the energy driving the expansion wave. In reality, the explosion dissipates some energy in ground cratering and in ground shock. A good "rule of thumb" is to multiply the effective source energy by a factor of 1.8 if signigicant cratering occurs [2]. This is valid for surface-bursts, explosion on the ground. The reflection also depends on the hight from the ground, see from figure 3.3. An explosion near the ground, where the shock wave interacts with the ground surface prior to arrival at the point of interest, is called a near-surface burst. The reflected shock wave interacts with the incident shock wave, and merge into a singular pulse called the Mach stem. For design purposes, the shock wave can be considered as plane over the full height of the front. The pressure-time variation stays the same, but the magnitude of the pressure is larger [31].
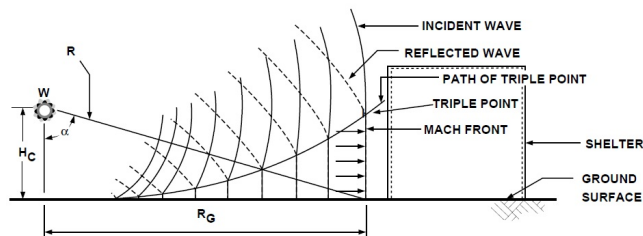
Figure 3.3: Groundeffects [31]

3.3   Cube-root scaling and scaled distance

Testing of structures exposed to blast loading, especially full scale testing, is not trivial. It is more convenient to do a small scale test, or even better, use already existing data. By using Hopkinson cube-root scaling, equation 3.7, one can attain the characteristic properties of the airblast wave from experimental data included in TM-855-1. Parameters such as overpressure, dynamic pressure, incident and reflected pressure, arrival time and particle velocity may be found for an explosion with charge weight W and stand off distance R [31].

An example is shown in figure 3.4. One searches the charge weight W for stand off distance R=1.5 m, giving the same peak reflected overpressure as when using W2=0.15 g and R2=0.15 m. Cube-root scaling gives W=150 g.

$$\frac{R}{R_2} = \left(\frac{W}{W_2} \right)^{\frac{1}{3}} \tag{3.7}$$
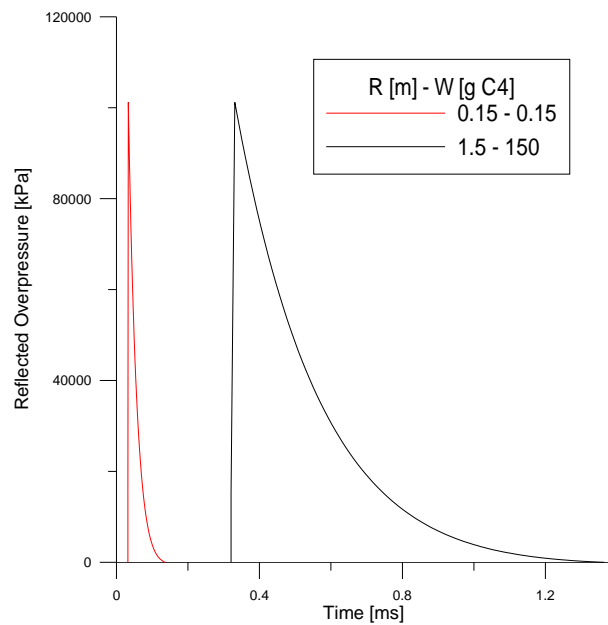
Figure 3.4: Cube-root scaling in practice
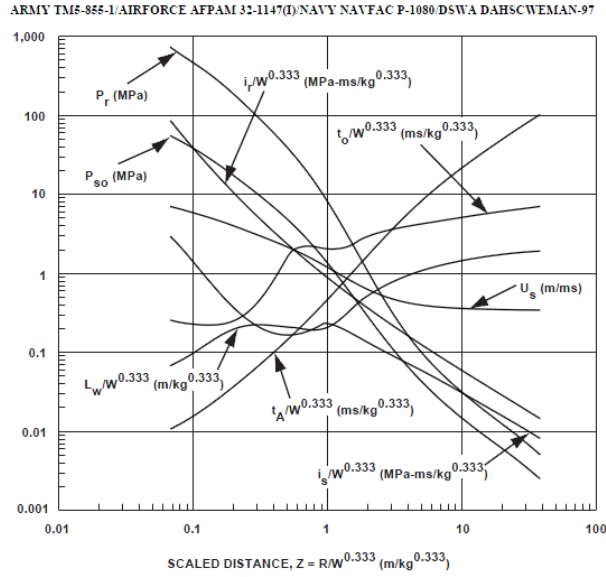
Figure 3.5: Blast characteristics as a function of scaled distance for TNT [31]

By calculating the scaled distance Z, equation 3.8, one can easily find a large amount of data associated with the blast wave, using plots based on empirical data.

$$Z = \frac{R}{W^{\frac{1}{3}}} \tag{3.8}$$

3.4   ConWep

ConWep is a well known "tool" in structural analysis when looking at blast loading. To avoid computational cost and complexity by doing CFD-analysis, one can simplify by using ConWep. ConWep is based on the empirical blast loading functions by Kingery and Bulmash. It is implemented in LS-DYNA as *LOADBLAST. The implementation is based on a report by Randers-Pehrson and Bannister [14]. The blast load equation is:

$$P(\tau) = P_r cos^2\theta + P_s(1 + cos^2\theta - 2cos\theta) \tag{3.9}$$

θ is the angle of incidence. The blast function can be used for free air burst of a spherical charge, and surface-burst of a hemisperical charge. To calculate the pressure, one define in the equivalent TNT mass, type of blast, charge location, and surface identification for which pressure is applied. There are some disadvantages though; during simulation, the pressure vector always stays normal to the surface of the shell, independent of the structural deformation. This is in conflict with the flow of the blast wave, and may cause inaccuracies if the deformation becomes large [23] [7].

3.5   Equation of state (EOS)

An equation of state is a thermodynamic equation describing the state of gases under a given set of physical conditions. It is a constitutive equation which provides a mathematical relationship between two or more state functions associated with the matter, such as its temperature, pressure, volume, or internal energy. Equations of state are useful in describing the properties of fluids etc. One of the simplest equations of state is the ideal gas law, which is accurate for gases at low pressures and moderate temperatures. When doing ALE analysis ,chapter 8, equations of state for the explosive and the air will be given.

The Jones-Wilkins-Lee JWL equation of state is an empirical mathematical expression used to describe the pressure-volume relationship associated with chemical products. It is used to calculate the state of the gas as it expands from a certain high-pressure, high-density condition, to some terminal state at normal pressure and gas density. The pressure is represented as a function of volume V and energy E, equation 3.10 [35].

$$P = A\left(1 - \frac{\omega}{R_1 V}\right)e^{-R_1 V} + B\left(1 - \frac{\omega}{R_2 V}\right)e^{-R_2 V} + \frac{\omega E}{V} \qquad (3.10)$$

The C4 values and definitions for equation 3.10 are given in table 3.1.

A	Pressure coefficient	597.4 GPa
B	Pressure coefficient	13.9 GPa
R_1	Principal eigenvalue	4.5
R_2	Secondary eigenvalue	1.5
ω	Fraction of the Tait equation, adiabatic exponent	0.32
E_0	Initial internal energy	8.7 GJ/m^3

Table 3.1: Input C4 to JWL equation of state

The air can be treated as a perfect gas, described by a linear polynomial equation of state, with pressure depending on density ρ and internal energi (E). γ is 1.4 and the initial internal energy E_0 is equal to 253.3 kPa, which gives an initial pressure equal to 1 atmosphere [14].

$$P = (\gamma - 1)\left(\frac{\rho}{\rho_0}E\right) \qquad (3.11)$$

3.6   Failure modes in plates

Experimental results obtained by G.N. Nurick et.al [24] illustrated that there
are basically 3 modes of failure for a clamped quadratic plate subjected to blast
loading, see figure 3.6.
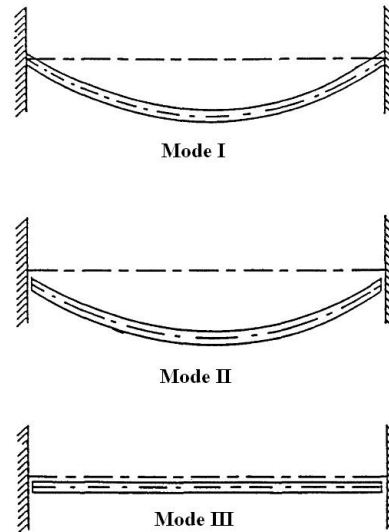
Figure 3.6: Failure modes [24]

- **Mode I failure:** Large ductile deformation with midpoint deflection in-
  creasing as a function of impulse. There may also be some shear deforma-
  tion with this mode. The failure mode is associated with lower impulses
  than the other modes.

- **Mode II failure:** A combination of ductile failure and partial to full
  tensile tearing at the supports. The support tearing is caused by initial
  shear deformation propagating further as tensile tearing. Mode II should
  be further subdivided into.

- Mode II*: Tensile tearing over parts of the support. Can be seen as an
  intermideate between mode I and II.

- Mode IIa: Full tensile tearing over entire support area and increasing mid-
  point deflection with increasing impulse.

- Mode IIb: Full tensile tearing over supports and decreasing midpoint de-
  flection as a funcion of impulse. The tensile tearing can usually be ob-
  served starting over the support midspan and then propagating towards
  the specimen corners.

- **Mode III failure:** Shear failure at supports. High levels of impulse will
  cause the supports to fail in shear before tensile tearing occurs. Deforma-
  tion will thus be localised with little energy dissipation. In terms of design
  this is clearly not a desireable outcome for our structure

3.7 Structures hit by fragments

Much of the theory behind this section is taken from Børvik [6], and Desphande et.al [12]. Earlier the blast wave, and its effects on structures have been discussed. An explosion often generates fragments, which together with the blast wave, damage the structure. The fragments may be pieces separated from its body beacause of failure, loose objects or sand generated by a mine. In other words, the size of the fragment may vary a lot, as well as the structures response. Inertia effects, stress wave propagation, and non quasi-static (transient) material behaviour are important elements in impact dynamics.

3.7.1 Projectiles and penetration

Depending on size, form, speed, mass etc, fragments may be assumed to act like projectiles leading to non-perforating and perforating deformation modes. Sand will be discussed later on.

According to Børvik [6], penetration is defined as the entry of a projectile into any region of a target. Backman and Goldsmith (1978) suggested the following penetration ways:

- **Perforation:** The projectile passes through the target with a final residual velocity, greater initial than dissipated energy

- **Embedment:** The projectile is stopped during contact with the target

- **Ricochet:** The projectile is deflected from the target without being stopped

Speed, mass, size, shape and hardness of the projectile are some om the parameters which decide the penetration way and the structur's response.

3.7.2 Response of structure

Estimating the structural response after an impact, and transforme projectile kinetic energy into work, is a highly complex process. Børvik devides the main mechanisms into:

- Elastic vibrations in target and projectile. These may transfer energy to the supports and initiate plastic deformations throughout the structure.

- Local plastic deformation of the sturcture, causing different types of failure.

- Global plastic deformation of the sturcture, with considerable membrane and bending strains.

- Projectile deformation or fracture.

- Friction at the interfaces between the projectile and target.

Military projectiles, velocity regime 500-1300 m/s, will typically lead to very little global deformation. Plastic work will occur both in the projectile and the

target area close to the penetration. Lower velocity, higher mass, and softer material lead to greater global deformations.

The ballistic limit velocity is an important parameter when designing a protective structure, and is given by the average of two projectile velocities; the highest velocity giving partial penetration, and the lowest velocity giving complete perforation. It has been shown that a projectile having a velocity just below the minimum perforation limit gives a maximum target deformation. Thus, both local and global deformation have to be considered when designing a protective structure exposed to fragments [6].

3.7.3   Sand

Explosions in sand, e.g. landmine-blast, will give different types of loading and stuctural response, depending on the water content in the soil and the depth of the sand. Dry sand fully disperses, while water saturated sand makes clumps and gives higher loading on the target. An explosion deep underground may generate no air shock, due to the energy absorbtion done by the soil. For design purposes the shock wave is often neglected.

Deshpande divides the detonation of an explosive burried in sand into three phases:

- **Phase 1:** Detonation of the explosive and the following soil interaction

- **Phase 2:** Expansion of the gaseous detonation products

- **Phase 3:** Development of soil ejecta

When the shock wave reaches the soil/air interface, phase 1 and 2, it is reflected and only a small part is transmitted into air. This means that the primary loading to the stucture is sand. The sand is ejected at high speed, generally in the upward direction, and forms an inverted cone. Figure 3.7 shows the traces of the ejecta in miliseconds, after an explosion of a 100 gram C4 mine buried 8 cm under dry sand [12].
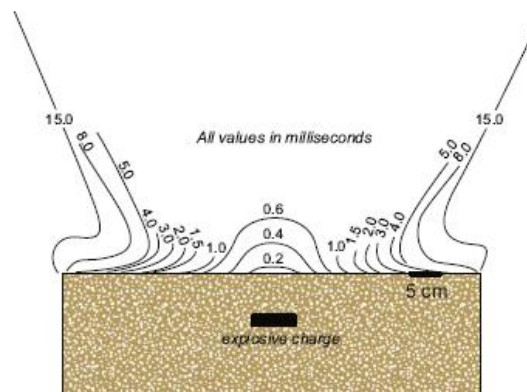
Figure 3.7: Explosion in sand [12]

Chapter 4

Theory II - Numerical methods

This chapter concerns the theory behind the numerical methods used in this paper. First there will be a descripton on numerical time integration and the attributes of explicite and implicite methods. Then there will be a summary of the three different finite element formulations, namely the Eulerian, Lagrangian and Arbitrary Lagrangian Eulerian (ALE) formulations. Special emphasis will be given to the ALE methods, where the mathematical construct and properties of the method will be discussed. Finally there will be a description of the basis of the Corpuscular method.

4.1   Explicit method

LS-DYNA is mainly using explicit time integration to solve nonlinear dynamic problems, e.g. explosions/blast loading. This section is based on the course notes from Non Linear Finite Element analysis TKT4197 [19] and LS-DYNA Theory Manual [13].

When using an explicit method, equation and equilibrium solving using iterative methods is not necessary. This means that each time increment is computationally inexpensive and iterative convergence is not an issue. The method is conditionally stable, and requires very small time steps. If the critical time step Δt_{cr}, equation 4.7, is exceeded, the numerical process become unstable. Beacause of the small time increments required, the explicit method is ideal for high-speed dynamic simulations. When dealing with problems involving discontinuous nonlinearities such as contact-, buckling-, and failure problems, the explicit method is preferable.

Equation of Motion of a MDOF System

$$[M]\left\{\ddot{D}(t)\right\} + [C]\left\{\dot{D}(t)\right\} + \left\{R^{int}(t)\right\} = \left\{R^{ext}(t)\right\} \qquad (4.1)$$

M: Mass matrix
D: Damping matrix
R^{int}: Internal force vector, K*D for linear elastic material
R^{ext}: External force vector, Pressure

The Central Difference Explicit Method

LS-DYNA uses the explicit central difference scheme to integrate the equations of motion. For the central difference method to be explicit, lumped mass must be employed. This eliminates solution of equations and increases the critical time increment.

$$\ddot{D}^n = M^{-1} \left(R_{ext}^n - C\dot{D}^n - R_{int}^n \right) \tag{4.2}$$

$$\dot{D}^{n+1/2} = \dot{D}^{n-1/2} + \ddot{D}^n \Delta t^n \tag{4.3}$$

$$D^{n+1} = D^n + \dot{D}^{n+1/2} \Delta t^{n+1/2} \tag{4.4}$$

$$\Delta t^{n+1/2} = \frac{1}{2} \left(\Delta t^n + \Delta t^{n+1} \right) \tag{4.5}$$

The geometry is updated by adding the displacement increments to the initial geometry.

The critical time increment for the central difference method is determined from the highest natural frequency ω_{max} and the damping ratio ζ.

$$\Delta t_{cr} \leq \frac{2}{\omega_{max}} \left(\sqrt{1 - \zeta^2} - \zeta \right) \tag{4.6}$$

For an undamped system, the critical time increment becomes:

$$\Delta t_{cr} \leq \frac{2}{\omega_{max}} = \frac{L}{c_d} \tag{4.7}$$

L is the element length, c_d is the speed of sound in the material. The critical time increment must be small enough that the information does not propagate more than one element length during a single time step.

Why not implicit method?

The implicit method is ideal for problems where either the response period of interest is long, or the nonlinearities are smooth. When using an implicit method, equation solving and equilibrium solving is necessary for each time increment. For each increment convergence must be obtained, which means that each increment is computationally expensive. On the other hand, the method is unconditionally stable. This means that the time increment size is not limited, and fewer increments are required fo complete a simulation. However one needs

to be assured that the timestep is significantly less than the the period of contact for contact-impact problems. There are also problems with the fact that newton solvers used in implicit methods are unable to resolve the discontinious shock waves which occur at high impact velocities.

4.2 Langrangian, Eulerian and ALE formulations

Most of this theory is related to chapters 4 and 7 in Nonlinear Finite Elments for Continua and Structures [3].

There are basically three numerical approaches for solving partial differential equations in terms of finite elements. Namely the Lagrangian, Eulerian and Arbitrary Lagrangian Eulerian (ALE) formulations. The difference between these formulations stems from how the mesh conforms to material motion. The subsequent sections will explain the differnce between these strategies and how they are adopted in the finite element program LS-DYNA.

4.2.1 Governing equations

The initial start point for the theory part, is to consider what solution variables need to be solved for. Typically, any dynamic finite element code needs to consider 3 physical laws. These laws are given in terms of spatial coordinates and are thus initally considered eulerian.

- Conservation of mass, equation 4.8
- Conservation of linear and angular momenta, equation 4.9 and 4.10
- Conservation of Energy, equation 4.11

$$\dot{\rho} + \rho v_{j,j} = 0 \tag{4.8}$$

$$\sigma_{ji,j} + \rho b_i = \rho \dot{v}_i \tag{4.9}$$

$$\sigma_{ij} = \sigma_{ji} \tag{4.10}$$

$$\rho E_{,t} = (\sigma_{ij} v_i)_{,j} + b_j v_j + (k_{ij}\theta_{,j})_{,i} + \rho s \tag{4.11}$$

E is defined in equation 4.12, where $V^2 = v_i v_i$.

$$E = W^{int} + \frac{V^2}{2} \tag{4.12}$$

The variables σ_{ij}, b, k_{ij}, θ, and s, are the stress tensor, body force, thermal conductivity tensor, temperature and specific source term respectivly.

4.2.2　Lagrangian Formulation

In the a Lagrangian mesh the nodes move with the deformation of the material. Consequently, the quadrature points are also locked within the material, making storage of variables very convenient for history dependent materials. The treatment of boundary condtions is also very straight forward as they are always incident with the material domain. In addition, the stiffness and mass matrices determined by the lagrangian formulation are always symetric by the law of conservation of angular momentum, which can easily be utilized to reduce computational time. However, in systems with large element deformation, the Jacobian determinant of the deformation gradient tensor, equation 4.14, may attain negative values, resulting in negative mass and energy densities. It is also the issue of the stable timestep decreasing as a function of the smallest dimension of the deformed element.

Since there is no convection of any properties in the Lagrangian formulation, the conservation of mass is given by stating that the mass of the elements are equal for subsequent timesteps. This implises that the density can be easily solved for, equation 4.13.

$$\rho(\mathbf{X}, t)J(\mathbf{X}, t) = \rho_0(\mathbf{X}) \tag{4.13}$$

$$J(\mathbf{X}, t) = Det(\mathbf{F}) \tag{4.14}$$

$$F = \begin{vmatrix} \frac{\partial x_1}{\partial X_1} & \frac{\partial x_1}{\partial X_2} \\ \frac{\partial x_2}{\partial X_1} & \frac{\partial x_2}{\partial X_2} \end{vmatrix} \tag{4.15}$$

Which also simplifies the conservation of momentum and energy equations to

$$\frac{\partial \sigma_{ij}}{\partial X_j} + pb_i = p\dot{v}_i \tag{4.16}$$

$$\rho\dot{E}^{int} = D_{ij}\sigma_{ij} - \frac{\partial k_{ij}\theta_j}{X_i} \tag{4.17}$$

When compared to the Eulerian and ALE formulation, the algebra needed to solve a Lagrangian system is far less complex, as the constitutive equations are solved using material points.

4.2.3　Eulerian Formulation

The Eulerian finite element formulation assumes that the mesh is incident with spatial reference points that do not change as the material deforms. The material properties are thus updated by using a combination of convection and source terms within the elements. It is no issue with decreasing stable timestep or negative mass, as elements do not deform. However there are errors assosciated

with the difference algorithms used for solving the convective terms that lead to smearing of discontuities and attenuation, which effectively separates variables traveling at different frequencies. The fact that the nodes are also fixed while the material moves and deforms is problematic, as the solution variables need to be mapped into the material domain to get history variables locked to material points. Last but not least, moving boundaries also pose problems, as rigid Eulerian nodes can not conform to the moving bondaries. This makes the Eulerian formulation most appropriate in fluid mechanics where history variables usually are not needed for moving points.

The governing equations for the Eulerian formulation in terms of spatial points is equal to what is given in section 4.2.1. However, in solid mechanics one is usually interessted in obtaining derivatives locked to material points. The differential equation for a volume moving with the material flow becomes:

$$\frac{Df}{Dt} = f_{,[x]} + f_{,i}v_i \tag{4.18}$$

v_i is the material velocity. The governing differential equations from section 4.2.1 will then take the form:

$$\rho_{,t[x]} + p_{,i}v_i + pv_{i,i} = 0 \tag{4.19}$$

$$\rho[v_{i,t[\chi]} + v_{i,j}v_j] = \sigma_{ji,j} + pb_i \tag{4.20}$$

$$\rho(E_{,t[x]} + E_{,i}v_i) = (\sigma_{ij}v_i)_{,j} + b_jv_j + (k_{ij}\theta_{,j})_{,i} + ps \tag{4.21}$$

4.2.4   ALE coordinate system

The basic difference between Lagrangian, Eulerian and ALE element formulations, is how the mesh is constructed. In the Lagrangian formulation the mesh follows material points, while in the Eulerian formulation the mesh is locked to spatial reference points. The ALE formulation takes the best from both methods, as it relieves the distortion in Lagrangian elements, and handles the moving boundaries unlike Eulerian methods. The key part of this formulation is that the mesh is able to move independently of the material and spatial domains, and consequently a third domain, namely the mesh or computational domain, is introduced. One thus has 3 coordinate systems in the ALE formulation which need to be defined, in order to get the material time derivatives of the three physical laws, equation 4.8, 4.9, and 4.10.

- The spatial coordinate system cooresponding to the Eulerian formulation defined by the domain Ω with the variable $\mathbf{x}$

- The material coordinate system cooresponding to the Lagrangian formulation defined by the domain Ω_0 with the variable $\mathbf{X}$

- The mesh coordinate system corresponding to the ALE formulation defined by the domain $\widehat{\Omega}$ with the variable $\boldsymbol{\chi}$

One may start by defining the spatial coordinates as a function of the material coordinates

$$\mathbf{x} = \Phi(\mathbf{X}, t) \tag{4.22}$$

Then define the intial mesh coordinates to be incident with the initial spatial coordinates

$$\boldsymbol{\chi} = \Phi(\mathbf{X}, 0) \tag{4.23}$$

Further more, one must define the transformation between mesh coordinates and spatial coordinates

$$\mathbf{x} = \widehat{\boldsymbol{\Phi}}(\boldsymbol{\chi}, t) \tag{4.24}$$

Having established these relations, one may obtain the mesh coordinates by taking the inverse of equation 4.22 and combine it with 4.23

$$\boldsymbol{\chi} = \widehat{\Phi}^{-1}(\mathbf{x}, t) = \widehat{\Phi}^{-1}(\Phi(\mathbf{X}, t), t) = \Psi(\mathbf{X}, t) \tag{4.25}$$

As the analysis progresses, the mesh will displace from the its initial incidence with the material. It is therefore appropriate to define a mesh displacement and velocity which will be utilized for computing the transport term in the following sections.

$$\widehat{u}(\chi, t) = \mathbf{x} - \boldsymbol{\chi} = \widehat{\Phi}(\chi, t) - \boldsymbol{\chi} \tag{4.26}$$

$$\widehat{v}(\boldsymbol{\chi}, t) = \widehat{\Phi}_{,t[\boldsymbol{\chi}]} \tag{4.27}$$

The needed equations for describing the material and mesh motion in the spatial coordinate system is thus defined. Figure 4.1 serves as an illustration for the mapping relationships.
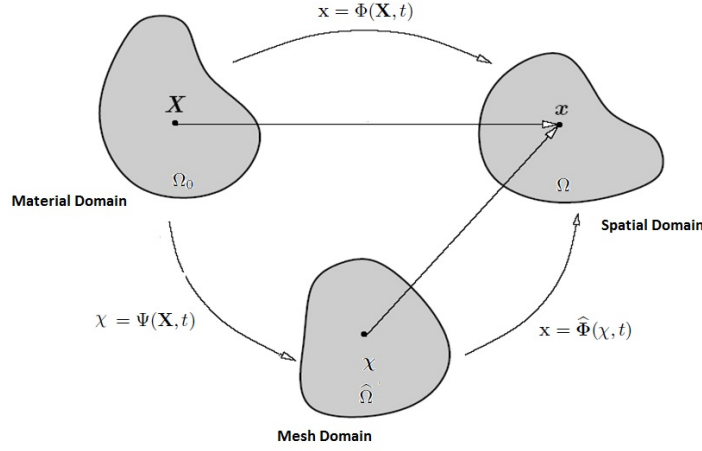
Figure 4.1: FEM domains

4.2.5   Advective velocity and material time derivatives

The next step is to express derivatives properly in the ALE formulation. If the coordinate system is shifted from the spatial domain $\mathbf{x}$ to the ALE coordinate system $\boldsymbol{\chi}$, one must recognize that the coordinate $\boldsymbol{\chi}$ is free to move in space and is therefore time dependent. Considering a function $f(\boldsymbol{x}, t)$, one must employ the chain rule to determine its proper derivative.

$$f(\mathbf{x}, t) = f(\widehat{\Phi}(\boldsymbol{\chi}, t), t) \tag{4.28}$$

$$\dot{f}(\boldsymbol{\chi}, t) = f_{,t[\chi]} + \frac{\partial f}{\partial \chi_i} \frac{\partial \chi_i}{\partial t} \tag{4.29}$$

To get the material velocity in terms of the ALE coordinate system, the inverse of equation 4.25 replaces $\mathbf{X}$.

$$v_j = \frac{\partial \Phi_j(\mathbf{X}, t)}{\partial t} = \frac{\partial \widehat{\Phi}(\boldsymbol{\chi}, t)}{\partial t} + \frac{\partial \widehat{\Phi}_j(\boldsymbol{\chi}, t)}{\partial \chi_i} \frac{\partial \Psi_i(\mathbf{X}, t)}{\partial t} \tag{4.30}$$

In order to find the velocity in which the mesh and material seperates, one subtracts equation 4.27 from 4.30.

$$a_i = v_i - \widehat{v}_i = \frac{\partial \widehat{\Phi}_i(\boldsymbol{\chi}, t)}{\partial \chi_j} \frac{\partial \Psi_j(\mathbf{X}, t)}{\partial t} \tag{4.31}$$

The derivatives in the mesh domain can alternatively be expressed with a spatial gradient.

$$\frac{\partial f}{\partial \chi_i} = \frac{\partial f}{\partial x_j} \frac{\partial x_j}{\partial \chi_i} \tag{4.32}$$

Substituting equation 4.32 into equation 4.30 gives

$$\frac{\partial f}{\partial t} = f_{,t[\chi]} + \frac{\partial f}{\partial x_j} \frac{\partial x_j}{\partial \chi_i} \frac{\partial \chi_i}{\partial t} \tag{4.33}$$

One recognizes that the product of the two last terms in equation 4.33 is equal to the advective velocity 4.31. The expression can then be written on its final form as:

$$\frac{\partial f}{\partial t} = f_{,t[\chi]} + \frac{\partial f}{\partial x_j} \frac{\partial \widehat{\Phi_j}(\boldsymbol{\chi}, t)}{\partial \chi_i} \frac{\partial \Psi_i(\mathbf{X}, t)}{\partial t} = f_{,[\chi]} + f_{,j} a_{,j} \tag{4.34}$$

4.2.6   Governing equations in ALE system

The material time derivatives are basically equal to the Eulerian time derivatives given in section 4.2.3. The only difference really being the substitution of the material velocity v_j with the convective velocoity a_j given in equation 4.31

$$\rho_{,t[\chi]} + \rho_{,j} c_j + \rho v_{j,j} = 0 \tag{4.35}$$

$$\rho[v_{i,t[\chi]} + c_j v_{i,j}] = \sigma_{ji,j} + \rho b_i \tag{4.36}$$

$$\rho(E_{,t[x]} + E_{,i} c_i) = (\sigma_{ij} v_i)_{,j} + b_j v_j + (k_{ij} \theta_{,j})_{,i} + \rho s \tag{4.37}$$

4.2.7   Implementation in LS-DYNA, Operator split

The implementation of the ALE formulation in LS-DYNA is based on succsessive steps of Lagrangian forumulation, followed by a remap step and advection steps [13].

In mathematical terms, this boils down to initially assuming that the mesh moves with the material. Considering the transport equation for one component of the Cauchy stress, equation 4.38,

$$\sigma_{,t[X]} = \sigma_{,t[\chi]} + a_i \sigma_{,i} = q \tag{4.38}$$

the advective term $a_i \sigma_{,i}$ falls away. The remaining equation becomes:
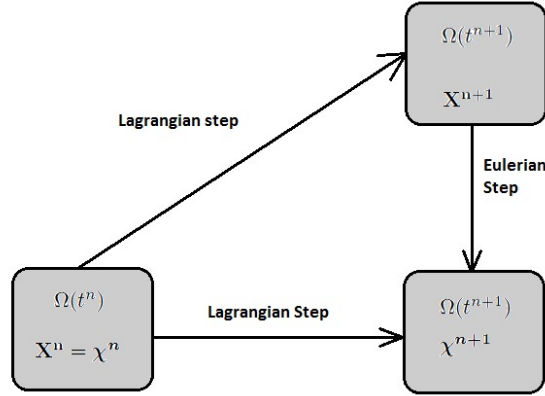
$$\sigma^n_{,t[X]} = q \tag{4.39}$$

Figure 4.2: Visual representation of subsequent Lagrangian and Eulerian steps

The derivative with respect to time is established, and it is possible to compute a trial solution for the Cauchy stress.

$$\sigma^{trial} = \sigma_n + \frac{\partial \sigma_n}{\partial t}_{[X]} \Delta t \tag{4.40}$$

After the Lagrangian step is completed one may choose to perform additional Lagrangian steps, or perform a remapping or smoothing to elminate mesh distortion. This remapping can be based on several different algorithms which will be mentioned in section 4.2.8.

After the new mesh is established, mass, stress, velocities and energies must be transported such that they correspond corectly to the new mesh. This is equivalent to the Eulerian step, equation 4.41, and is treated by advection. The advective speed a_i given in equation 4.31, is equal to the relative velocity between the mesh and material.

$$\sigma^{trial}_{,t[\chi]} + a_i \sigma_{,i} = 0 \quad q = 0 \tag{4.41}$$

Which is equvalient to the equation of advection, equation 4.42.

$$\frac{\partial \phi}{\partial x} = a(x) \frac{\partial \phi}{\partial t} \tag{4.42}$$

This implies that the stabillty of the advection step is related to the Courant Fredrichs Levy (CFL) criteria of computational fluid dynamics, equation 4.43.

$$C = \frac{c \Delta t}{\Delta x} = \frac{f}{V} \leq 1 \tag{4.43}$$

f is the transported volume of variable in question, and $V = \Delta x$ the volume of incident elements. The convective velocity c is the velocity difference between mesh and material, and is given by equation 4.31.

Having both convective velocity and the size of the adjacent elements, it is possible to compute the stable timestep based on the CFL condition. According to Olovsson [26], this criteria should restrict the flow of particles to be less than half incident element lenghts. This can be attained by selecting the timestep to be:

$$\Delta t_{cr} = min[\frac{\Delta x^e}{s}, \frac{\Delta x^e}{4c}] \tag{4.44}$$

s is the speed of sound in the material.

The motivation behind the operator split, is that it simplifies the the governing partial differential equation. The solution of the combination of the two partial differential equations 4.39 and 4.41, is not equal to the solution of equation 4.38, but it is simpler in terms of numerical stabillity, and far easier to implement correctly than a full solution of equation 4.38.

4.2.8   Solution schemes for the advection step

In the current LS-DYNA implementation, two different algorithms are implemented to solve the advection step, namely the first order accurate Donor Cell alogrithm and the second order Van Leer muscle scheme [36]. Both these methods are monotonic, which means that they do not create new maxima and minima in the solution variables.

$$max(\theta^{new}) \leq max(\phi^{old}) \tag{4.45}$$

$$min(\theta^{new}) \geq min(\phi^{old}) \tag{4.46}$$

They are also conservative which implies that:

$$\int_V \theta^{new} dV = \int_V \theta^{old} dV \tag{4.47}$$

Donor Cell alogrithm

The Donor Cell algorithm is an upwind method. This implies that it is only using data from upstream of the convective velocity [4]. The method of updating variables utilizes internal averaging. This means that the updated varibles are equal to the volume weighted average of their projection into the new mesh.
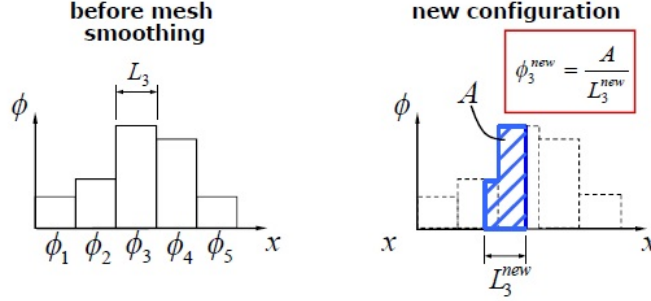
Figure 4.3: Remapping of soulution variables using Donor Cell scheme [26]

This can also be seen from how it is constructed mathematically, equation 4.48 and 4.49, as the flux f_j takes its information from location $j - 1/2$ if the convective velocity is positive, and $j + 1/2$ if it is negative [13].

$$\theta^{n+1}_{j+1/2} = \theta^n_{j+1/2} + \frac{\Delta t}{\Delta x}(f^\theta_j - f^\theta_{j+1}) \qquad (4.48)$$

$$f_j = \frac{c_j}{2}(\theta^n_{j-1/2} + \theta^n_{j+1/2}) + \frac{|c_j|}{2}(\theta^n_{j-1/2} - \theta^n_{j+1/2}) \qquad (4.49)$$

Van Leer scheme

Because of its first order accuracy, the Donor Cell alogrithm is highly dissipative. In order to reduce dissipation, Van Leer [36] introduced a second order accurate scheme. Like the Donor Cell algorithm this scheme is upstream, monotonic and conservative, but it replaces the piecewise constant nodal values over elements ϕ with a linear equation, figure 4.4. This equation is expanded around the element centroid to ensure conservation.
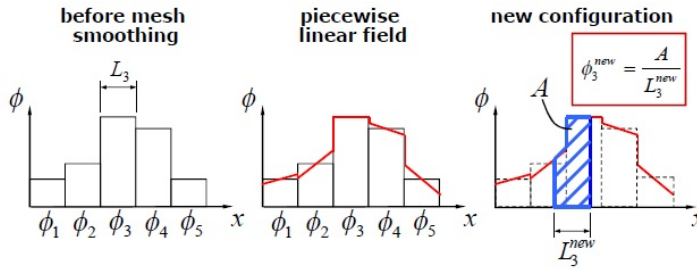

Figure 4.4: Remapping of solution variables using van leer scheme [26]

To ensure monoticity such that new minima and maxima are not created, the slope of the linear function is constructed such that the value of the element centroid and values of adjacent elements are not exeeded [13]. In matematical terms this is stated through the interpolation scheme as:

$$\phi_{j+1/2}^n(x) = S_{j+1/2}^n(x - x_{j+1/2}^n) + \phi_{0\,j+1/2}^n \tag{4.50}$$

$$S_{j+1/2}^n = \frac{1}{2}(sgn(s^L)) + sgn(s^R)) \times (min(s^L|, s_{j+1/2}^n|, s^R) \tag{4.51}$$

$$s^L = \frac{\phi_{0\,j+1/2}^n - \phi_{0\,j-1/2}^n}{\frac{1}{2}(x_{j+1/2} - x_j)} \tag{4.52}$$

$$s^R = \frac{\phi_{0\,j+3/2}^n - \phi_{0\,j+1/2}^n}{\frac{1}{2}(x_{j+1} - x_{j+1/2})} \tag{4.53}$$

$$s_{j+1/2}^n = \frac{\phi_{0\,j+3/2}^n - \phi_{0\,j+1/2}^n}{x_{j+3/2} - x_{j-1/2}} \tag{4.54}$$

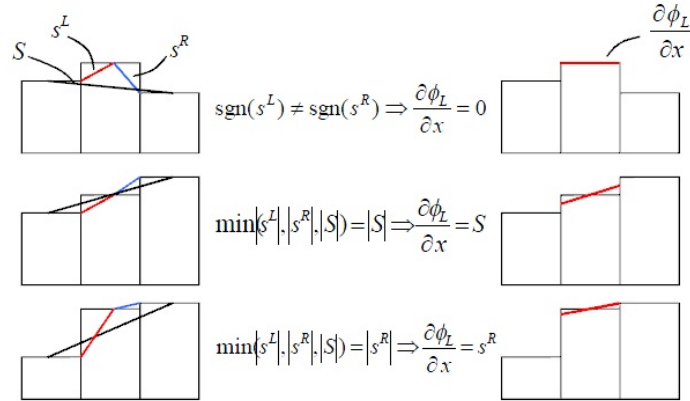Figure 4.5 shows how the slope is restricted for 3 different distributions of the parameter θ.

Figure 4.5: Slope selection based on ϕ distribution [26]

Half index shift

The Donor Cell and Van Leer scheme are effective algoritms for transportation of element centered variables, i.e stress, plastic strain, mass and energies. Velocity is however assosciated with element nodes. The half index shift moves the velocity half an index to the element centers. In 2D this implies that four nodal velocities must be transported to four different integration points, figure 4.6. They can then be transported using either Donor Cell or the Van Leer scheme. After the advection, they are moved back to the nodes in the updated mesh. Since the nodes have four different element incidents, four different velocites are obtained. They are consequently averaged to give the updated nodal velocity.
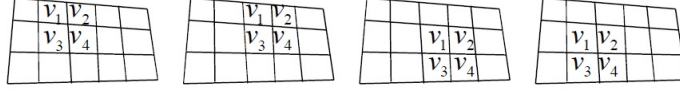
Figure 4.6: Transport of nodal centred values to integration points [26]

4.3 Artificial bulk viscosity

As mentioned in section 3.1, a discontinious shock front is created because the speed of sound increase with pressure. The unmodified finite element method capture discontinious solutions rather poorly, and have a tendency to create high frequency numerical oscillations within the shock front [4]. In modern finite element codes, this problem is addressed by introducing an artificial bulk viscosity term q to the momentum and energy equations [13].

$$q = C_0 \rho l^2 (\frac{ds}{dt})^2 - C_1 \rho l a (\frac{ds}{dt}) \quad if \quad \dot{\epsilon}_{kk} \leq 0 \tag{4.55}$$

$$q = 0 \quad if \quad \dot{\epsilon}_{kk} \geq 0 \tag{4.56}$$

C_0 and C_1 are dimensionless coefficients, typically selected as respectively 1.5 and 0.6. l is the lenght of the element, $\dot{\epsilon}_{kk}$ is the trace of the strain rate tensor, a is the speed of sound within the shock, and $\frac{ds}{dt}$ is the strain rate in the direction of acceleration.

After the visocosity is added, the shock front becomes continious with a thickness in the order of one element. The finite element codes thus become far more stable at the cost of smearing the shock. This may have the negative consequence of reducing the peak pressure during an airblast.

4.4 Contact formulations

Contact problems occur when two or more spatialy separated domains impact each other, or when two domains governed by different physical equations interact. In the case of fluid structure interaction (FSI), the contact alogrithm controls how the impulse is imparted on the structure, and how the flow is changed after FSI. Contact can generaly not be expressed through algebraic or differential equations, because it is impossible to anticipate the points on the two domains which will interact during an arbitrary motion [3]. This causes the inpenetrability condition to be stated in very general terms.

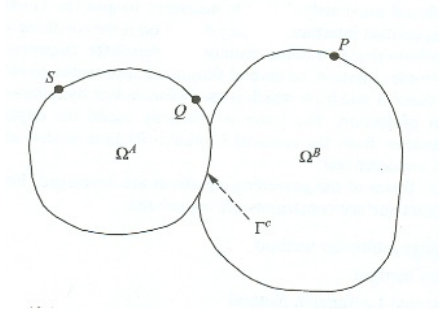$$\Gamma^c = \Gamma^a \cap \Gamma^b \qquad\qquad (4.57)$$

Figure 4.7: Contact of two initially seperated domains [3]

Any contact alogrithm must approximate the inpenetrability condition as best as possible, and it typically should be constructed to [32]:

- Address the finite deformation in 3 dimensional space.

- Automatically determine the contact associations between impacting elements.

- Enforce the interface boundary conditions, including friction between sliding boundaries.

In LS-DYNA there are currently implemented two different contact algorithms for the ALE formulation. Namely the Kinematic constraint method and the Penalty based method [13].

4.4.1   Kinematic constraint method

The Kinematic constraint method is subjected to impact and release condtions which determine the duration of the impact, and ensure conservation of momentum. It is basically constructed as a method of projection, where the equations that govern the movement of the slave domain is constrained to movement along a contact interface defined by the master domain. In order to ensure an efficient calculation, mass momentum and force are lumped on the master nodes. The velocity is consequently updated [3].

4.4.2   Penalty based method

The Penalty based method is constructed as a linear compression only spring, acting in between contacting interfaces. The method measures the degree of penetration of the slave mesh through a master surface, and applies a symmetric compressional force. In mathematical terms it is constructed rather simply as a heavyside step function. Its basic construction is on the form:

$$F_c = \alpha \int_{b_c} U(u_n - g)u_n db_c \tag{4.58}$$

u_n is a vector of displacement normal to the contact boundary b_c. g is the initial clearing between the impacting surfaces, and α is a suitable penalty number governing the strenght of the penalty force. The funcion $U(u_n - g)$ is defined as:

$$U(u_n - g) = 0 \quad for \quad (u_n - g) \leq 0 \tag{4.59}$$

$$U(u_n - g) = 1 \quad for \quad (u_n - g) \geq 0 \tag{4.60}$$

While the penalty method does not satisfy the contact boundary conditions as accurately as the Kinematic constraint method, it does have some sigificant advantages [32]:

- No new variables or extra degrees of freedom are needed to handle contact

- Permits symmetric treatment of the contact phase

- Very little numerical noise is created, thus severe hourglassing is not introduced in elements of low order with reduced integration

- Implemenation is straight forward

- Unlike in the Kinematic constraint method, arbitrary intersection of master-master and slave-slave surfaces are possible

The drawback of the method, is associated with how to determine the penalty number α. To enforce the boundary condition and ensure that no particles flow through the contact interface, it is necessary to select a high enough penalty number. However a high penalty number will ultimately decrease the stable timestep in explicit schemes. A good penalty alogrithm must therefore choose an appropriate value somewhere in between.

4.5   Corpuscular method

The theory in this section is taken from Olovsson et.al [25] [28] [9], and Desphande et.al [12].

A dicrete particle method, also known as the corpuscular method, has been developed by Olovsson et.al, and is implemented in IMPETUS Afea Solver. To begin with it was used for airbag simulations, but it is now also used to model close-range blast loading, and the interaction between high explosive detonation products, air, and sand. The corpuscular method has been found very robust, and less CPU-demanding than the Eulerian approaches. The pressure loading to a structure is described by momentum transfer from particles. The modelling of air and detonation products is based on kinematic molecular theory, originally derived by Maxwell (1860), while the modelling of sand is based on the Rheological model, proposed by Desphande et. al [12].

4.5.1   Kinematic molecular theory

In kinematic molecular theory one supposes that the molecules are rigid following Newton's laws, the collisions are perfectly elastic, the average distance between the molecules $\bar{L}$ is large compared to their size, and that the molecules are in random motion. In addition, ideal gas is assumed.

Olavsson [25] derives an expression for the pressure $\mathbf{P}$, equation 4.61, by looking at $\mathbf{N}$ molecules moving inside a box with volume $\mathbf{V}$, speed $v_i = [v_{x,i} v_{y,i} v_{z,i}]$ and mass m_i. Since the pressure is an expression of the translational kinetic energy only, a few large particles will give the same pressure as many small ones, as long as the total mass and the root mean square velocity v_{rms} are the same. In simulations, one particle represents typically $10^{15} - 10^{20}$ molecules.

$$P = P_x = P_y = P_z = \frac{1}{3V} \sum_{i=1}^{N} m_i \left| v_i \right|^2 = \frac{nMv_{rms}^2}{3V} = \frac{2W_k}{3V} = \frac{2}{3} w_k \qquad (4.61)$$

W_k is the total translational kinetic energy of all molecules, while w_k is per unit volume. $\mathbf{n}$ is the amount of mol, and $\mathbf{M}$ is the molar weight. The root mean square velocity is defined as the square root of the average velocity-squared of the molecules in a gas (Wikipedia). The ideal gas law, together with equation 4.61, gives an expression for v_{rms}, equation 4.62.

$$v_{rms} = \sqrt{\frac{3RT}{M}} \qquad (4.62)$$

w_k is a fraction $\xi(T)$ of the specific internal energy $\mathbf{e}$. $\xi(T)$ is a function of the heat capacities. Some energy is stored as spin and vibration. For a di-atomic gas at moderate temperature, 60 per cent is translational kinetic energy, while 40 per cent is spin. In a mono-atomic gas, no energy is stored as vibration or spin, $\xi = 1$. Assuming temperature independent heat capacities, $e = \rho C_v T$, one

ends up with equation 4.63. γ is the ratio between heat capacities at constant pressure and volume, and lays between 1 and 5/3.

$$\xi(T) = \frac{3\rho(C_p - C_v)T}{2e} \Rightarrow \frac{3}{2}(\gamma - 1) \tag{4.63}$$

$$p = \frac{2}{3}w_k = \frac{2}{3}\xi(T)e = (\gamma - 1)e \tag{4.64}$$

The particles will loose some energy while impacting the expanding box. Olavsson [25] derives an expression for the rate of dropping energy, equation 4.65. E is the total internal energy in the gas, and $\dot{V}$ is the volume increase rate. Assuming temperature independant heat capacities, the same energy drop as when working with the ideal gas law is predicted.

$$\dot{E} = -\frac{2\xi E}{3}\frac{\dot{V}}{V} \Rightarrow E_1 = E_0 \left(\frac{V_0}{V_1}\right)^{\gamma - 1} \tag{4.65}$$

In a box filled with gas, one will find molecules flowing around with a great variety of velocities. The **Maxwell-Boltzmann distribution** for speed, equation 4.66, gives the probability for a certain speed to occur. The velocity distribution is implemented in LS-DYNA and IMPETUS to translate macroscopic properties to particle data.

$$f(|v|) = 4\pi \left(\frac{M}{2\pi RT}\right)^{3/2} |v|^2 \, exp\left(\frac{-M\,|v|^2}{2RT}\right) \tag{4.66}$$

4.5.2 Rheological model

While the contact between air particles and detonation products can be modelled as purely elastic collisions, a penalty based contact is used for the sand. The Rheological model uses two linear springs to describe the interaction between two sand particles with mass m_p, one spring acting in the normal direction, the other one in the tangential direction, both having the stiffness $\mathbf{K}$. Parallell to the spring acting in the normal direction it is a linear dashpot with damping coefficient $\mathbf{C}$. The tangential spring force is limited by a Couloumb friction coefficient μ [9].
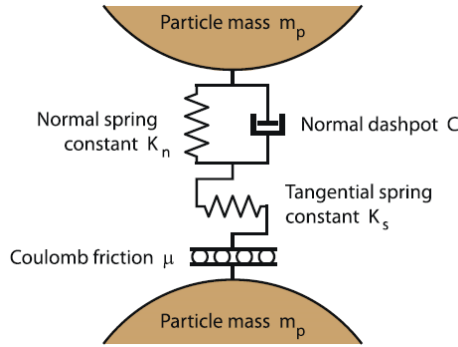

Figure 4.8: Rheological model, interaction between two sand particles [12]

The normal and tangential contact forces, F_n and F_s, are given by equation 4.67, 4.68, and 4.69. δ_n and δ_s are the relative normal and tangential displacements of the contacting particles [12].

$$F_n = K_n \delta_n + C \dot{\delta}_n \tag{4.67}$$

$$F_s = -K_s \delta_s \qquad if \qquad |F_s| \prec |\mu F_n| \tag{4.68}$$

$$F_s = -\mu |F_n| \, sign\left(\delta_s\right) \qquad otherwise \tag{4.69}$$

The damping coeffisient determines the loss of energy during collisions, and is directly related to the coefficient of restitution $\mathbf{e}$, equation 4.70. The collision time t_c is a function of mass, coefficient of restitution, and the damping coeffisient, equation 4.71. A plastic collision, $e = 0$, gives infinite collision time [12].

$$e = exp\left[-\frac{\pi C}{\sqrt{2m_p K_n - C^2}}\right] \tag{4.70}$$

$$t_c = -m_p \frac{ln\left(e\right)}{C} \tag{4.71}$$

Chapter 5

Experimental data and Material Modeling

The investigations in this paper were primarly performed on a square plate in Steel AL6XN. The original intention however, was to perform investigations on a honeycomb truss structure in AL6061-T6. Experimental data regarding honeycomb truss behavior under blast loading was not attained, so further investigations on the honeycomb truss was omitted. There were however experiments performed on specimens in AL6061-T6 to determine strain rate dependency and fracture strain. This might be useful for further work so it is included together with material data obtained from the litterature for AL6XN.

5.1 Johnson Cook model

This section will deal with the material behavior of our plate in terms constitutive laws and possibe failure modes. Emphasis will also be given on the implemenation of these models in finite element formulation and the pitfalls which consequently may arise.

In problems with large plastic strain velocities and coupled material-thermodynamic behavior, standard elastic plastic material models are not sufficient to capture the material behavior accurately. Usage of these models usually requires definition of kinematic and istropic hardening properties, which are very hard to identify correctly. Johnson and Cook indtroduced a model which expresses the flow stress as a function of plastic strain, strain rate and temperature, equation 5.1. These parameters are easy to determine, thus making model calibration a simpler task.

$$\sigma_{eg} = [A + B(\epsilon_e^{pl})^n][1 + C\ln(\frac{\dot{\epsilon}_e^{pl}}{\dot{\epsilon}_0})](1 - \theta^m) \qquad (5.1)$$

Where $\dot{\epsilon}_0$ is a reference strain rate, ϵ_e^{pl} is the equivalent plastic strain, $\dot{\epsilon}_e^{pl}$ is the plastic strain rate and θ is a normalised temprature which takes the form

$$\theta = \frac{T - T_r}{T_m - T_r} \tag{5.2}$$

Now there are at least two problems assosciated with the Johnson Cook model [15].

- **Unphysical strain rate:** The strain rate effect captured by the logarithmic term in the model is unphysical. It is evidence proving that an exponential function of the strain rate is more appropriate. Problems are also associated with small strain rates as the natural logarithm goes towards minus infinity.

- **No kinematic hardening:** The Johnson Cook model does not include any form of kinematic hardening, and thus the Bauschinger effect is not considered. This is ok for problems with no stress reversals, but for other loading situations errors will occure.

- **No damage coupling:** The Johnson Cook model does not account for cross sectional damage in the flow stress. However, models which account for damage are usually not employed because of complexity [8].

- **Assumes homogenity:** The Johnson Cook model assumes that the material is homogenous in all principal directions. Some fairly common steel and aluminium alloys do however not satisfy this, as extrusion and forming processes lead to different material characteristics along different planes in the material.

5.2   Material AL6XN

The steel AL6XN described by Nemat-Nasser [22] is a relatively new stainless steel which shows promising ductilty characteristics. Nemat-Nasser performed uniaxial compression tests over a range of temperatures (77K - 1000K) and varying strain rates ($0.001s^{-1}$ - $8000s^{-1}$). The properties of AL6XN were found to be as follows:

- Very good ductility. For high strain rates and low temperatures it was estimated to be over 40 %, and increasing with increasing temperature.

- The temperature was found to have a greater effect on the flow stress than the strain rate.

- At low temperatures and high strain rates, failure was assosciated with adiabatic shear bands, forming if the strain was in excess of 40 %.
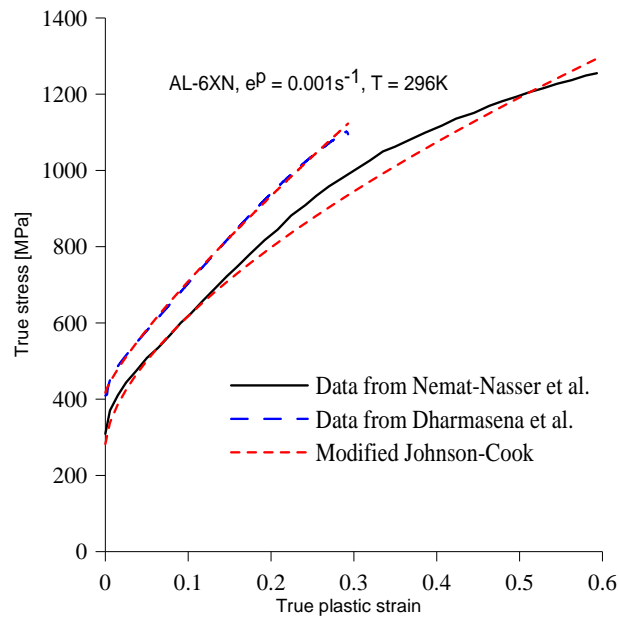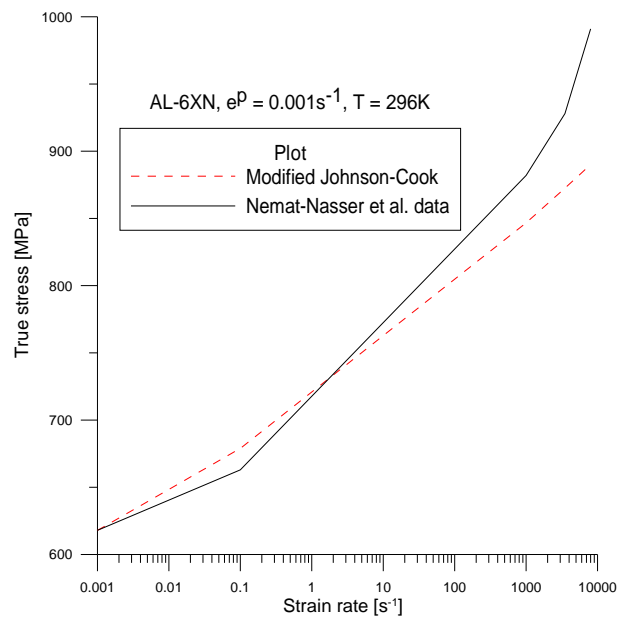
Figure 5.1: Strain hardening
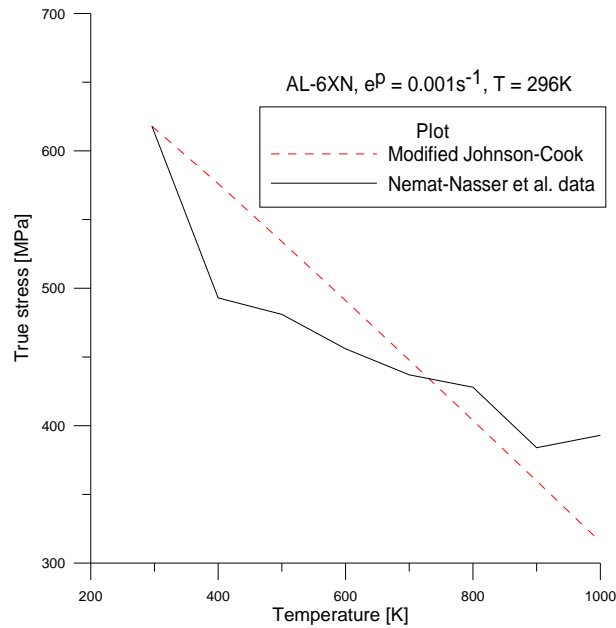

Figure 5.2: Strain-rate hardening

Figure 5.3: Temperature softening

In Nemat-Nassers article [22], a material model based on movement of dislocations were utilized. This model is rather complex and thus seldom used. A far simpler alternative is the previously mentioned Johnson Cook model. Using the least squares approach, Tore Børvik et.al [9] calibrated the JC parameters concerning temperature and strain rate to fit the data obtained from Nemat-Nassers article. The quasi static stress-strain part of the JC model was computed from experimental results by Despande et.al. This approach was chosen because the plate used in Børviks and Deshpande et.al experiment was coldformed. The specimens used by Nemat-Nasser were fabricated using electro-discharge machining to eliminate residual stresses. The assumptions for the calibration of the JC model was:

- Room temperature $T = 296K$ for the true-stress true-strain curve, and the strain rate dependent part.

- A neglible strain rate $\dot{\epsilon}^p = 0.001s^{-1}$ for the quasi static true-stress true-strain curve.

- A plastic strain $\epsilon^p = 0.1$ for the temperature and strain rate dependent parts.

5.2.1 Fracture criterion

Fracture in the modified Johson Cook model is modeled utilzing element erosion. This means that when the plastic work per unit of volume reaches the critical value W_c, the element is eroded from the mesh [14]. This parameter was determined by integrating the Dharmasena curve, figure 5.1, from zero to final quasi static fracture.

$$W_c = \int^{\epsilon_{cr}} \sigma d\epsilon = 235.7 E6 Pa \qquad (5.3)$$

5.2.2 Input material data for ALX6N Steel

The input data to the Johnson Cook model, table 5.1, and the physical data for AL6XN steel, table 5.2, is taken from Børvik et.al [9]. The critical energy parameter is also included in table 5.1.

A [MPa]	B [MPa]	n	C	$\dot{\epsilon}_0$	m	$W_c[Pa]$
410	1902	0.82	0.024	0.001	1.03	235.7E6

Table 5.1: Johnson Cook parameters AL6XN

E [GPa]	$\rho[\frac{kg}{m^3}]$	ν	$C_p[\frac{J}{kg*K}]$	$T_m[K]$	$T_r[K]$	$\alpha[\mathrm{K}^{-1}]$
195	8060	0.3	500	1700	296	1.5E-5

Table 5.2: Physical data AL6XN

5.3   Material AL6061-T6

5.3.1   Microstructure

Several samples of the profile have been investigated by Ketill Pedersen, SINTEF Materials and Chemistry. They show a huge variation in the microstructure. In some parts of the profile, the grains were found to be several millimetres ,see figure 5.4. Large pores were also observed in the material. Material testing on small specimen, D=3 mm, will obviously lead to great variation in fracture strain. A pore in the tensile specimen will reduce the fracture strain even more. Consequently, not only the orientation to the extrusion direction change the material behaviour, but also where in the material the specimen is taken from.
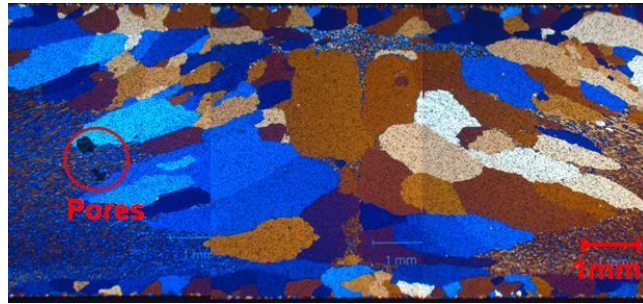

Figure 5.4: Grain structure

5.3.2   Quasi-Static tensile test

Quasi-static tests on AL6061-T6, have been done by SINTEF Materials and Chemistry . Nine tests with three different orientations to the extrusion direction, 0, 45 and 90 degrees. The geometry of the specimen is shown in figure 5.5.
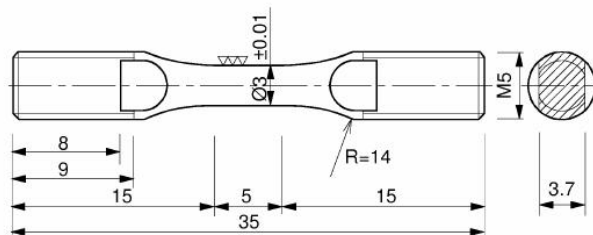

Figure 5.5: Geometri of specimen used in the quasi-static tests

A 20 kN DARTEC servohydraulic universal testing machine with displacement control was used. The velocity was 0.15 mm/min, giving a strain rate of $5 * 10^{-4}s^{-1}$. Force and minimum diameter, one in the thickness direction D_Z and one in the transverse direction $D_\perp$ of the specimen, were measured to fracture.

Crossection area A, true stress σ, and true strain ϵ could then be calculated by using equation 5.4, 5.5 and 5.6. Fracture strain ϵ_f was found by inserting the fracture cross section area A_f in to equation 5.6.

$$A = \frac{\pi}{4} D_Z D_\perp \tag{5.4}$$

$$\sigma = \frac{F}{A} \tag{5.5}$$
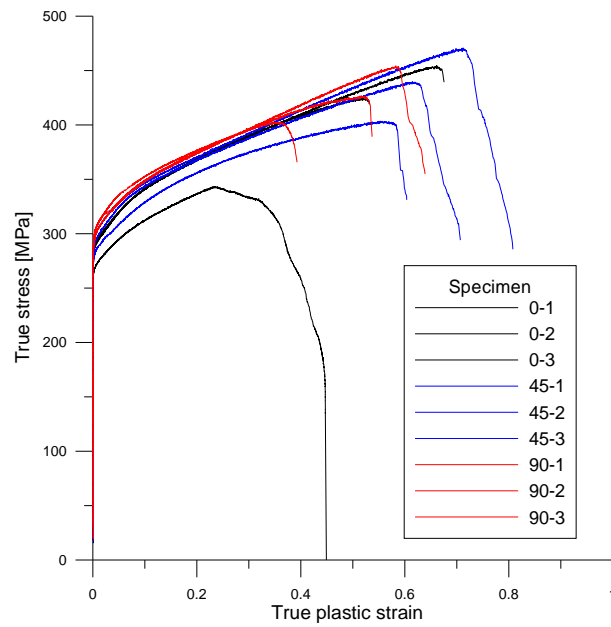
$$\epsilon = ln\frac{A_0}{A} \tag{5.6}$$

Figure 5.6: Quasi-Static tensile test, three orientations to the extrusion direction

Figure 5.6 shows that the stress level was about the same for all the tests. Fracture occured randomly, which indicates anisotropic material. The highest and lowest fracture strain was found to be respectively 0.81, for 45 degrees, and 0.39, for 90 degrees.

5.3.3   Dynamic tensile test - Split Hopkinson

In order to calibrate the Johson Cook model correctly, material tests data must be aquired to account for material strain rate and temperature dependency. For this goal, a Split Hopkinson test was performed. The Split Hopkinson test rig used at the department of structural engineering and the theory needed to to determine material strain rate dependency is desribed by Clausen [11]. The rig can in rough terms be described by figure 5.7.
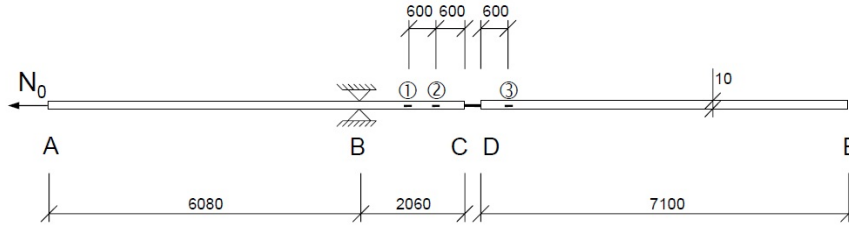

Figure 5.7: Split Hopkinson test rig

The test procedure starts by clamping point B, using a frictional clamp. This clamp is secured using a notched bolt which will eventually break given sufficient stress. The bolt is manufactured in low ductility SS2140 steel and given a notch to ensure triaxial stress state and brittle fracture. The importance of the brittleness is assosciated with the steepness of the shock front, as a more ductile bolt would ultimately give a larger failure time and a less cohesive front. A hydraulic jack is winded up such that a given stress is attained in rod A-B. At this point further level of clamping force is increased such that the bolt breaks. A tensile stress wave will then travel from point B towards C. The tensile stress wave will be recorded at strain gauges 1, 2 and 3. Consequently, parameters such as stress, strain and strain rate can be determined using stress propagation theory.

Wave propagation in the Split-hopkinson test rig

Even though the possion ratio cause contractions and expansions in metals, it is generally assumed that the effect on this can be negelected in stress wave theory. The standard hyperbolic wave equation then takes the form.

$$\frac{\partial^2 u}{\partial^2 t} = c^2 \frac{\partial^2 u}{\partial^2 x} \tag{5.7}$$

The general soltution can be determined to be the d'Alembert solution.

$$u(x,t) = f(x - ct) + g(x + ct) \tag{5.8}$$

f is the equation representing the propagating wave in the positive direction, and g is the equation representing propagation in the negative direction. c

represents the velocity of propagation. For an isotropic material it is equal to the speed of sound and can be determined as.

$$c = \sqrt{\frac{E}{p}} \tag{5.9}$$

Stress state and velocity can easily be found by differentiate equation 5.8.

$$\sigma(x,t) = E[f'(x - ct) + g'(x + ct)] \tag{5.10}$$

$$v(x,t) = \frac{\partial u}{\partial t} = c[-f'(x - ct) + g'(x + ct)] \tag{5.11}$$

Determination of stress, strain and strain rate

After the clamp is relased in point B, the stress wave is recorded at point 2, figure 5.7. It is then assumed that no dispersion occurs, such that the strain is equal at point C. As the wave is incident with point C, it is partly transmitted and reflected giving strain components in sensor 2 and 3.

$$\epsilon(x_c, t) = f'(x_c - c_0 t) + g'(x_c + c_0 t) = \epsilon_I + \epsilon_R \tag{5.12}$$

$$\epsilon(x_d, t) = f'(x_d - c_0 t) + g'(x_d + c_0 t) = \epsilon_T \tag{5.13}$$

With equation 5.11 the current strain rate at C can also be found.

$$\dot{\epsilon}(x_c, t) = c(-f'(x_c - c_0 t) + g'(x_c + c_0 t)) = c(-\epsilon_I + \epsilon_R) \tag{5.14}$$

$$\dot{\epsilon}(x_d, t) = c(-f'(x_d - c_0 t) + g'(x_d + c_0 t)) = c(-\epsilon_T) \tag{5.15}$$

f and g can not be determined analytically. However the signals obtained from the strain gauges, ϵ_I, ϵ_R and ϵ_T can be integrated numerically. The stress, strain, and strain rate parameters needed to calibrate the Johnson Cook model can then be determined as, [11]:

$$\sigma_s = \frac{E_0 A}{A_s} \epsilon_t \tag{5.16}$$

$$\epsilon_s = -2 \frac{C_0}{L_s} \int_0^t \epsilon_r d\tau \tag{5.17}$$

$$\dot{\epsilon}_s = -2 \frac{C_0}{L_s} \epsilon_r \tag{5.18}$$

5.3.4   Dynamic tensile test - Fracture strain

The fracture strain obtained from the quasi static tests was found between 0.4 and 0.8, 5.3.2. One can however not expect this to be true during the high strain rates that occur under dynamic loading. Under these conditions, most metals have much lower ductility, and in order to predict failure accurately, one has to determine a dynamic fracture strain for the high strain rate regimes.

Seven tests with three different orientations to the extrusion direction, 0, 45 and 90 degrees, were done. To obtain the fracture strain from the dynamic tests, a microscope was utilized to determine the diameter before and after fracture.

Specimen	D_0 [mm]	$D_{f1}[mm]$	$D_{f2}[mm]$	$D_{favg}[mm]$	$\epsilon_f = \frac{D_0}{D_f}$
0-1	3.01	2.075	2.550	2.313	0.263
0-2	3.02	2.400	2.500	2.450	0.209
0-3	3.01	2.240	2.550	2.395	0.229
45-2	3.02	2.240	2.100	2.170	0.331
90-1	3.01	2.100	2.345	2.222	0.304
90-2	3.01	2.270	2.335	2.300	0.269
90-3	3.01	2.355	2.240	2.297	0.270

Table 5.3: Measured dynamic fracture strain for AL6061

D_0: Intial undeformed diameter
D_{f1}: First measure of fracture area diameter
D_{f2}: Second measure of fracture area diameter
D_{avg}: Average fracture diameter
ϵ_f: Final true fracture strain

The critical plastic work per unit of volume W_c was found by integrating the equivalent stress with respect to the plastic strain until fracture. Part 1 and 2 in equation 5.20 were neglected. ϵ_f was assumed to be 0.268, the average of the fracture strains, table 5.3.

$$W_c = \int_0^{\epsilon_f} (A + B\epsilon_q^n) = (279E6 + 220E6\epsilon_q^{0.57}) = 90E6Pa \qquad (5.19)$$

5.3.5   Calibration of the Johnson Cook model

Calibration of the Johnson Cook model starts by assuming that the parameters dependent on strain, strain rate and temperature are independent of each other. This is, strictly speaking, not quite true, but by using the typically occuring values for plastic strain, strain rate and temperature, one should be able to get good agreement with experimental results.

$$\sigma_{eg} = \underbrace{[A + B(\epsilon_e^{pl})^n]}_{Part1} \underbrace{[1 + \frac{\dot{\epsilon}_e^{pl}}{\dot{\epsilon}_0}]^C}_{Part2} \underbrace{[1 - \theta^m]}_{Part3} \qquad (5.20)$$
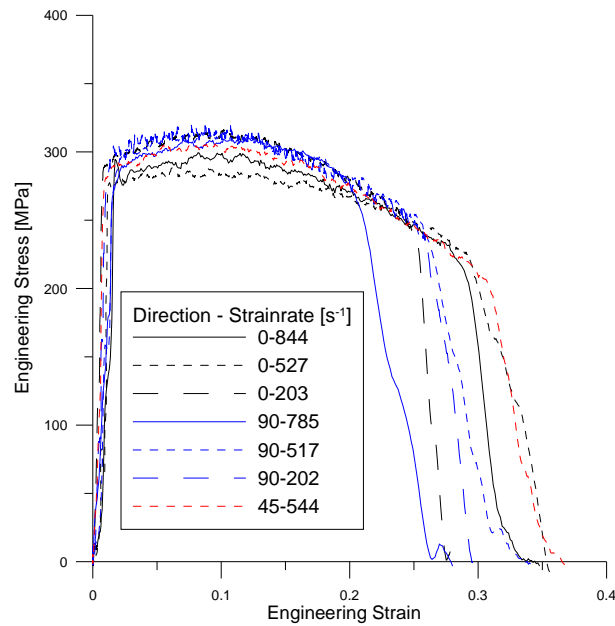
Figure 5.8: Split Hopkinson, engineering stress-strain, with respect to extrusion direction and strainrate

- **Parameters part 1:** The first parameters A, B and n are fitted using quasi static test results. As seen in figure 5.6, there were some differences in the initial flow stress between the different extrusion directions and even between samples in the same direction. The strain hardening however, seemed to be more or less equal for all samples and directions. Since the material coarseness causes this large spread of flow stress, there must be a certain amount of guesswork in determining the correct properties for the JC model. The curve 90-2 was therefore chosen for fitting using the least squares method, as it represented a typical trend. The strain rate was assumed quasi static $\dot{\epsilon}_e^{pl} = 0$ and the temperature was assumed to be $T = 296K$.

- **Parameters part 2:** The next parameters, $\dot{\epsilon}_0$ and C, represent the strain dependent part of the solution. Determination of this parameter is based on the Split Hopkinson test results. To determine the strain dependency, the assumption is that $\epsilon_{pl} = 0,04$. It was considered such as the strain rate was stable and without dynamic interference for all specimens at this particular strain. When applying this material model in a finite element calculation, it should be verified that the typically occuring plastic strain is close to the predicted $\epsilon_{pl} = 0,04$. Since the Split Hopkinson tests were performed at room temperatures, the temeperature must be assumed to be $T = 296K$. This might be problematic as the plastic deformations could raise temperatures to such a degree that one effectively calibrates the dynamic parameters for the wrong temperature. Preheating the specimens to agree with fracture temperature will resolve this, but is currently not an avaliable option at the NTNU Split Hopkinson rig.

- **Parameters part 3:** There is currently not any avaliable equipment to determine the temperature dependent part of the JC model. If it was to be accesible, the assumptions would be $\dot{\epsilon}_e^{pl} = 0$ and plastic strain $\epsilon_{pl} = 0,04$. A uniaxial tensile test should then be performed recording the true stress as a function of temperature. Using these data and the reference temperature, the parameter m could be determined using least squares fitting. There is probably published experimental data concerning temperature depedency for AL6061-T6 in the litterature, but since the material is not actually used in this paper it would be somewhat redundant to devote any more time to it.

The experimental data compared to the Johnson Cook model is given in figure 5.9 and 5.10. The material data is given as points and the Johnson Cook model is shown as trendlines.
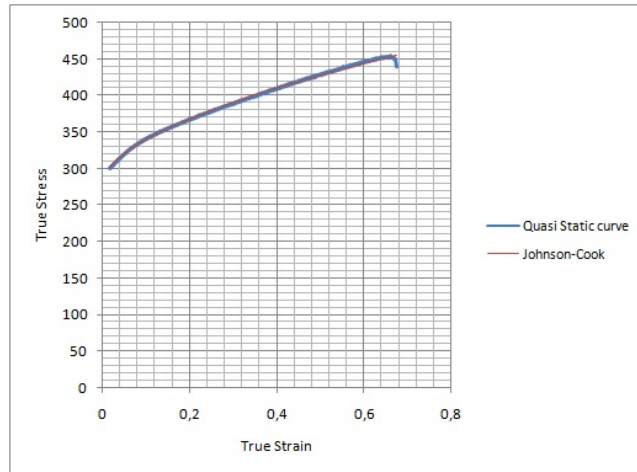
Figure 5.9: Parameters, Part 1, Experimental data vs. Johnson Cook model
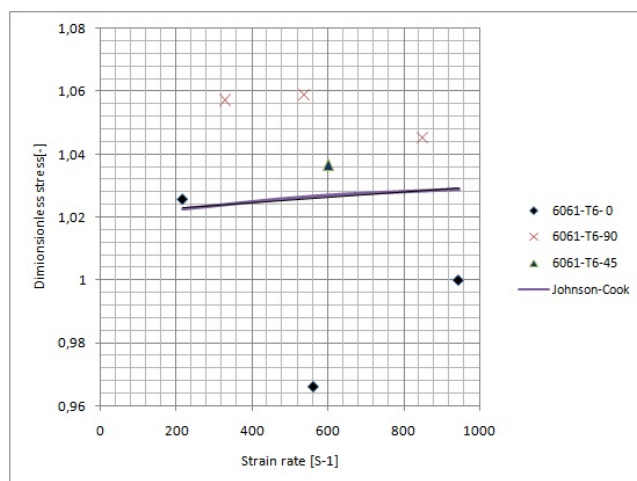
Figure 5.10: Parameters, Part 2, Experimental data vs. Johnson Cook model

From figure 5.8 it is apparent that there are problems assosciated with the coarse grain structure of our specimen. Normally we should expect the flow stress to increase with increasing strain velocity, but the measured data seems to indicate a random pattern. This certainly indicates a very low strain rate dependency, and possibly that locally increasing temperatures counteract the effect of strain rate hardening. A parametric study on C should therefore be performed if the model is to be used in future papers. The quasi parameters A, B, and n however, seems to be in good agreement with the material data from specimen 90-2.

5.3.6 Input material data for AL6061-T6 Aluminium

A [MPa]	B [MPa]	m	C	ϵ_0	W_c [Pa]
279.25	220.34	0.57	0.0042	1	90E6

Table 5.4: Johnson Cook parameters AL6061-T6

E [GPa]	$\rho[\frac{kg}{m^3}]$	ν	$C_p[\frac{J}{kg*K}]$	$T_m[K]$	$T_c[K]$	$\alpha[\text{K}^{-1}]$
70	2700	0.33	900	933	855	2.3E-5

Table 5.5: Physical data AL6061-T6

Chapter 6

Experimental study of steel plates exposed to blast loading

Experimental studies of steel plates, AL-6XN, exposed to blast loading of 150 gram C4 have been done by Dharmasena et.al (2009). The experiment and its results will be described in this chapter. The experimental results will be compared with different numerical solutions in chapter 10.

The plates were fully edge clamped, and the charge was placed 150 mm, 200 mm and 250 mm from the target. The sides of the plate were 406 mm, the thickness 3.4 mm. Three different tests were done; bare charge, charge surrounded by dry sand, and charge surrounded by wet sand. The charge was packed inside inside a plastic sphere with radius 30 mm. The sand was not real sand, but consisted of silica glass microspheres with a diameter of ≈ 200 μm. The mass of the sand was approximately 2.7 kg, and surrounded the charge as a 46.2 mm shell.

The main focus in this thesis is bare charge. Charge surrounded by wet sand is totally neglected. The permanent central deflection of the plate was measured for each test, table 6.1. None of the plates failed as a result of the blast load. No shear deformation was observed at the plate boundaries, so the mode of deformation was assumed to be mode 1, see section 3.6. Consequently fracture was not an issue. The set up for the experiment is shown in figure 6.1.

Stand off distance	150 mm	200 mm	250 mm
Experiments - bare charge	17	12.7	11.3
Experiments - charge surrounded by dry sand	38.5	26.8	18.5

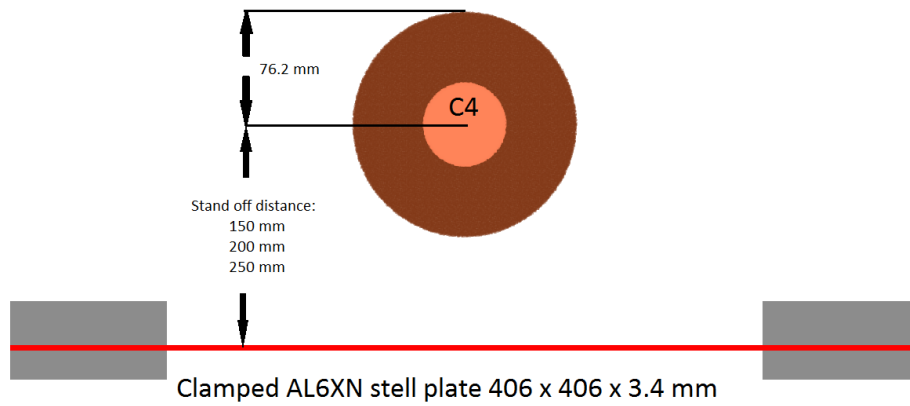Table 6.1: Experiments, Permanent central deflection

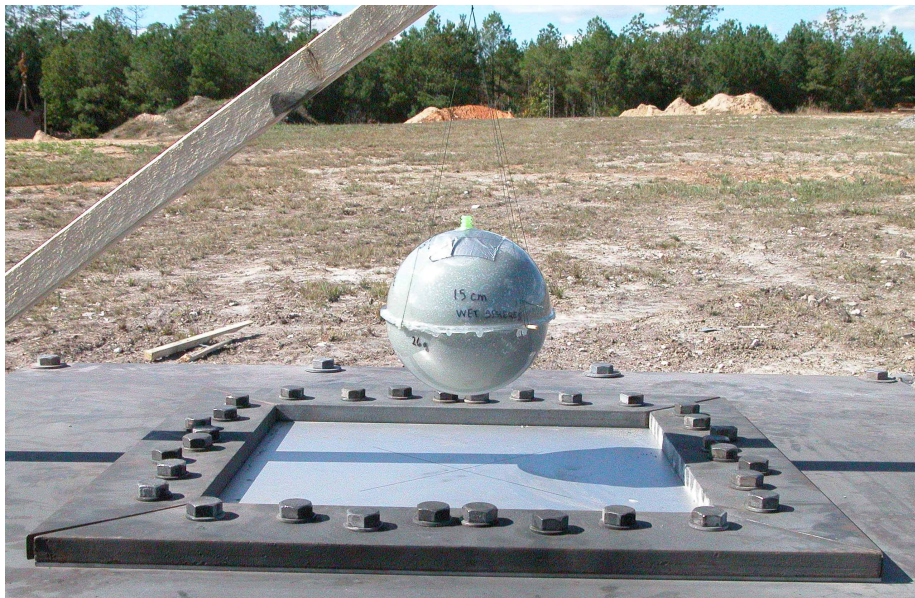Figure 6.1: Set up, steel plate exposed to blast loading [9]

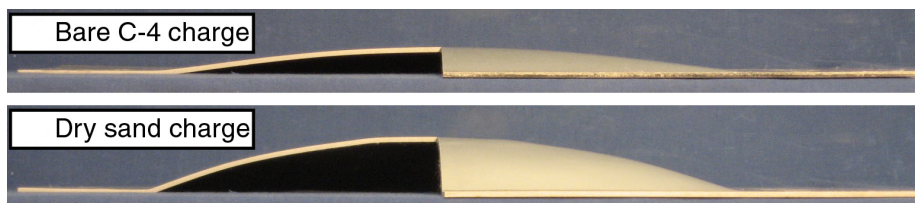Figure 6.2: Photo from experiment prior to detonation [9]

Figure 6.3: Permanent state of deformation, stand off distance 150 mm [9]

Chapter 7

Lagrangian method using Load Blast function in LS-DYNA

7.1 Motivation for the Load Blast function

In LS-DYNA, the ConWep blast charcteristics are implemented directly in the load blast function, ensuring that correct blast pressure is assigned at each node according to its distance from the blast source. The method is easy to use, little computational time is required, and the results may be very good when looking at blasts giving small deformations.

7.2 Numerical preliminaries

A number of different investigations were performed in the explicit finite element program LS-DYNA. The blast was simulated using the load blast function on a lagrangian mesh. The experimental set up utilized a charge of 150 grams of C4 and was scaled with the factor 1.19 to attain its impulse-equivalent in TNT. The finite elements considered were the 4 node quadrilateral belytscho-tsay shell element and the 8 node solid constant stress element. The plate was discretized using a mesh with elements roughly equal to the thickness; $3.38mm \times 3.38mm$ with 5 integration points for the shell, and 5 elements in thickness for the solid, figure 7.1 and figure 7.2.
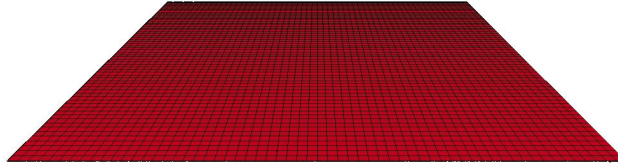
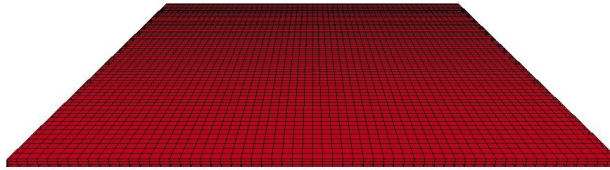Figure 7.1: Mesh for the shell computations

Figure 7.2: Mesh for the solid computations

7.3   Effect of mirroring

The quadratcic plate considered has symmetry along the x and y axis. Consequently a reasonable approach would be to mirror the soulution about the symmetry axes. However, there exists doubt wether or not this approach captures the physics of the problem. If shock waves arise within the steel plate, one effectivly neglects the transfer over the symmetry axes and the corresponding interaction effects that might occur. Wether or not this has any measurable effect was tested by comparing the Von Mises stress states for the whole plate with a mirrored quadrant at the time $t = 3.6ms$ for stand off distance 150 mm, figure 7.3. Shell elements were used.
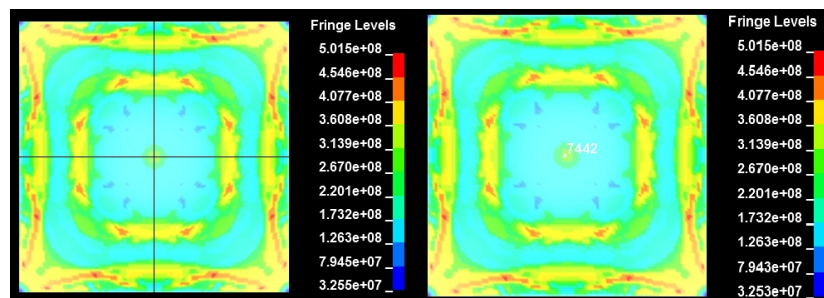
Figure 7.3: Stress states at t=3,6ms

The results indicated no difference in the stress states between the mirrored solution to the left and the whole plate to the right, figure 7.3. The conclusion must therefore be either that shock discontinuities are not present to any significant degree or that the physics is indeed captured by the mirroring.

7.4   Shell vs. Solid

The constant stress solid element formulation was compared to the Belytschko-Tsay shell element formulation. Figure 7.4 shows the time-displacement curve for stand off distance 150 mm, for the two different element formulations. The two formulations gave approximately the same answer. Shell elements were less CPU demanding, and were therfore adopted in the further study, table 7.1.

Element formulation/ mesh	1/4 Shell	1/4 Solid	1/1 Shell
Elapsed time	3 min	17 min	11 min

Table 7.1: Elapsed time for shell and solid elements, time period 5 ms
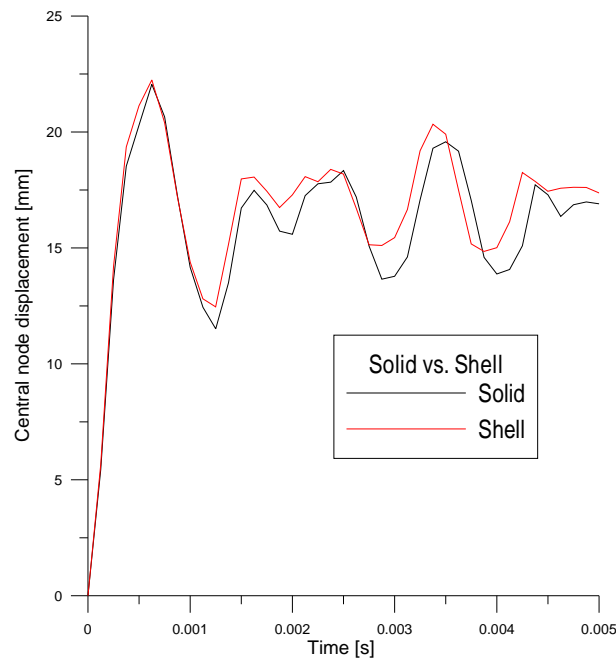
Figure 7.4: Central node displacement, stand off distance 150 mm, Solid vs. Shell

7.5   Mesh effects

Different element sizes have been tested to see the effect on the central node displacement; 3.38 mm, 6.77 mm, and 20.3 mm, figure 7.5. The stand off distance was 150 mm. One can conclude that the solution is pretty mesh-size independent. The maximum deflection is equal for all cases, while the oscillations after ended loading has some variations. To have elements equal to the thickness seemed to be meaningless this case, but is used anyways thanks to low computational costs
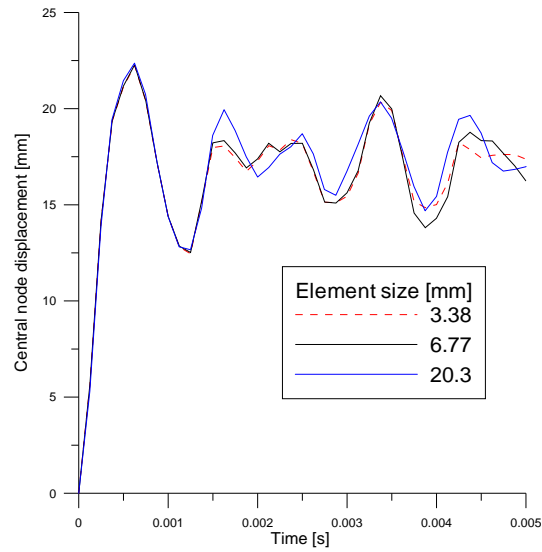
Figure 7.5: Central node displacement for different shell element sizes, stand off distance 150 mm

7.6   Reflected Impulse

The reflected impulse per m^2 was calculated by multiplying the average velocity to the non-constrained plate with the mass per m^2, figure 7.6.
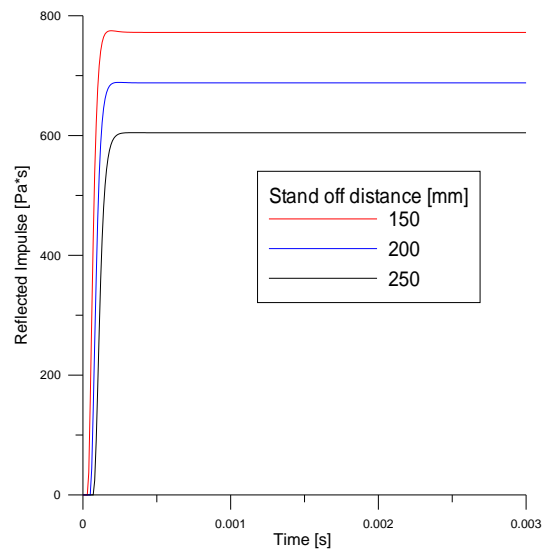

Figure 7.6: Reflected impulses using load blast function in LS-Dyna

7.7 LS-DYNA blast function vs. Uniform pressure from ConWep

The load blast function is not commonly found in other FEM programs. To consider blast using these programs the usual approach is to assume a uniform pressure field on the side facing the blast. This pressure is typically based on the stand off distance and will yield overly conservative results. A number of tests were performed using the load blast function in LS-DYNA, with a charge of 150 g C-4 and stand off distance 0.2, 0.6, 1, 1.4, 1.8, 2.2 m. The obtained reflected impulses were compared to the reflected impulses obtained by using uniform pressure from ConWep [16].
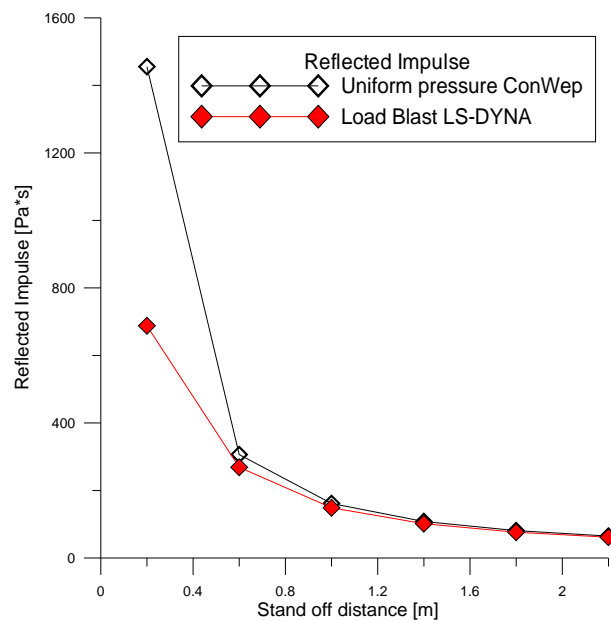

Figure 7.7: Reflected impulse, load blast function in LS-DYNA vs. Uniform pressure from ConWep

The results, shown in figure 7.7, indicated that severly conservative estimates will be obtained if one chooses to employ a uniform pressure field on very small stand of distances.

7.8   Energy

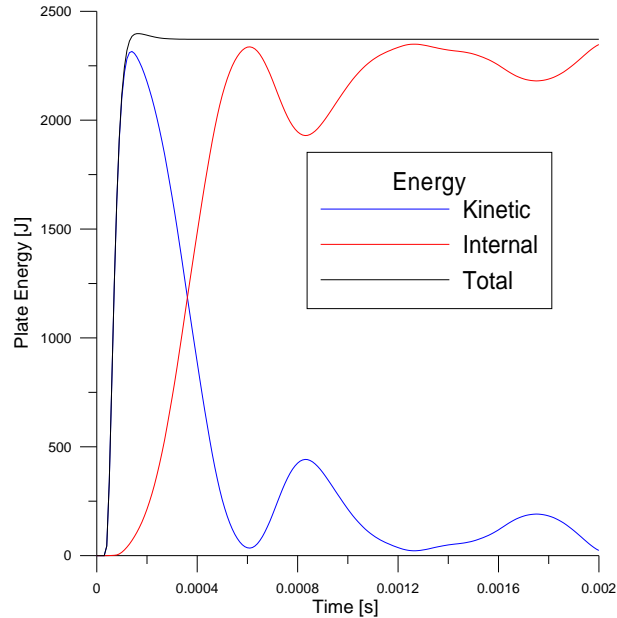No problems concerning the plate energy are observed, 7.8.

Figure 7.8: Plate energy, stand off distance 150 mm

7.9   Failure

When using the load blast function in LS-DYNA to investigate small deformations on a plate due to blast, one can expect good results. On the other hand, when looking at problems concerning large deformations and material failure of mode II and III (section 3.6), the load blast function may give very conservative results, see section 3.1 and 3.4. This could be interesting to compare with results from other numerical methods, e.g. ALE and the Corpuscular method. In contrast to the earlier analysis where element type and size had little to none influence, analysis dealing with failure mode II and III are very mesh dependant.

Several analysis with duration 3 ms have been done to see what charge of C4 was needed to cause failure mode IIa, full tensile tearing over the entire support area. The 1/4 symmetry model with both shell elements (5 integration points) and solid elements (5 elements in thickness) have been used. The fracture criterion is described in section 5.2.1. The resulting charges of C4 are represented in table 7.2. To get the equivalent TNT values scaled with respect to impulse, which are the input to LS-DYNA, one must multiply with 1.19.

Stand off distance	150 mm	200 mm	250 mm
Charge C4 [kg] SHELL element size 5.08 mm	≈ 0.55	≈ 0.73	≈ 0.92
Charge C4 [kg] SHELL element size 3.38 mm	≈ 0.46	≈ 0.61	≈ 0.79
Charge C4 [kg] SHELL element size 2.54 mm	≈ 0.42	≈ 0.55	≈ 0.71
Charge C4 [kg] SOLID element size 5.08 mm	≈ 0.65	-	-
Charge C4 [kg] SOLID element size 3.38 mm	≈ 0.65	-	-

Table 7.2: C4 charge giving total failure (mode IIa)

Having no experimental data concerning this, it is impossible to say whether the results are credible or not. Shell elements do not seem to be suitable for material failure of mode II and III. Convergence is not obtained, and full tensile tearing along the edges appears for much lower charges than when using solid elements. From the results obtained using shell elements, figure 7.9, the charge giving failure mode IIa seems to increase linearly with stand off distance. For solid elements convergence is obtained.
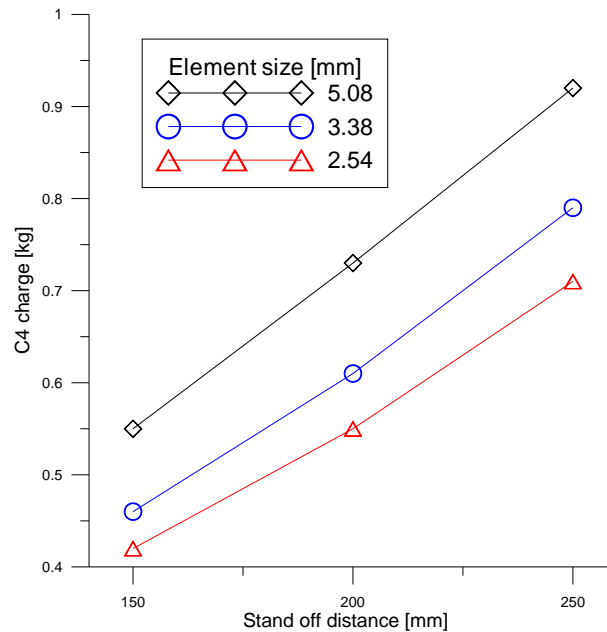

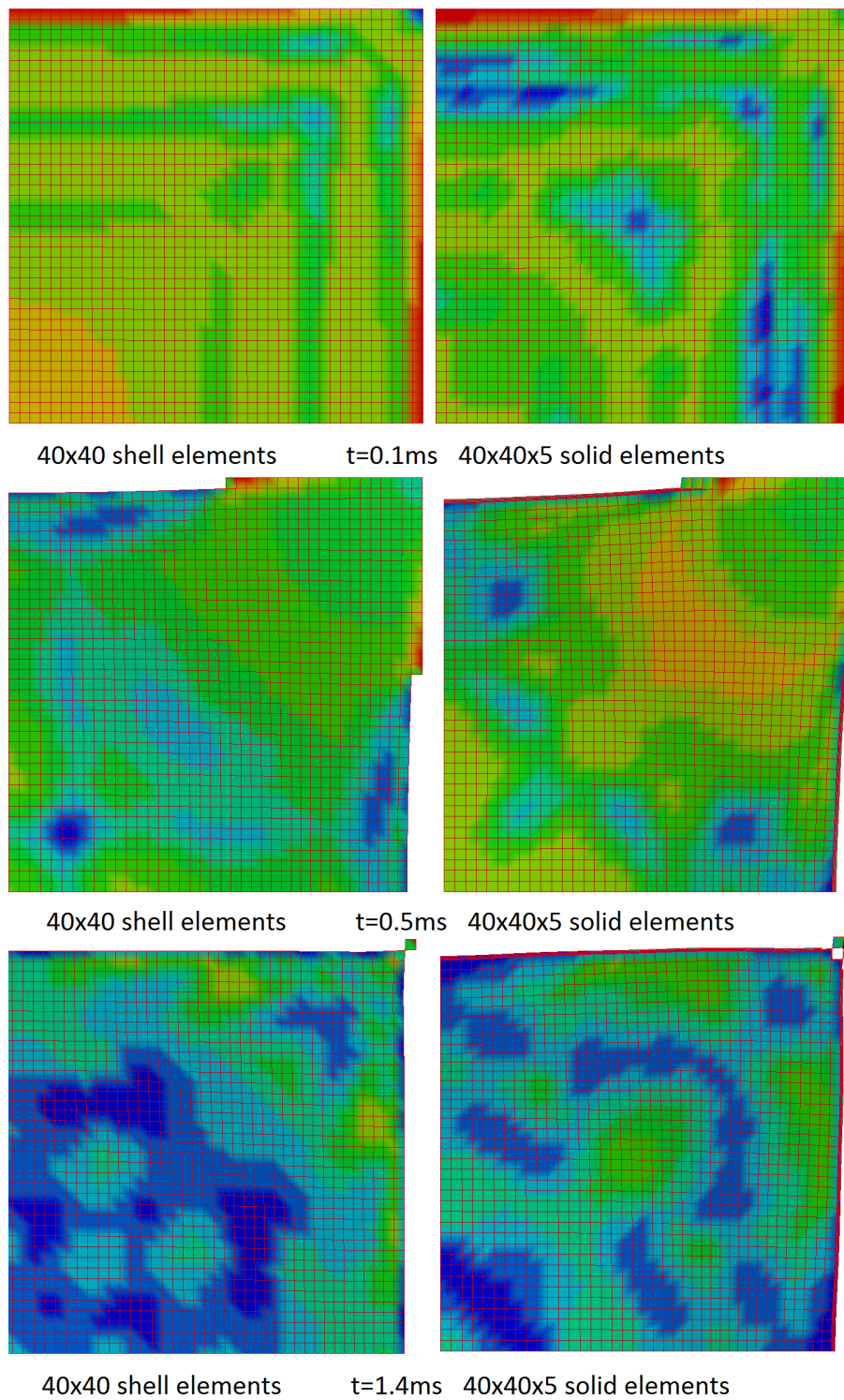Figure 7.9: C4 charge giving total failure (mode IIa) using shell elements

40x40 shell elements   t=0.1ms   40x40x5 solid elements

40x40 shell elements   t=0.5ms   40x40x5 solid elements

40x40 shell elements   t=1.4ms   40x40x5 solid elements

Figure 7.10: Failure mode IIa, C4 charge 0.55 g for shell elements and 0.65 g for solid elements, element size 5.08 mm

Chapter 8

ALE method for blast loading in LS-DYNA

8.1 Motivation for the ALE method

In the previous section the Lagrangian analysis was based on the LS-DYNA Load Blast function. A major assumption of this formulation is that the blast wall is infinitely rigid such that the wall stiffness and mass properties have little influence on the reflected pressure. However, according to the kinetic theory of gases, equation 4.61, the pressure on a plate is given by the air particles impacting the plate and transfering momentum. Consequently if a plate attains significant velocities, the impulse and pressure is reduced. In practial terms, this means that a thin plate will attain greater speeds during blast loading and thus experience less impulse than a thicker plate. This is of great importance to engineers as the fact can be exploited to create more optmized thin walled structures.

8.2 Solution strategy

Proper control of the ALE function in LS-DYNA is far from effortless and requires a significant amount of tweaking of input parameters. The chosen solution strategy is therefore an attempt to remove some of the complexity by splitting the problem in two. The first part consists of tweaking the ALE mesh size and switching ALE control cards in order to replicate the incident pressure and impulse expected in a free air blast. The obtained impulse and pressure are then validated against results from ConWep. The second part consists of coupling the air blast model to a constrained plate. In this section parametric studies will be performed on increasing mesh refinement both for the air and plate. There will also be studies on several keycards controling the contact and ALE formulation, to ensure no leakage and appropriate transfer of impulse to the plate.

8.3   Free air blast

8.3.1   Geometry and constraints

The initial air mesh configuration was chosen as cubic. In order to reduce computational time and allow for high mesh refinement, constraints were imposed normal to the x-y, x-z and y-z planes such that 1/8 of the blast was considered, figure 8.1. This approach was verified in the case ALE blast modeling for aluminium foam models [21], where little difference was found between considering the whole domain and a symmetry based model. The mesh for the air domain is constructed using a matlab program which defines nodes, elements and constraints, and is included in appendix A.
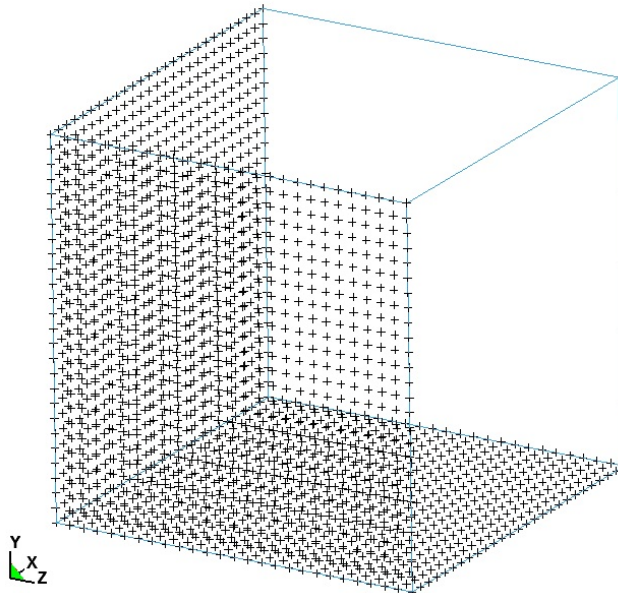
Figure 8.1: Reflective boundary conditions imposed on cube

8.3.2   Material

The cube consists of two materials, air and C4. The *ale-multi-material-group defines the two materials. The air is given a density using *mat-null, and the C4 is defined using *mat-high-explosive-burn, which controls the explosive's detonation characteristics. The *inital-volume-fraction-geometry card defines the initial distribution of air and C4. It also defines where the C4 i placed, and its intial shape. Initial detonation defines where and when the detonation starts. Both the air and explosive are treated as 1 point multi material ALE elements.

8.3.3 Air domain control parameters

In the *control-ale-keycard the Van Leer scheme with half index shift is selected with one timestep between mesh smoothing and advection. The method of mesh smoothing is selected as simple averaging. In the *ale-reference-system card the option for mesh contraction in the vicinity of the shock front is considered. This keycard requires an input of the parameter EFAC which determines the initial mesh remapping factor [14]. The EFAC factor is a chosen between 1 and 0, where 1 is a fully Eulerian inital blast treatment, and 0 is fully Lagrangian initial blast treatment. By utlizing a low value Lagrangian approach one may be able to escape the smearing of Eulerian methods and attain higher and more realistic impulses and pressures. There is however a penalty as distorted elments leads to timestep reduction and possible program termination. A parameter study will be performed regarding the EFAC factor at a later point in this chapter.

The *constrained-lagrange-in-solid-keycard is used to couple the air domain to the plate, and the Penalty method is utlized as the contact algorithm with suitable amount of interface points to prevent leakage. As the unit normal of a shell element is defined by wether or not the nodes are numbered clockwise or counterclockwise, the unit normal for the contact alogrithm is defined such that it faces the blast source [27].

8.3.4 Open space incident pressure and impulse

The incident pressure is recorded using the tracer function in Ls-DYNA. A problem with the tracer function is that it adds atmospheric and overpressures together. They are consequently removed by subtracting the atmospheric pressure from the incident pressure and the integral from the incident impulse during the positive phase duration. The sensors are located along two series, figure 8.2 and figure 8.3, such that they are at the same distance from the blast source.

Sensor	x-coord	y-coord	z-coord
Sensor 1	0.15m	0	0
Sensor 2	0.20m	0	0
Sensor 3	0.25m	0	0

Table 8.1: Sensor series 1

Sensor	x-coord	y-coord	z-coord
Sensor 1	0.087m	0.087m	0.087m
Sensor 2	0.115m	0.115m	0.115m
Sensor 3	0.144m	0.144m	0.144m

Table 8.2: Sensor series 2

For the mesh convergence analysis, the number of elements per length is increased by a factor of 2.25 for each analysis. The analysis time period is determined to be 3 ms. According to Lars Olovsson [27] a mesh of size 3 mm with constant aspect ratio would be sufficient for this analysis. Consequently, one of the meshes is selected to be finer and the other 2 coarser than this.

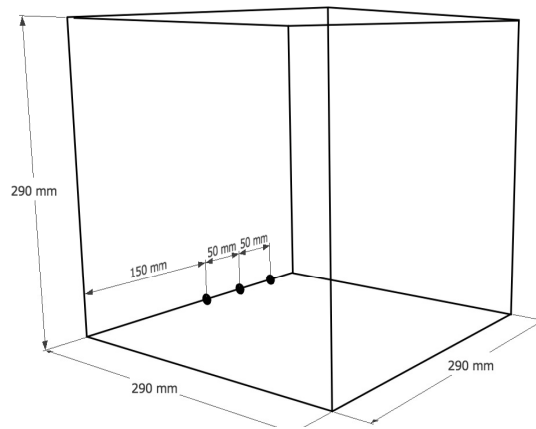| Name	Element lenght	Domain size	Number of elements
Coarse	10mm	$0.26^3 m^3$	17576
Medium	4.44mm	$0.26^3 m^3$	195112
Fine	1.98mm	$0.26^3 m^3$	2248091

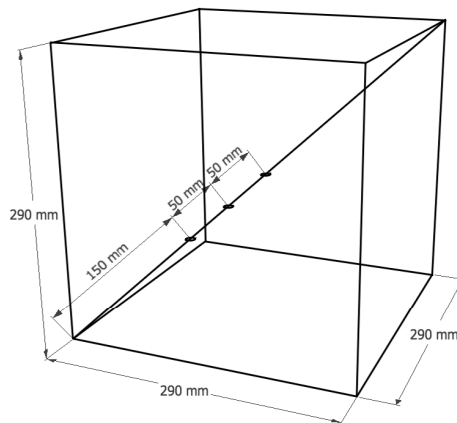Table 8.3: Mesh selection for open space incident

Figure 8.2: Sensors in series 1
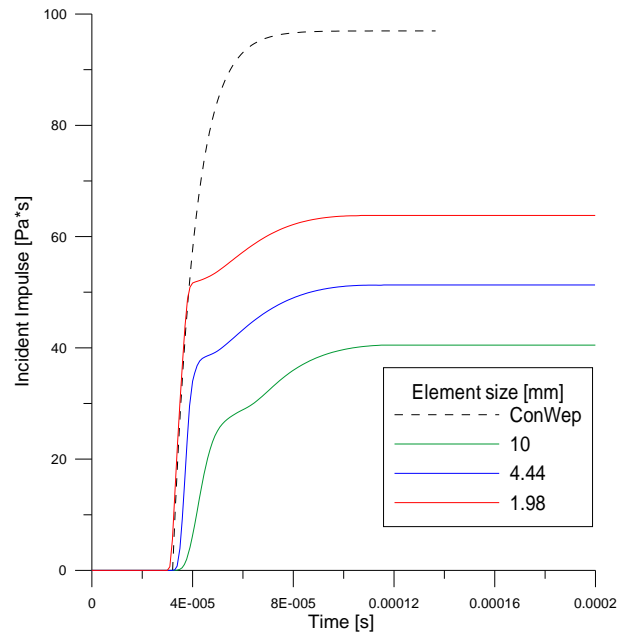

Figure 8.3: Sensors in series 2

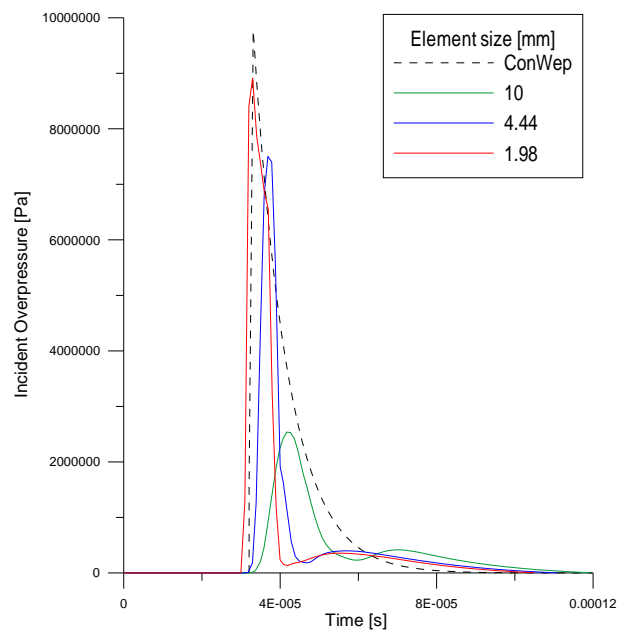Figure 8.4: Incident Impulse series 1, Stand off distance 150 mm
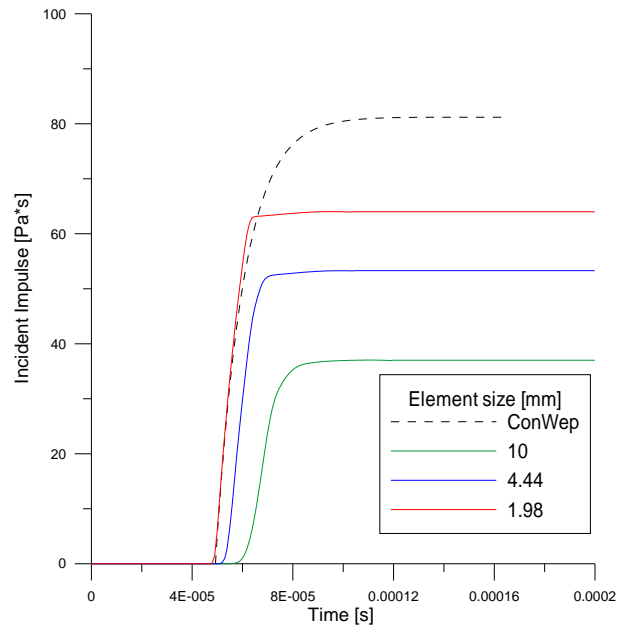

Figure 8.5: Incident Overpressure series 1, Stand off distance 150 mm

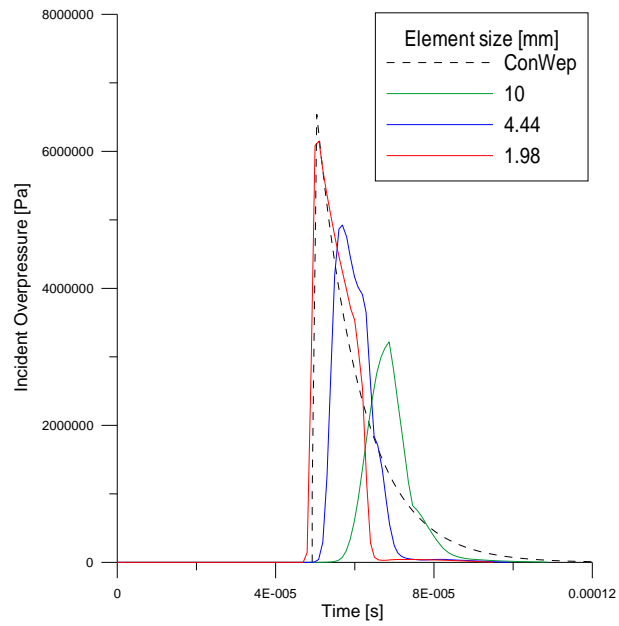Figure 8.6: Incident Impulse series 1, Stand off distance 200 mm

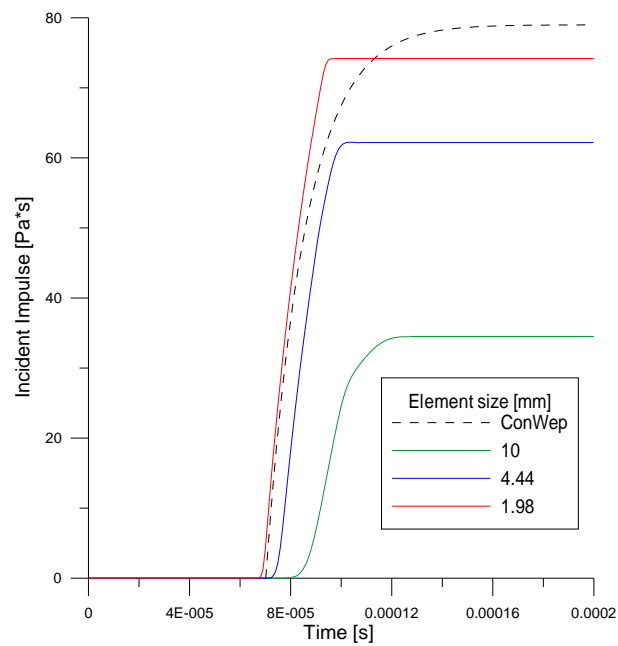Figure 8.7: Incident Overpressure series 1, Stand off distance 200 mm

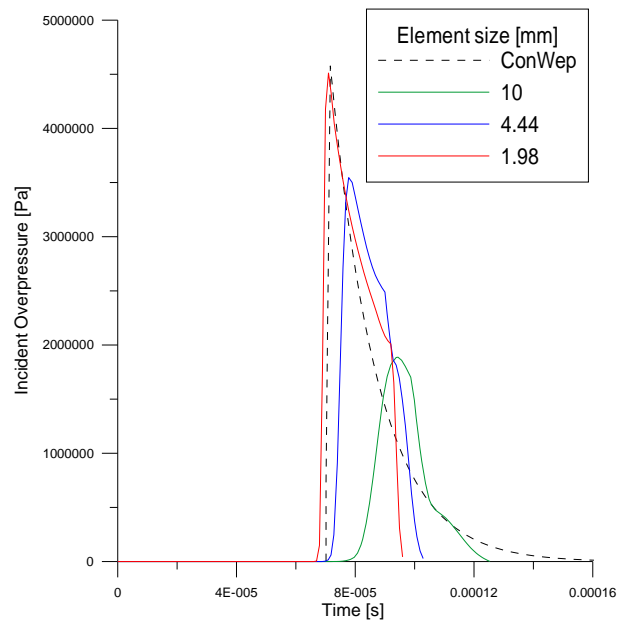Figure 8.8: Incident Impulse series 1, Stand off distance 250 mm

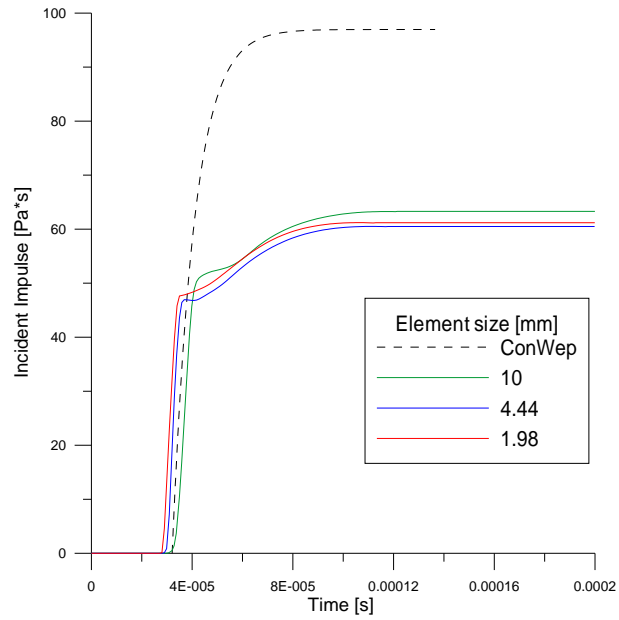Figure 8.9: Incident Overpressure series 1, Stand off distance 250 mm

Figure 8.10: Incident Impulse series 2, Stand off distance 150 mm
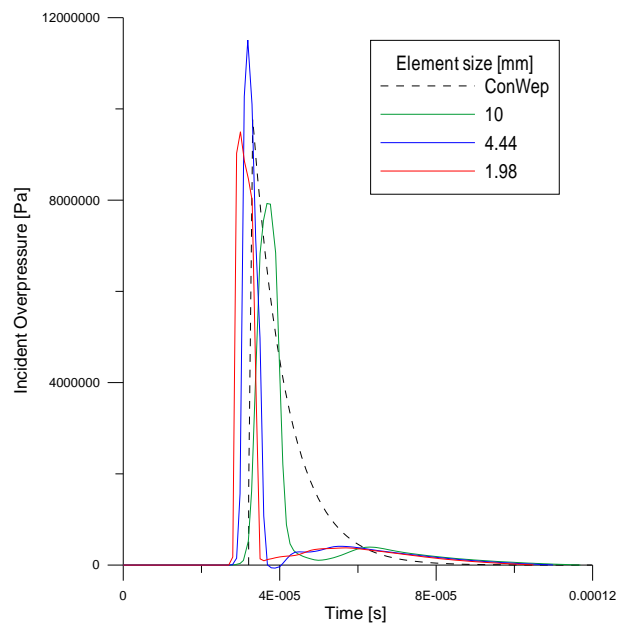

Figure 8.11: Incident Overpressure series 2, Stand off distance 150 mm
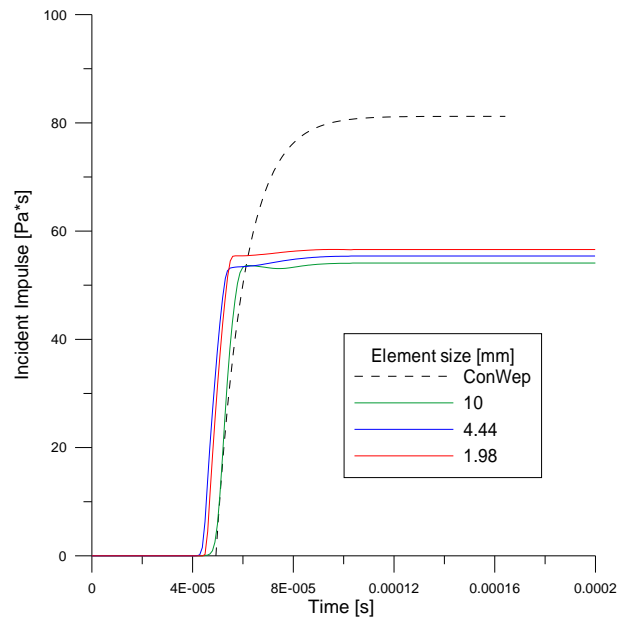
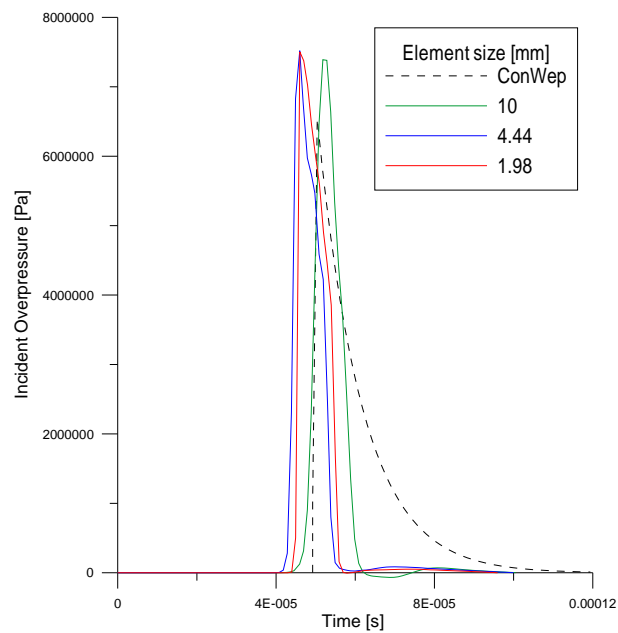Figure 8.12: Incident Impulse series 2, Stand off distance 200 mm

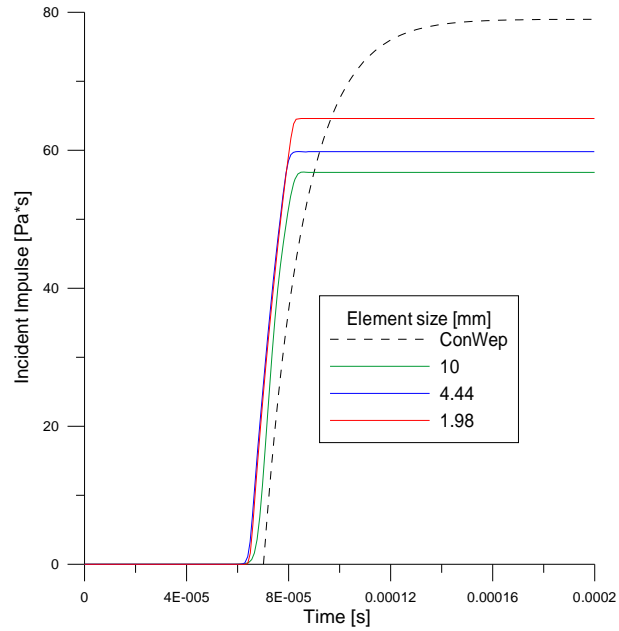Figure 8.13: Incident Overpressure series 2, Stand off distance 200 mm

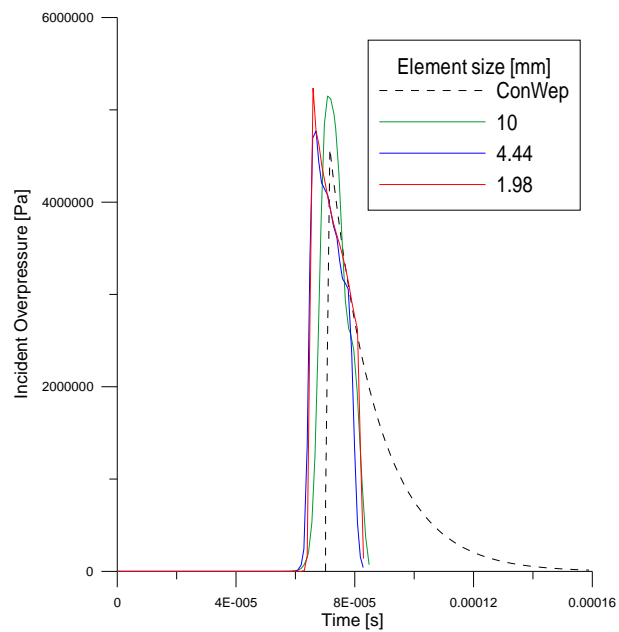Figure 8.14: Incident Impulse series 2, Stand off distance 250 mm

Figure 8.15: Incident pressure series 2, Stand off distance 250 mm

Analysis 150 mm	Element size [mm]	ALE Element count	Peak Incident Overpressure [kPa]	Incident Impulse [Pa*s]	Elapsed time [min]
1	10	17576	2537	40.5	5
2	4.44	195112	7501	51.3	25
3	1.98	2248091	8917	63.8	NA

Table 8.4: Incident Overpressure and Impulse series 1, stand off distance 150mm

Analysis 200 mm	Element size [mm]	ALE Element count	Peak Incident Overpressure [kPa]	Incident Impulse [Pa*s]	Elapsed time [min]
1	10	17576	3220	37	5
2	4.44	195112	4930	53.3	25
3	1.98	2248091	6149	64	NA

Table 8.5: Incident Overpressure and Impulse series 1, stand off distance 200mm

Analysis 250 mm	Element size [mm]	ALE Element count	Peak Incident Overpressure [kPa]	Incident Impulse [Pa*s]	Elapsed time [min]
1	10	17576	1887	34.5	5
2	4.44	195112	3546	62	25
3	1.98	2248091	4513	74.2	NA

Table 8.6: Incident Overpressure and Impulse series 1, stand off distance 250mm

Analysis 150 mm	Element size [mm]	ALE Element count	Peak Incident Overpressure [kPa]	Incident Impulse [Pa*s]	Elapsed time [min]
1	10	17576	7925	63	5
2	4.44	195112	11510	61	25
3	1.98	2248091	9499	61	NA

Table 8.7: Incident Overpressure and Impulse series 2, stand off distance 150mm

Analysis 200 mm	Element size [mm]	ALE Element count	Peak Incident Overpressure [kPa]	Incident Impulse [Pa*s]	Elapsed time [min]
1	10	17576	7390	54	5
2	4.44	195112	7521	55	25
3	1.98	2248091	7503	57	NA

Table 8.8: Incident Overpressure and Impulse series 2, stand off distance 200mm

Analysis 250 mm	Element size [mm]	ALE Element count	Peak Incident Overpressure [kPa]	Incident Impulse [Pa*s]	Elapsed time [min]
1	10	17576	5150	57	5
2	4.44	195112	4772	60	25
3	1.98	2248091	5235	65	NA

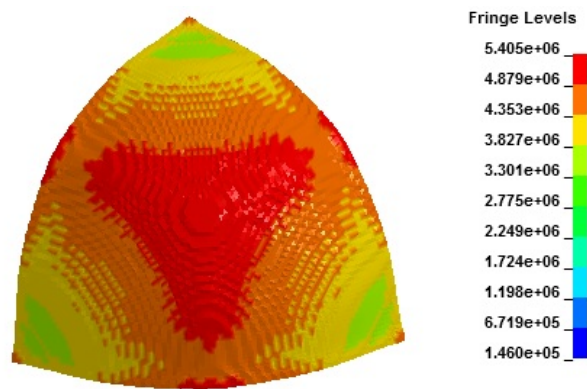Table 8.9: Incident Overpressure and Impulse series 2, stand off distance 250mm

Figure 8.16: Pressure variations in the expansion wave, 1/8 symmetry model at t=4.98E-5s, Element lenght=2.96mm

Figure 8.17: Pressure variations at the expansion wave, 1/8 symmetry model at t=4.98E-5s, Element lenght=1.98mm
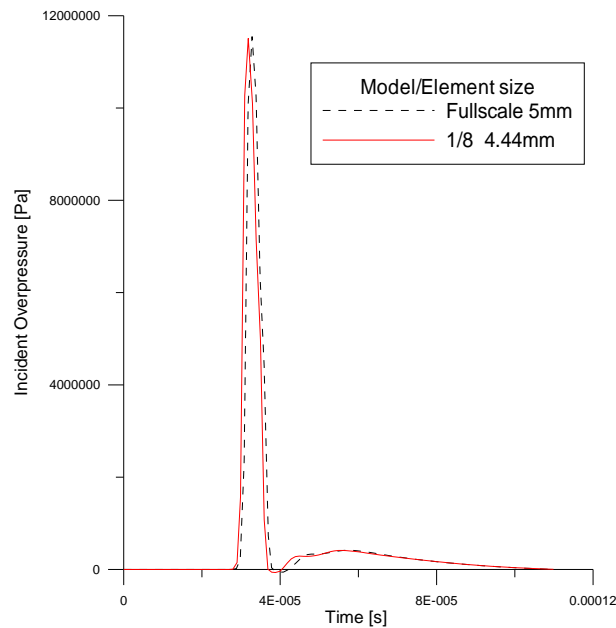
Figure 8.18: Incident overpressure 1/8 symmetry model vs. Fullscale model

8.3.5   Discussion

The results indicate generally increasing impulse with increasing mesh refinement and slightly varying impulse with stand of distance. Generally, standoff distance 200 mm seemed to have the lowest impulse and standoff distance 250 mm seemed to have the highest. The agreement with ConWep seemed to get better with increasing stand off distance, and increasing mesh refinement. The sensors in series 2 seem to converge for coarse meshes, while the sensors in series 1 do not converge at all. This may be caused by the reflective boundary conditions imposed directly adjacent to the sensors at series 1. To check if the reflective boundary conditions cause any significant errors in analysis, the quarter scale model was compared to a fullscale model of roughly the same refinement. The obtained pressure histories from standoff distance 150mm figure **??**, gave identical results. From figure 8.16 and figure 8.17 there can be seen a region of higher pressure close to the boundaries. This overpressure probably causes some distortion in the expansion wave as the speed of sound increases. It is therefore probable that the reflective boundary condtions have some influence, but only to the extent of a few elements close to the boundary.

The pressure pattern shows large differences in pressure at surface of the expansion wave. According to Svein Christensen of The NDEA, this pattern might be caused by two things. Either Richtmeyer-Meshkov instabillities which is a physical phenomenon occuring at the surface of the expansion wave, or unsufficient mesh refinement of the explosive charge. The unsufficient refinement leads to micro jet beams which may effect the pressure locally close to the blast source. It is believed that this is the source of the weird pressure pattern as definite

improvement is seen with increasing refinement figure 8.17, figure 8.16.

Svein Christensen suggested defining pressure sensors at the same stand off distances but at different angles relative to the charge, and compare the results in terms of pressure and impulse. This is the motivation for the two different sensor series.

For sufficiently small differences the analysis is probably ok. As seen in table 8.4 to 8.8, the difference between the sensors at the same stand off distance is getting gradually less with increasing mesh refinement.

In terms of blast arrival time the sensors along the diagonal in series 2 are slightly off compared to ConWep data. The expansion wave seems to be attaining a somewhat square form as it expands. It is probable that the expansion wave travels slightly faster along the diagonal because of the pressure instabillities.

8.3.6   Study on the E-factor

It could be interesting to consider the mesh contraction option and see if variation of the E-factor has any influence on the shock front pressure issues. The study is performed on a 1/8 symmetry model utilizing elements with constant aspect ratios and side lenghts $l_e = 4.44mm$. The sensor location was chosen as 150mm along the diagonal axis as in series series 2. The E-factors were chosen as: 0.025, 0.10, 0.25 and 0.5.

Even though variations of the E-factor gave large differences in terms of impulse and pressure, it is not clear at this point if it should be included any further in the model. The factor basically allows for more Lagrangian behaviour in the initial blast which for some EFAC values resulted in larger pressures and impulses. However, for the smallest EFAC value of 0.025, the impulse actually decreased and the pressure was found to be decreasing for EFAC values less than 0.25. The computational time was also increasing with decrasing EFAC values, indicating that severe element distortion was taking place. It might be possible that the E-factor would be more well behaved for finer meshes, but this has currently not been considered.
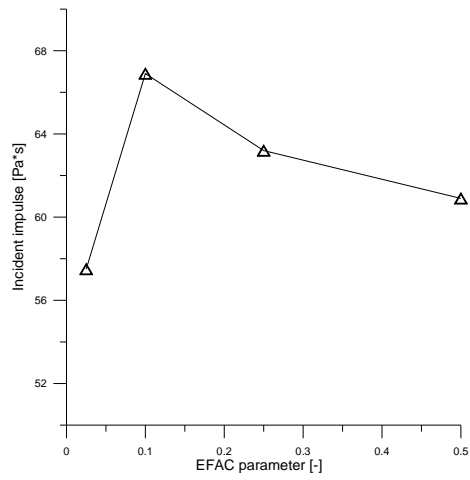
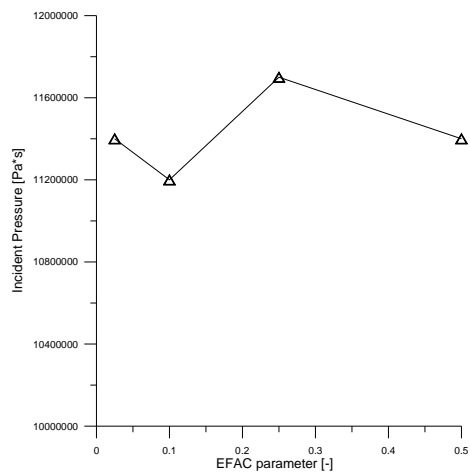Figure 8.19: Incident impulse distrubution t=3.99E-5 s, stand off distance=150 mm, sensor series 2

Figure 8.20: Pressure distrubution t=3.99E-5 s, stand off distance=150 mm, sensor series 2

8.4   Blast on plate

In this section three computational models are considered. A fullscale model, a 1/8 symmetry model with reflective boundary conditions, and a 1/8 biased symmetry model.
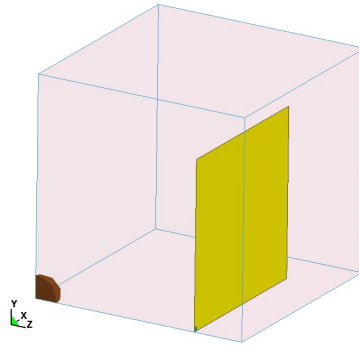

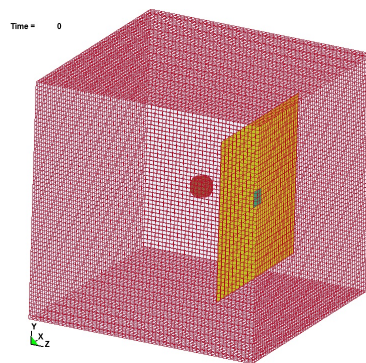Figure 8.21: 1/8 symmetry model
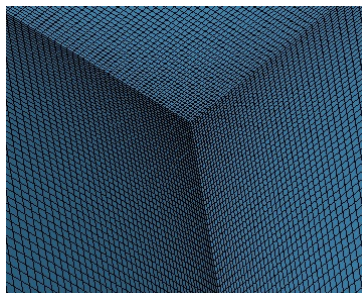

Figure 8.22: Fullscale model

Figure 8.23: 1/8 biased symmetry model, close to blast source

8.4.1   Geometry, constraints and Element sizes

Two studies on a fullscale model with fine and coarse element sizes have been performed. Finally a biased 1/8 symmetry model was used to attain reduction of the compuational times.

Model	Element length	Bias	Domain size	Number of elements
Fullscale coarse	10mm	-	$0.6^3 m^3$	216000
Fullscale fine	5mm	-	$0.6^3 m^3$	1728000
1/8 symetry bias	3mm	1%	$0.3^3 m^3$	343000

Table 8.10: Air mesh selection for reflected pressure/impulse

The plate elements were chosen as twice the size of the ALE elements for the fullscale model. For the 1/8 symmetry model the plate elements were chosen as smaller than the ALE elements. This was done to check the influence of the plate elements on the calculation.

Model	Element length	Dimensions	Number of elements
Fullscale coarse plate	20.3mm	$0.406m$	400
Fullscale fine plate	10.15mm	$0.406m$	1600
1/8 symmetry plate	2.03mm	$0.203m$	10000

Table 8.11: Plate meshes for reflected pressure/impulse

8.4.2   Reflected Pressure and Impulse

Stand off distance [mm]	Peak Reflected Pressure [kPa]		Reflected Impulse [Pa*s]		CPU time [min]		Time Period [ms]
Mesh model	coarse	fine	coarse	fine	coarse	fine	
150	14015	15229	688	742	56	1114	2
200	10786	12310	667	748	75	1445	3.5
250	8278	10580	694	805	45	1068	3.5

Table 8.12: ALE, Average Reflected Pressure and Impulse, Fullscale model

Stand off distance [mm]	Peak Reflected pressure [kPa]	Reflected Impulse [Pa*s]	CPU time [min]	Time period [ms]
150	13660	704	NA[1]	-
200	11500	739	NA	-
250	10480	812	NA	-

Table 8.13: ALE, Average Reflected Pressure and Impulse, 1/8 symmetry biased model

---

[1]The analysis was unable to run to completion because of segmentation error or stable timestep moving towards zero
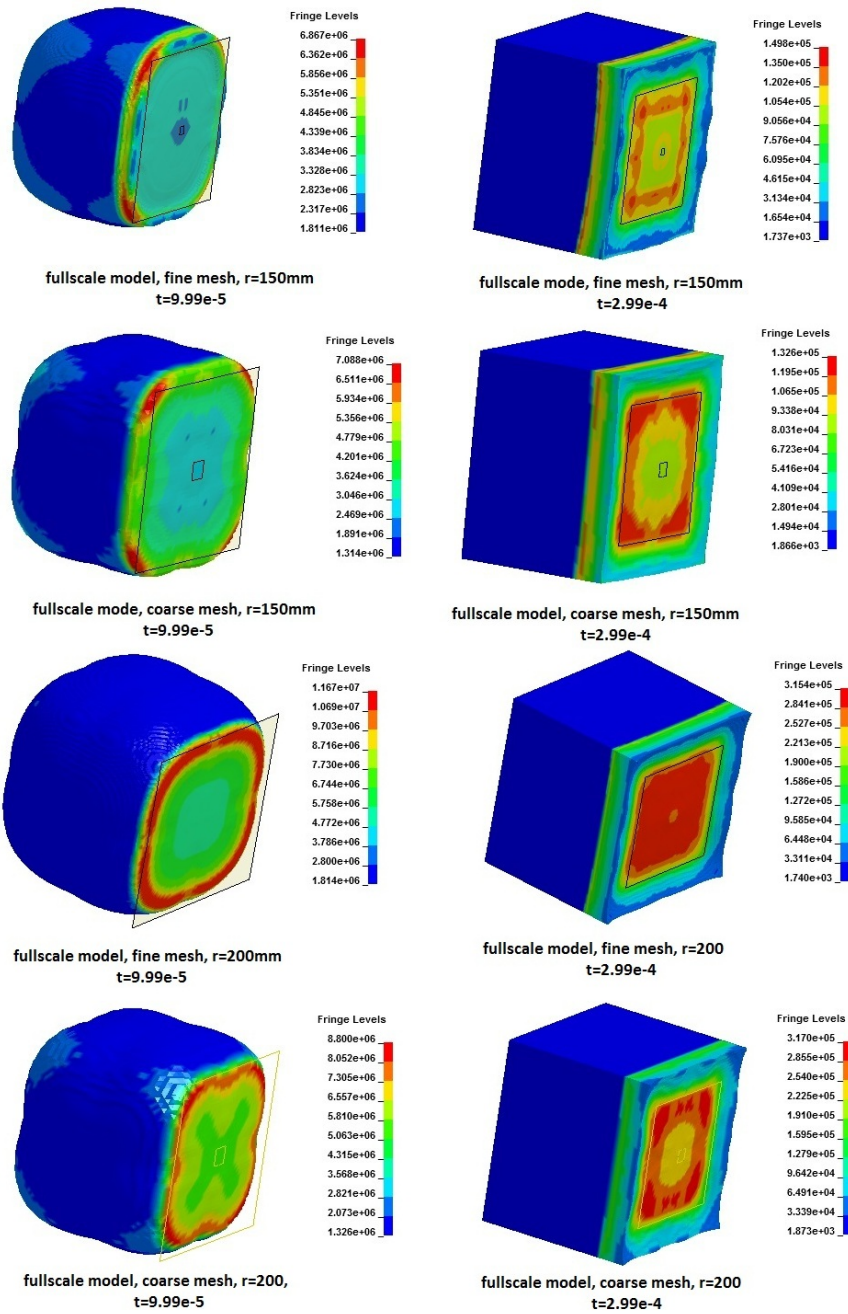
Figure 8.24: FSI for fullscale coarse and fine meshes, R=150mm and R=200mm, t=9,99e-5 s and t=2,99e-4 s

fullscale model, fine mesh, r=250
t=9,99e-5

fullscale model, fine mesh, r=250mm
t=2,99e-4

fullscale model, coarse mesh, r=250
t=9,99e-5

fullscale model, coarse mesh, r=250
t=2.99e-4
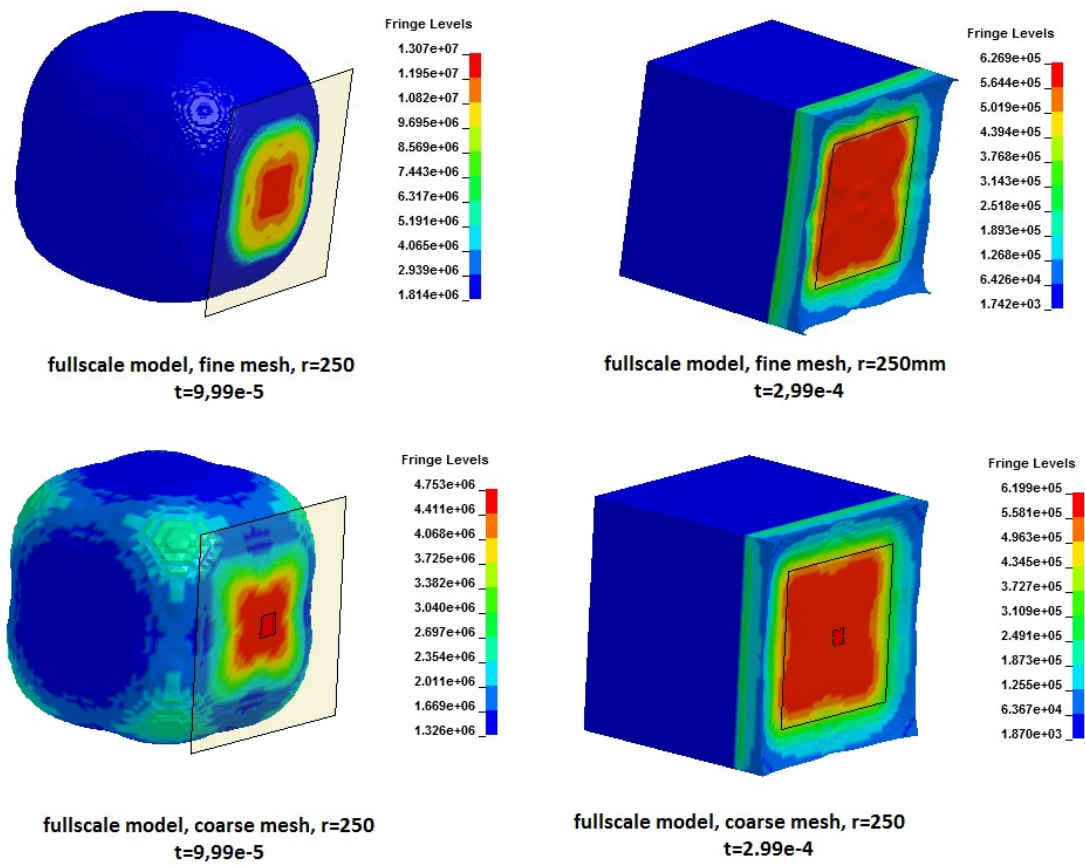
Figure 8.25: FSI for fullscale coarse and fine meshes, R=250, t=9,99e-5 s and t=2,99e-4 s
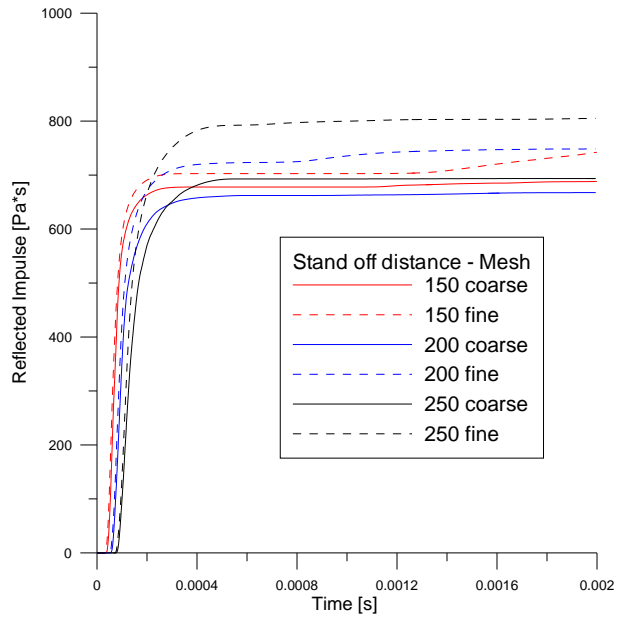
Figure 8.26: Reflected impulse, ALE fullscale model
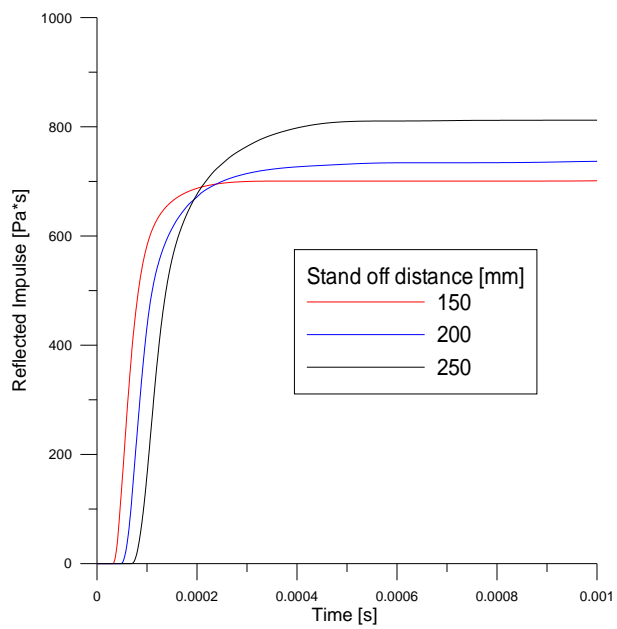
Figure 8.27: Reflected impulse, ALE 1/8 symmetry model
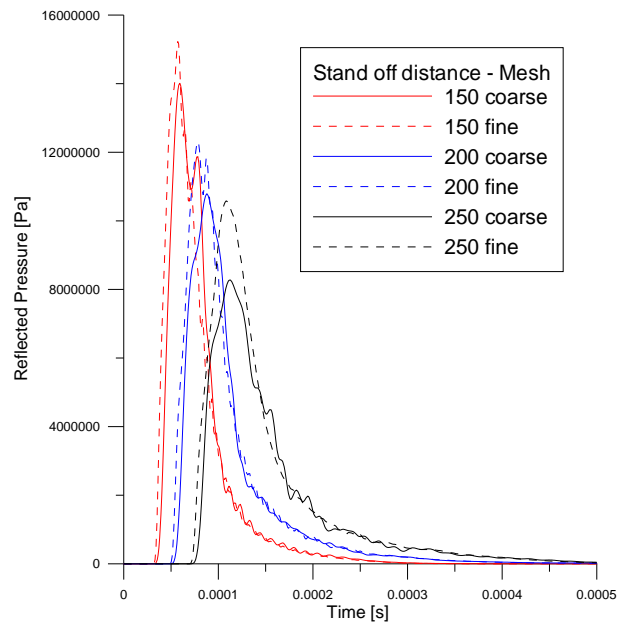
Figure 8.28: Reflected pressure, ALE fullscale model
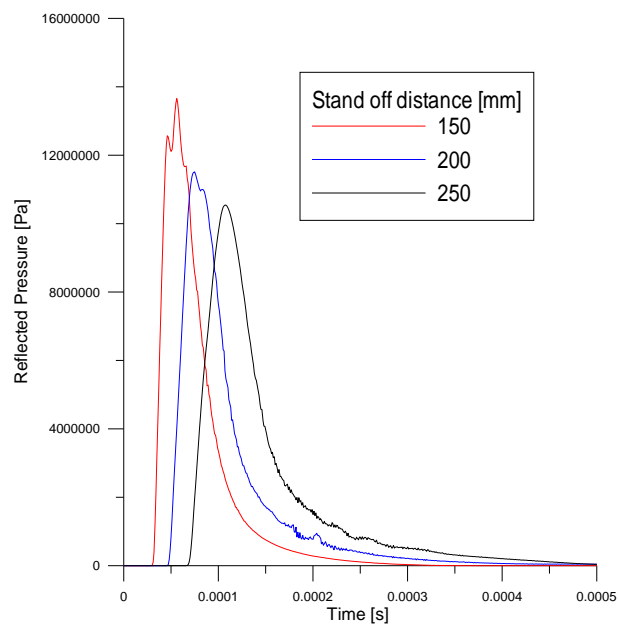
Figure 8.29: Reflected pressure, ALE 1/8 symmetry model

8.4.3 Energy levels
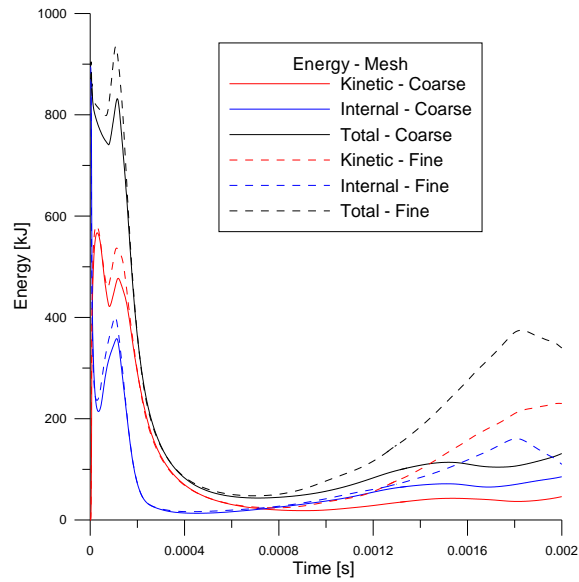
Figure 8.30: Energy plots blast on plate, fullscale, stand off distance 150 mm

Figure 8.31: Energy plots blast on plate, fullscale, stand off distance 200 mm

Figure 8.32: Energy plots blast on plate, fullscale, stand off distance 250 mm

Figure 8.33: Sliding energy, fullscale

Figure 8.34: Total energy, 1/8 symmetry model

Figure 8.35: Sliding energy, 1/8 symmetry model

8.4.4   Discussion

Mesh refinement and convergence

The reflected impulse is generally increasing with stand off distance. This is probably a bad sign, as according to TM5-855-1 (figure 3.5), the reflected impulse should be decreasing for all stand off distances considered in this paper.

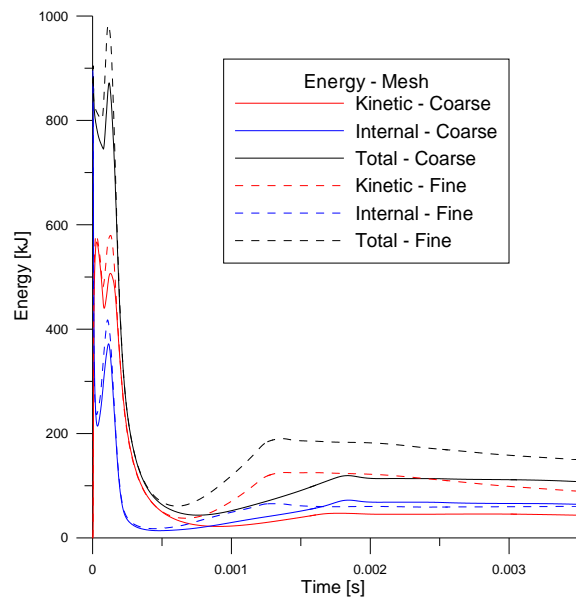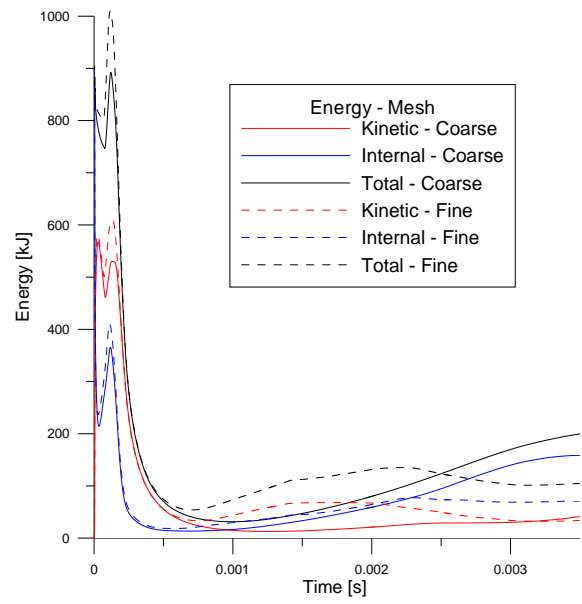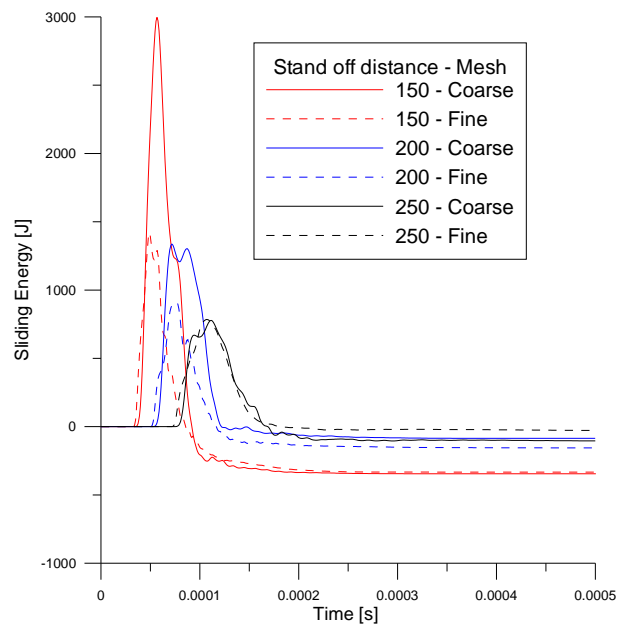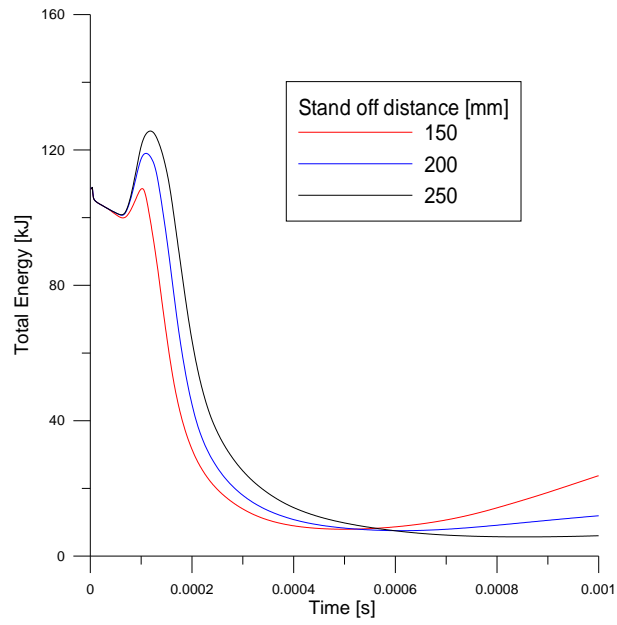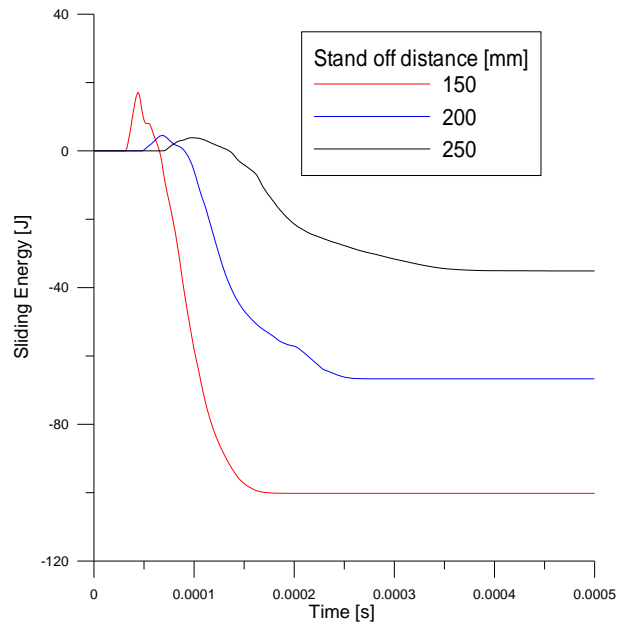This trend seem to be increasing with mesh refinement. There are indications that there is some degree of numerical contact energy being introduced to the system. Further mesh refinement was impractial for the fullscale model as the number of elements already was in the millions. As seen in table 8.12 the computational times were prohibitively large. A 1/8 symmetry model with further mesh refinement was consequently adopted. In this configuration the plate mesh was selected as slightly finer than the air mesh.

When comparing the fullscale fine model 8.26 with the 1/8 symmetry model 8.27 there is a slight difference in terms of impulse. It seems like the impulse for the fine fullscale model is increasing slightly at 0.8 ms. This impulse increment is probably caused by numerical errors in the contact algorithm, which can probably be fixed by increasing the number of quadrature points in the *constrained-lagrange-in-solid keycard. The results in terms of impulse are however very close, and if one disregards the impulse from the numerical errors it seems like convergence is attained.

The fact that convergence was attained for the reflected pressure seems to indicate that convergence of incident impulse is not a strict requirement for convergence.

Energy levels

The energy plots seem to indicate some weird behaviour. There are a few issues that must be pointed out. The peak in the energy plots corresponds to the expansion wave impacting the plate. There is a clear trend indicating that the total energy peak is increasing with stand off distance and with mesh refinement, figure 8.30, 8.31, 8.32 and 8.34. In the fine fullscale models and the 1/8 symmetry bias analysis, this value even exceeds the initial energy stored in the explosive for standoff distance 200mm and 250mm. The increasing energy trend for times exeeding 0.8 ms is stronger for the 150 mm and 200 mm stand off distances and increases with refined meshing. This is also reflected in the impulse which begin to increase for stand off distances 150 and 200 at roughly 0.8 ms for the fine fullscale analysis.

The sliding energy gives out the non physical energy in the compression springs asssociated with the contact algorithm. According to LS-DYNA support [33] a positive sliding energy of about 10% of the peak internal energy is acceptable. This criterion is met for all analysis in this section, even if one considers the maximum internal energy as the second peak observed in figures 8.30-8.32. For the biased model with the finer plate, the positive contact energy is neglible.

This negative energy is asssociated with leakage and can be seen to be increasing

with decreasing stand off distances. This is the case for both the fullscale models and the 1/8 symmetry bias model which gives out roughly the same negative sliding energy when scaling with a factor of 8. The negative sliding energy seems to be neglible when compared to the maximum of the internal energy for all considered models. This proably indicates that the models are well behaved when considering leakage.
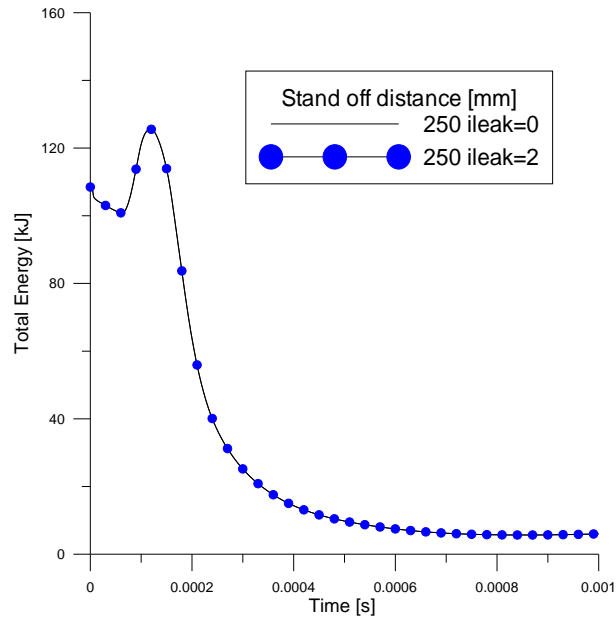
Figure 8.36: ileak=0 and ileak=2, standoff distance 250 mm, 1/8 bias symmetry model

To test this, the ileak=2 option in the *constrained-lagrange-in-solid keycard was turned on. This option ensures that particles stay on the right side of the contact interface, while removing the energy needed to enforce this with dampers parallel to the contact springs [26]. As expected, the results were exactely equal. This confirms that leakage is not a problem.

It is currently not known what the source of the increasing contact energy is. The contact energy levels seem to be well within the range suggested by LS-Support [33], but the energy peak still seems to be growing with stand off distance.

Finally, the fine fullscale model and the 1/8 symmetry model was prone to terminate the calculation. The scenario in which this occured was typically that the stable timestep decreased to zero and was followed by a segmentation error message. It is unclear what caused this, but the coarser fullscale mesh seemed to behave much better in this regard. The analysis did however perform long enough to attain pressure and impulse histories.

Chapter 9

Corpuscular method in IMPETUS

The main focus in this thesis has been blast on plates using bare charges. For protective stuctures and military aspects, explosions in sand, e.g. land mines, are very relevant. In this chapter, the results from two different numerical simulations using the non-linear finite element code IMPETUS, will be presented. The first considering bare charge, the second considering charge surrounded by dry sand.

9.1 Motivation for the Corpuscular method in IMPETUS

A discrete particle method, called the Corpuscular method, is a new method based on kinetic molecular theory, which seems to be promessing for solving close range blast simulations, especially when dealing with complex structures. The method is closely described in section 4.5.

The Corpuscular method is Lagrangian, which means that it does not suffer from advection errors that one experiences with an Eulerian formulation [28]. Compared to ALE, the Corpuscular method in IMPETUS is more evident/straight forward to use. There are less parameters to tweak, and it is less CPU demanding. An other great advantage with this method, is the possibility to run blast simulations including sand.

9.2   Bare charge

As for the analysis in LS-DYNA, different models were utilized; a 1/8 symmetry model, 1/4 symmetry model, and a fullscale model. The 1/8 symmetry model resulted in too large central deflection and reflected impulse, especially for stand off distance 150 mm, due to the reflecting boundary condition normally to the plate.

For the 1/4 symmetry model, the air and C4 were modelled inside a box with lengths $0.6x0.3x0.3m$, with reflecting boundary conditions a long the Z-axis. 30x30X1 solid 64-node 3rd order hexahedron elements with length ≈ 6.77 mm, was used for the plate. The edge nodes were constrained against translation in all directions, while the nodes along the symmetry edges were constrained against translation normally to the edge. The fullscale model was modelled as constrained in rotation and displacement along the plate edges.

9.2.1   Convergence study on reflected impulse

Several analysis using different amounts of particles were done, both for the 1/4 symmetry model and the fullscale model. The amount of air particles was initally set to be 10 times the amount of C4 particles. This ratio was rather arbitrary, since little studies on this subject have been done. As long as convergence is achieved, the ratio should be allright according to Lars Olovsson [27].

Three amounts of particles were tried out for both of the models for stand off distance 150 mm, table 9.1.

1/4 symmetry model		Fullscale model	
Air particles	C4 particles	Air particles	C4 particles
$1*10^5$	$1*10^4$	$4*10^5$	$4*10^4$
$3*10^5$	$3*10^4$	$1.2*10^6$	$1.2*10^5$
$5*10^5$	$5*10^4$	$2*10^6$	$2*10^5$

Table 9.1: Particles used in convergence tests
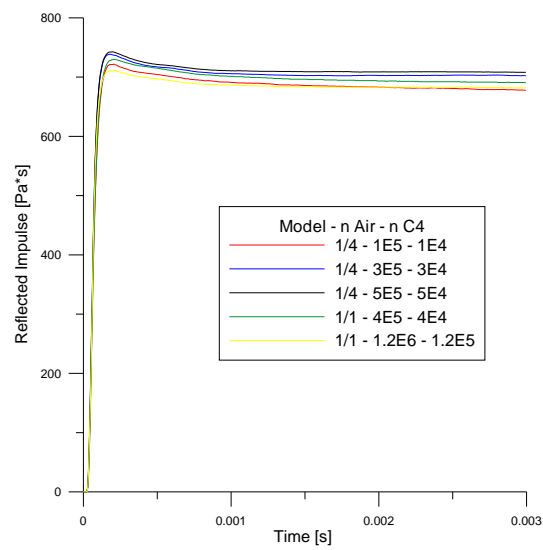
Figure 9.1: Study on Reflected Impulse, Stand off distance 150 mm, bare charge

Figure 9.1 shows that convergence is obtained. The 1/4 symmetry model corresponded very well with the fullscale model. It was therefore utilized in the further studies, using $3*10^5$ air particles and $3*10^4$ C4 particles. The following reflected impulses were obtained, figure 9.2.
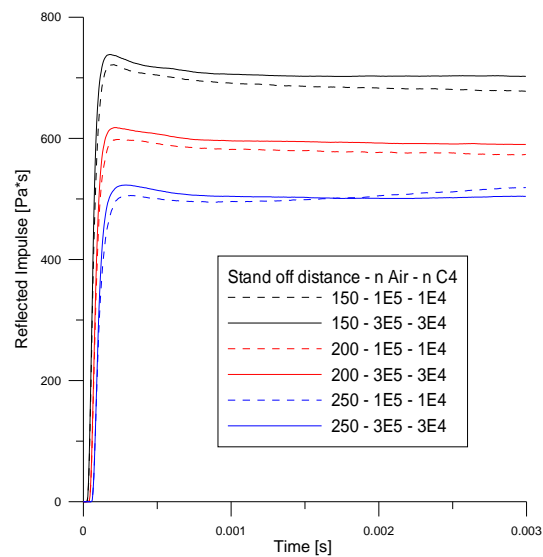
Figure 9.2: Reflected Impulse, 1/4 symmetry model, bare charge

9.2.2   Energy levels

The energy levels for the plate and C4, are plotted in figure 9.3 and 9.4. For comparison the results using the 1/4 symmetry model were multiplied by a factor of 4.
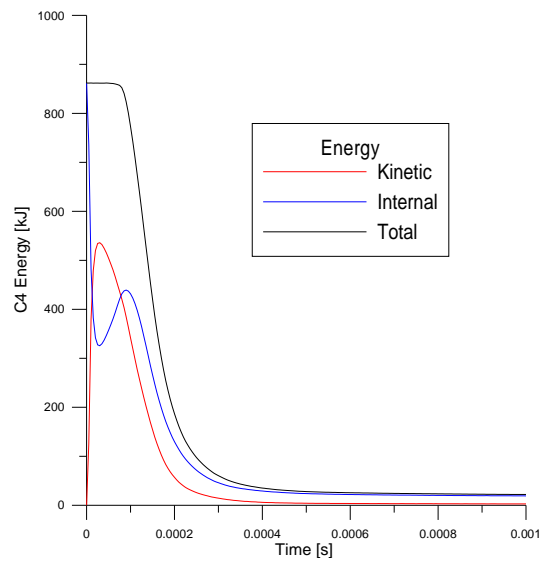
Figure 9.3: Energy C4, bare charge
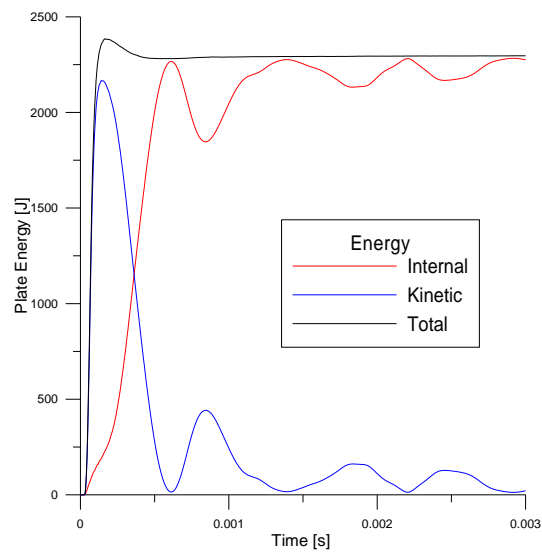
Figure 9.4: Plate energy, stand off distance 150 mm, bare charge
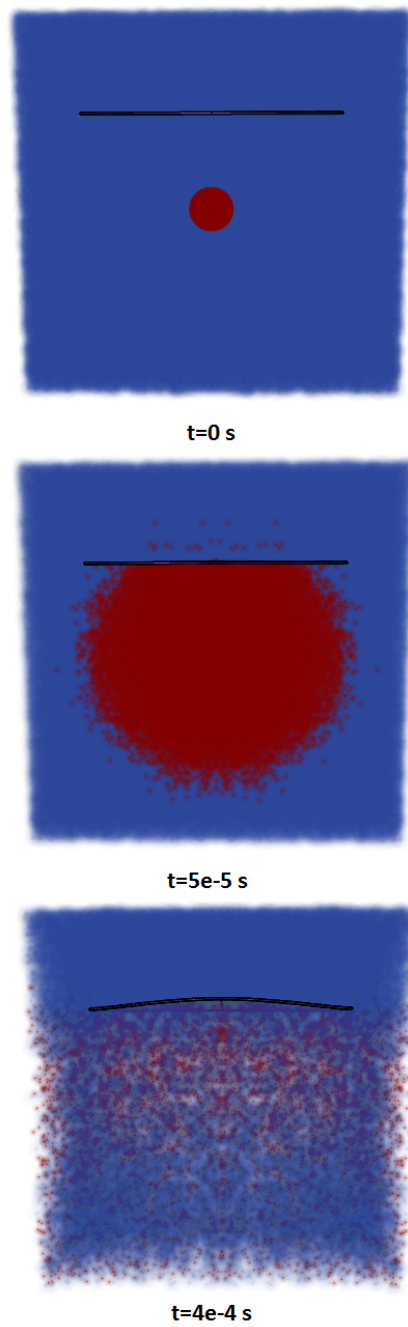
Figure 9.5: Plots from IMPETUS simulation, stand off distance 150 mm, bare charge

9.3   Charge surrounded by dry sand

In the simulations concidering charge surrounded by dry sand, the loading by air was assumed to be negligible [9]. The sand had an initial density of 1620 kg/m^3. The charge radius giving a weigth of 150 gram is 28.2 mm. To obtain a sand weight equal to 2.7 kg as in the experiments, the surrounding sand thickness wast set to 46.8 mm.

Sensitivity tests on the sand contact parameters **K** (contact stiffness) and μ (friction coefficient) were done by Olovsson et.al [9]. K=0.4 GN/m and μ=0.1 gave the best results. No further studies has been done on this subject. It was also concluded that the deflection of the plate was relatively insensitive to the number of particles [9]. The amount of C4 particles was set equal to the simulations with bare charge, $3 * 10^4$. The sand was modelled using $6 * 10^4$ particles.

9.3.1   Results

Reflected Impulses, energy levels and simulation plots describe the influence of dry sand in figure 9.6, 9.7, 9.8, and 9.9.

Figure 9.6: Reflected Impulse, 1/4 symmetry model, charge surrounded by dry sand
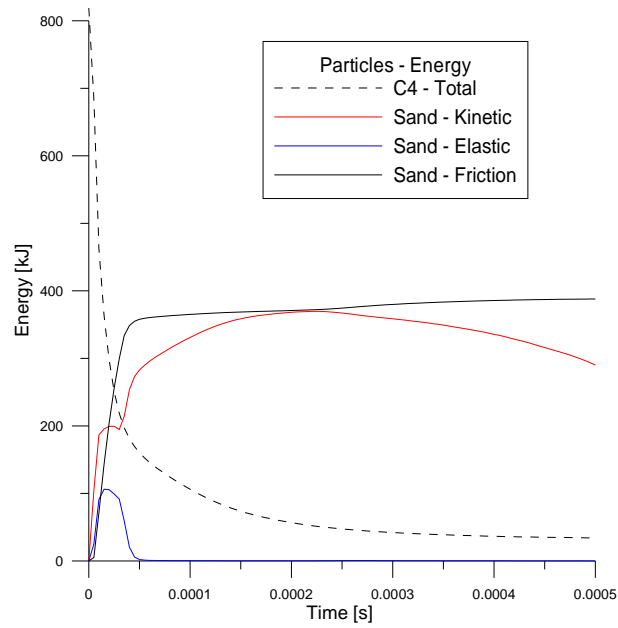
Figure 9.7: Energy, C4 and sand

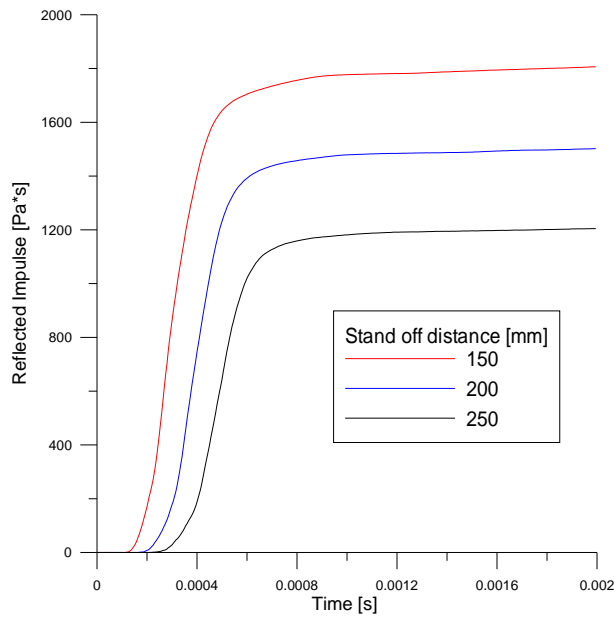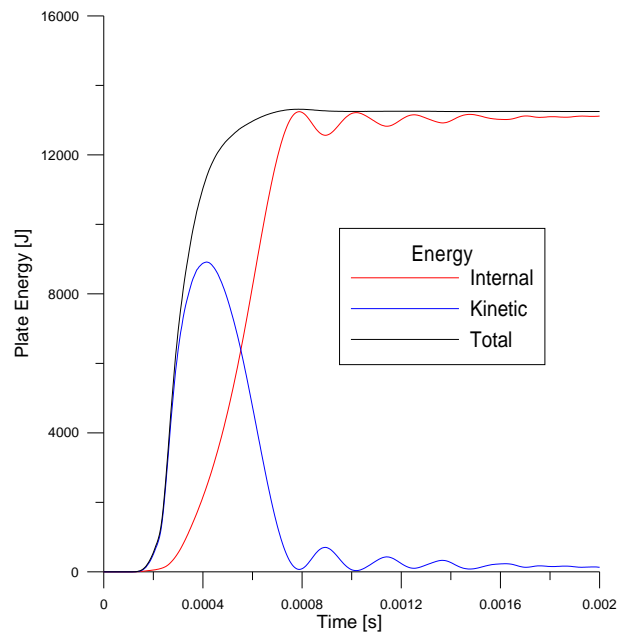Figure 9.8: Plate energy, stand off distance 150 mm, charge surrounded by dry sand
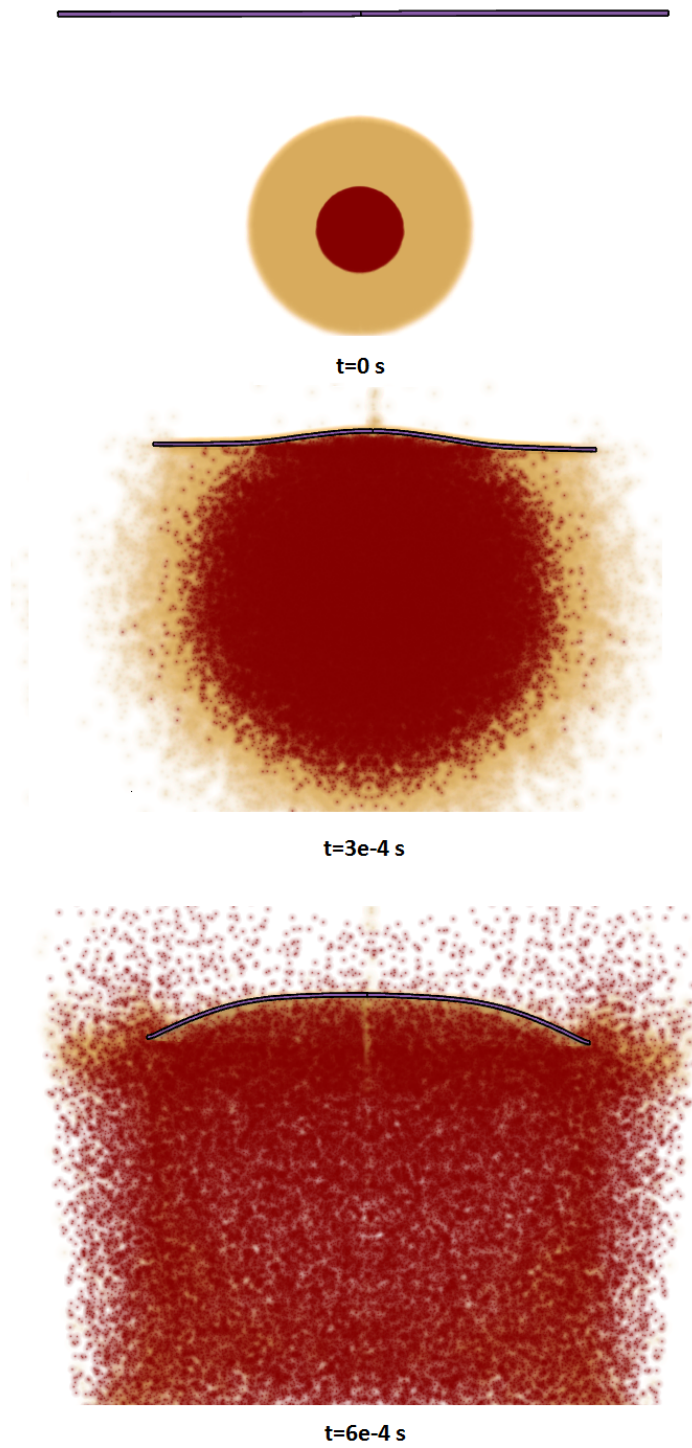
Figure 9.9: Plots from IMPETUS simulation, stand off distance 150 mm, charge surrounded by dry sand

9.4   Discussion

The reflected impulses for bare charge are within the expected size window, though smaller than ConWep values seen in 7.6. It is noticed that the reflected impulse is almost equal to the convergent values attained by the ALE method for stand off distance 150mm.

They differ at larger distances as the reflected impulse in IMPETUS decrease with increasing stand off distance, both for bare charge and charge surrounded by dry sand. The simulations showed that the influence of sand was huge, which was also seen in the experimental results. When adding sand, the reflected impulses were more than doubled, table 9.2.

Stand off distance	150 mm	200 mm	250 mm
Reflected Impulse Load Blast LS-DYNA	772	688	605
Reflected Impulse IMPETUS Bare charge	703	590	504
Reflected Impulse IMPETUS Dry sand	1806	1502	1205
Ratio IMPETUS Dry sand / Bare charge	2.57	2.55	2.39

Table 9.2: Reflected Impulses, Bare charge vs. Dry sand

There seem to be no problems concerning the energy. For the simulation with bare charge, figure 9.3, the C4 energy approaches zero when the blast is over. Likewise for the simulation with dry sand, figure 9.7. The most important energy source from the sand is friction. The plate energy plots show that the internal energy, due to plastic strain, is much more important for the simulations including sand, figure 9.4 and 9.8.

From the simulation plots, figure 9.9 and 9.5, one can see that the time period for the blast is longer for the simulation including dry sand.

A bare charge simulation with duration time 1 ms using the 1/4 symmetry model with $3 * 10^5$ air particles and $3 * 10^4$ C4 particles took about 30 minutes, while the sand simulation with duration time 2 ms took about 1 hour. Much less computational costfull than an ALE analysis using a fine mesh.

Chapter 10

Comparison

Three different numerical approaches have been used to simulate close range blast on plates with different stand off distances. The methods vary in complexity and computational costs, but they should somehow lead to approximately the same results, knowing that small deformations and no fracture were observed in the experiments. The permanent central deflection as well as the undamped central node displacement as a function of time and the final state of deformation, will be presented in this chapter.

The following parameters, table 10.1, were used to obtain the results presented in this chapter:

Numerical simulation	Model parameters
Load Blast	1/4 symmetry
	Plate: 60x60 shell elements, size 3.4 mm
ALE	1/1 symmetry
	Fluid: 60x60x60 solid elements, size 10 mm
	Plate: 20x20, size 20 mm
IMPETUS	1/4 symmetry
	Particles Air: $3 * 10^5$, Particles C4: $3 * 10^4$
	Particles Sand: $6 * 10^4$
	Plate: 30x30x1 solid elements, size 6.8 mm

Table 10.1: Parameters used for comparison of numerical simulations

10.1 Springback analysis

It is not a straight forward process to take out the permanent central deflection. Different techniques, based on the same principle, have been employed for every numerical method.

10.1.1   Load Blast LS-DYNA

A global viscous damping was utilized to avoid lasting oscillations, using the keyword *DAMPING-GLOBAL. The damping was put after 5 ms when the system was observed to be in steady-state, consequently it should not affect the plastic deformations. The total duration time was set to 15 ms to assure that oscillations disappeared. The damping was assumed to be more or less critical with the natural frequency measured from the time displacement plot.

10.1.2   ALE LS-DYNA

The same technique as for the Load Blast simulation could be used, but this requires a long time period to stop the oscillations, which is inconvenient for a CPU-demanding ALE simulation. Similar to Load Blast, a global viscous damping was utilized to obtain permanent deformations. First, a normal ALE analysis was done, in this case typically with a time period of 3 to 5 miliseconds. The results were investigated, to determine at which time the plastic strains remained constant, and if everything looked consistent with respect to impulse, leackage and energy levels. For stand off distance 150 mm, the time was found to be 2 ms, while 3.5 ms was used for stand of distances 200 mm and 250 mm.

The next step was to rerun the analysis using the new time period, including a new keyword; *INTERFACE-SPRINGBACK-LSDYNA. This gives out a file, dynain, which contains the plate's stresses, displacements and plastic strains. Then a new analysis, including this file, was done. Global viscous damping was turned on, elastic material was choosen, and the plate was reconstrained.

10.1.3   IMPETUS

The damping/springback analysis done in IMPETUS, is pretty simular to the one done in ALE. First, an analysis searching the appropriate time period was run, and then an analysis using this termination time. The *OUTPUT-INTERVAL function allows you to set the output interval for a model dump file, and decide which part set id, defining elements and nodes, that will be output to this restart file. Finally a springback analysis including the restart file was done, giving out the permanent deformed state of the plate. The Johnson Cook material model was used in the springback analysis.

In contrast to the springback analysis done in ALE which were run 2 and 3.5 ms, the time period in IMPETUS was set to be 1 ms for every stand off distance. This indicates the time where the transfer of impulse from the detonation products to the plate is ceased [9]. The simulations including dry sand were run 2 ms, due to longer impulse transfer period. Børvik et.al [9], in their studies on the same problem, used the same method to find the permanent central deflection.

10.2 Central node displacement
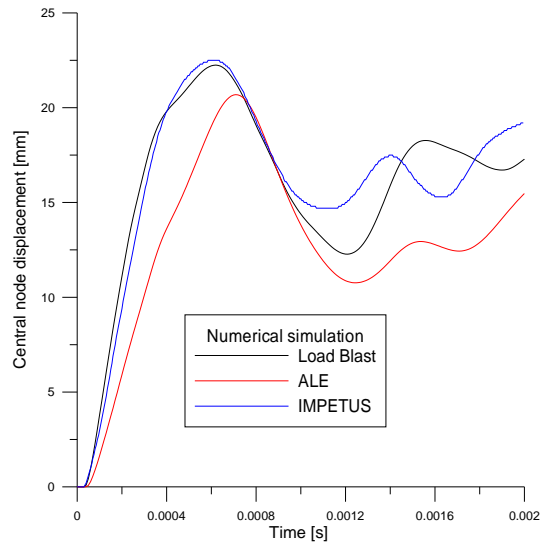
Figure 10.1: Central node displacement using different numerical approaches, stand off distance 150 mm
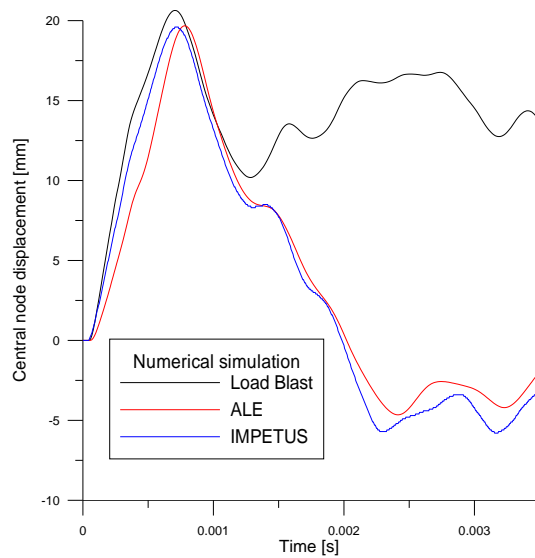
Figure 10.2: Central node displacement using different numerical approaches, stand off distance 200 mm
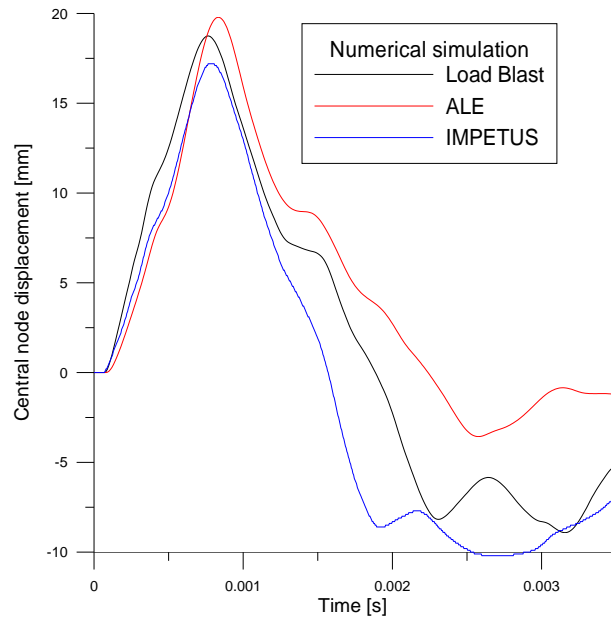
Figure 10.3: Central node displacement using different numerical approaches, stand off distance 250 mm
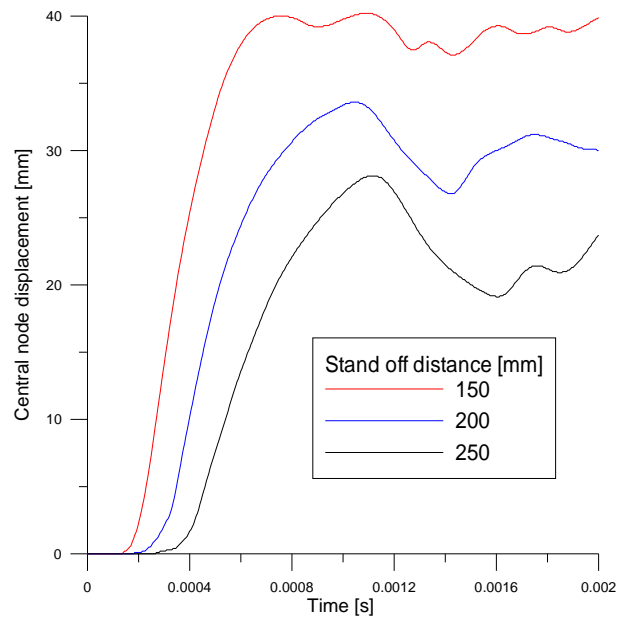
Figure 10.4: Central node displacement, charge surrounded by dry sand

For stand off distance 150 mm, figure 10.1, the oscillations stabilized around the permanent deflection for every numerical method, due to large plastic strain. The curves from IMPETUS and Load Blast follow each other perfectly in the beginning.

For stand off distance 200 mm, figure 10.2, the central node displacement was very similar for ALE and IMPETUS. They both obtained a negative deflection phase, while the Load Blast method oscillated around its permanent deflection. This confirms that conservative results may occur when using the Load Blast function.

For stand off distance 250 mm, figure 10.3, every numerical method obtained a negative deflection phase.

The simulations using dry sand in IMPETUS, figure 10.4, led to small oscillations stabilized around the permanent deflection, due to greater transfer of impulse.

10.3   Final state of deformation
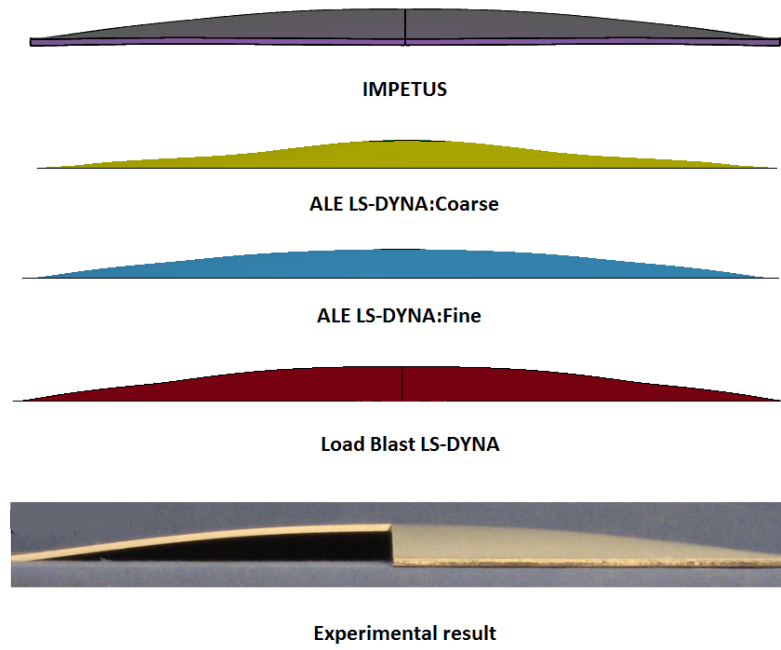
Figure 10.5: Final state of deformation, stand off distance 150 mm, bare charge
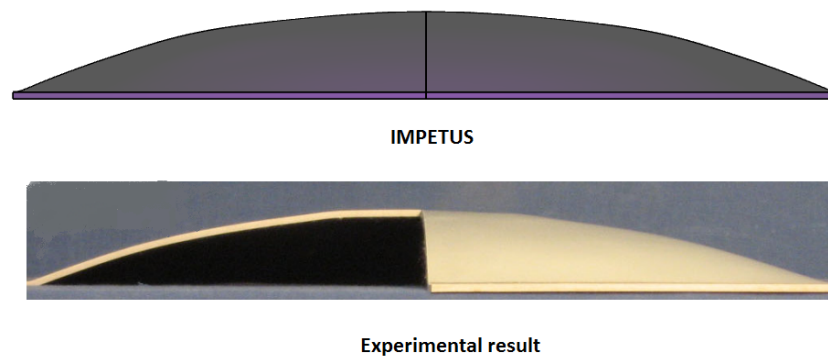
Figure 10.6: Final state of deformation, stand off distance 150 mm, charge surrounded by dry sand

The final state of deformation using IMPETUS corresponds very well with the experimental results. Load Blast and ALEfine correspond pretty good as well, while ALEcourse corresponds poorly.

10.4 Permanent central deflection

The main goal for this thesis was to compare the central deflection obtained from experimental results, with results obtained using different numerical methods. The results became as follows:

Stand off distance	150 mm	200 mm	250 mm
Experiments bare charge	17	12.7	11.3
Load Blast LS-DYNA	18.2	15.6	11.3
ALE LS-DYNA	15.6	11.9	12
IMPETUS bare charge	15.5	12.3	11.3

Table 10.2: Permanent central deflection, bare charge

Stand off distance	150 mm	200 mm	250 mm
Experiments Dry sand	38.5	26.8	18.5
IMPETUS Dry sand	38	29.2	22.9

Table 10.3: Permanent central deflection, charge surrounded by dry sand
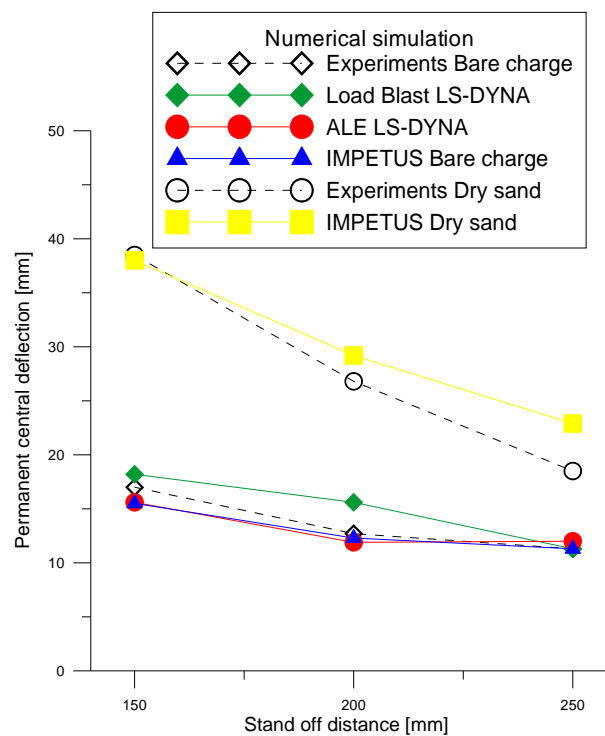
Figure 10.7: Permanent central deflection using different numerical approaches vs. experiments

Every numerical method gave relatively good results compared to experimental data. Especially for bare charge with standoff distance 250 mm, where IMPE-TUS and Load Blast are spot on the experimental results.

10.5   Discussion

In IMPETUS, it has also been tried to run the bare charge simulations further before doing a springback step. The same permanent central deflection was obtained for stand off distance 150 mm when using a termination time equal to 3 ms. On the other hand, for stand off distances 200 mm and 250 mm, using termination time 5 ms, the permanent central deflection decreased remarkebly, 2-3 mm. The negative deflection phase, figure 10.2 and 10.3, may explain why. Since the springback analysis in the IMPETUS code uses the Johnson cook material model in this thesis, it might attain plastic strains during the step. Since the springback analysis removes all intial velocities it might underpredict the plastic energy absorbed by the plate. When large velocities are present one must take care to ensure that the kinetic energy of the plate is close to zero before taking out the deformed plate.

For ALE, very good results with respect to central deflection were obtained when using the course mesh model. On the other hand, when using the finer mesh, the central deflection for stand off distance 200 mm and 250 mm got way to large compared with the experiments, due to increasing impulse with increasing stand off distance, figure 8.26.

Stand off distance	150 mm	200 mm	250 mm
Experiments bare charge	17	12.7	11.3
ALE LS-DYNA Course mesh	15.6	11.9	12
ALE LS-DYNA Fine mesh	16	15.7	16.9

Table 10.4: Permanent central deflection, course vs. fine mesh

It is therfore verified that the global response of the structure is in question with the current ALE blast model. The better fit for the coarser mesh can probably be explained by increasing attenuation for coarser meshes, section 4.2.8. Its likeliness to the experimental data is therefore caused by greater numerical dissipation rather than more accurate model description.

The computational time for the different methods vary quite a lot, table 10.5. For IMPETUS, the main simulation, giving out the restart file for springback analysis, is cheap in terms of computational time, while the springback analysis is pretty costful. For ALE, it is the other way around, especially for fine mesh. The springback analysis done in IMPETUS is costful, because the energy tolerance defining when equilibrium has been reached is set very low. This parameter can be changed without influence the results remarkebly. Table 10.5, do not contain springback times.

Simulation	Elapsed Time [min]	Duration of incident [ms]
Load Blast LS-DYNA	7	15
ALE LS-DYNA Course	56	2
ALE LS-DYNA Fine	1114	2
IMPETUS bare charge	27	1

Table 10.5: Elapsed time for different numerical simulations, stand off distance 150 mm

The compuational time speaks in great favour of IMPETUS, as the LS-DYNA ALE model uses almoast 42 times the amount of computational time when compared to IMPETUS. Since the models considered for ALE are fullscale and Impetus 1/4 scale it is slightly hard to compare the times. As simplification the LS-Dyna Elapsed time could be scaled by a factor of 1/4, and the the impetus code elapsed time is scaled by a factor of 2. Under these circumstances the impetus code still outperforms ALE with a factor of 5.15

Chapter 11

Concluding remarks

- The Lagrangian approach generally gives accurate results even at the shortest stand off distances used in this thesis. The Lagrangian model does however not account for FSI effects and it is probable that a larger charge with larger plate deformation, would yield more conservative results.

- Applying a uniform pressure directly as a function of the standoff distance of the closest point on the plate, will give severly conservative results at close standoff distance blast loading.

- Using solid elements, convergence was attained for the charge needed to induce failure mode IIa.

- The results obtained using the ALE method were very variable. In terms of reflected impulse, it was pretty much spot on when compared with IMPETUS for standoff distance 150 mm. For the larger distances the impulse was actually gradually getting bigger, which suggests numerical energy being created. It was therefore necessary to use a coarser mesh which seemed to increase less in reflected impulse. Probably because of the larger amount of numerical energy dissipation. However, the final deformed shape from the coarse analysis seemed to be quite different from that obtained from experimental data, figure 10.5. The fine analysis produced a deformation shape which was pretty much spot on.

- Calibrating the input parameters for the ALE method is extremely complex. The amount of functions and switches for tweaking are overwhelming. For someone with limited experience in this field, it is relatively hard to find the appropriate parameters to switch. The LS-DYNA keyword manual is also somewhat limited in its description of the parameters. The fact that accurate analysis requires compuational times roughly equal to a day, makes it hard to keep the train of thought in motion.

- Modeling the plate using 1/8 symmetry condtions, was appropriate for the ALE analyis in this thesis. It was found to give consistent values in terms of reflected impulse with the fullscale model. The reflective boundary condtions seemed to increase the pressure close to the reflective boundaries, but this effect was confined to a few elements. The increasing confinement of the blast might cause more errors if even smaller stand off distances are considered

- Turning on the E-factor in the *control-ale keycard gave too varying results in terms of pressure and impulse to be considered for using any further in the computational model.

- The IMPETUS analysis clearly gave the best correspondence with the experimental results. It was found to require a 1/4 symmetry condtion, since the boundaries behind the charge increases the amount of confinement, and therefore also the reflected impulse on the plate

- The springback analysis performed in IMPETUS was partially unreliable for the standoff distances 200mm and 250mm. This is speculated to be caused by the usage of the Johnson Cook material model in the springback step. The springback step zeros out the plate velocity and one might therefore possibly neglect the energy transfered from kinetic to plastic energy. The springback analysis seemed to give out great results when the springback step was taken out after 1 ms [9].

- The displacement time histories attained from Load Blast, ALE and particle method showed generally the same history in terms of displacement. The only exeption was the Lagrangian analysis at stand off distance 200 mm which differed by quite a lot.

Chapter 12

Further work

- ALE, change the contact formulatition from the Penalty method to the Kinematic constraint method.

- ALE, perform additional analysis using the Donor cell algorithm, and compare the results in terms of accuracy and computational times.

- ALE, turn off the automatic Penalty algorithm and use a custom defined Penalty stiffness.

- ALE, employ the enhanced Load Blast function in LS-DYNA (*load-blast-enhanced) to resolve the issues conserning increasing impulse in the ALE analysis (see chapter 2 and reference [30]).

- ALE, define a better mesh which fits the charge.

- ALE, IMPETUS, Load Blast, increase the mass of the intial charge in the analysis to spot the extend of increasing FSI effects.

- ALE and IMPETUS, determine the necessary charge to attain failure mode II. Because of FSI effects this could be larger than the charge determined in the Lagrangian section.

- ALE and IMPETUS, model the plate test rig more accurately. The plates in this paper are locked/suspended in air, while in reality they are constrained by a test rig. The interaction with the test rig might alter the results. In all analysis, fluid is allowed to flow around the edges of the plate and in behind it. This might be a source off error.

- IMPETUS, try to discern a more appropriate energy tolerance in the springback step. This step was found to use almost as long time as the particle analysis, and it is probable that convergence can be attained with lower tolerances.

- Do experiments with pressure sensors. This could make it easier to compare experimental results with numerical analysis.

Bibliography

[1] W.E. Baker. Explosion in air, 1973.

[2] W.E. Baker and P. Cox. *Explosion hazards and evaluation.* ELSEVIER SCI. PUBL. CO, P. O. BOX 211, 1000 AE AMSTERDAM, THE NETHERLANDS, 1982.

[3] T. Belytschko, W.K. Liu, and B. Moran. *Nonlinear finite elements for continua and structures.* Wiley New York, 2000.

[4] D. Benson. Lecture notes in Nonlinar Finite Element methods. 2008.

[5] A. Bouamoul and T.V. Nguyen-Dang. High explosive simulation using arbitrary Lagrangian-Eulerian formulation. 2008.

[6] T. Børvik. *An Introduction to Impact and Penetration Dynamics.* NTNU, SIMLab.

[7] T. Børvik, A.G. Hanssen, S. Dey, H. Langberg, and M. Langseth. On the ballistic and blast load response of a 20 ft ISO container protected with aluminium panels filled with a local mass-Phase I: Design of protective system. *Engineering Structures*, 30(6):1605–1620, 2008.

[8] T. Børvik, O.S. Hopperstad, T. Berstad, and M. Langseth. A computational model of viscoplasticity and ductile damage for impact and penetration. *European Journal of Mechanics/A Solids*, 20(5):685–712, 2001.

[9] T. Børvik, L. Olovsson, A.G. Hanssen, K. Dharmasena, H. Hansson, and H.N.G. Wadley. A discrete particle approach to simulate the combined effect of blast and sand impact loading of steel plates. *Currently Unpublished*, 2010.

[10] M.S. Chafi, G. Karami, and M. Ziejewski. Numerical analysis of blast-induced wave propagation using FSI and ALEmulti-material formulations. *International Journal of Impact Engineering*, 36(10-11):1269–1275, 2009.

[11] A.H. Clausen and T. Auestad. Experimental Set-up and Theoretical Considerations. 2002.

[12] V.S. Deshpande, R.M. McMeeking, H.N.G. Wadley, and A.G. Evans. Constitutive model for predicting dynamic interactions between soil ejecta and structural panels. *Journal of the Mechanics and Physics of Solids*, 2009.

[13] J.O. Hallquist. LS-DYNA theory manual. *Livermore software Technology corporation*, 3, 2006.

[14] J.O. Hallquist et al. LS-DYNA keyword user's manual. *Livermore Software Technology Corporation*, 2001.

[15] T.J. Holmquist and G.R. Johnson. Determination of constants and comparison of results for various constitutive models. *Le Journal de Physique IV*, 1(C3):3–3, 1991.

[16] D. Hyde. ConWep.exe. *US Army Corps of Engineers, Vicksburg, USA*, 1993.

[17] N. Jones, T.O. Uran, and S.A. Tekin. The dynamic plastic behavior of fully clamped rectangular plates. *International Journal of Solids and Structures*, 6(12):1499–1512, 1970.

[18] N. Kambouchev, L. Noels, and R. Radovitzky. Nonlinear compressibility effects in fluid-structure interaction and their implications on the air-blast loading of structures. *Journal of Applied Physics*, 100:063519, 2006.

[19] K.M. Mathisen. Course Notes TKT4197. 2009.

[20] S.B. Menkes and H.J. Opat. Broken beams- Tearing and shear failures in explosively loaded clamped beams. *Experimental Mechanics*, 13:480–486, 1973.

[21] M.J. Mullin and B.J. O'Toole. Simulation of energy absorbing materials in blast loaded structures. In *8th International LS-DYNA Users Conference*, 2004.

[22] S. Nemat-Nasser, W.G. Guo, and D.P. Kihl. Thermomechanical response of AL-6XN stainless steel over a wide range of strain rates and temperatures. *Journal of the Mechanics and Physics of Solids*, 49(8):1823–1846, 2001.

[23] A. Neuberger, S. Peles, and D. Rittel. Scaling the response of circular plates subjected to large and close-range spherical explosions. Part I: Air-blast loading. *International Journal of Impact Engineering*, 34(5):859–873, 2007.

[24] G.N. Nurick and G.C. Shave. The deformation and tearing of thin square plates subjected to impulsive loads–An experimental study. *International Journal of Impact Engineering*, 18(1):99–116, 1996.

[25] L. Olovsson. Corpuscular method for airbag deployment simulations in LS-DYNA. Technical report, ISBN 978-82-997587-0-3, May, 2007.

[26] L. Olovsson. Training class in ALE and fluid strucutre interaction. 2009.

[27] L. Olovsson. Private correspondence with Lars Olovsson, 2010.

[28] L. Olovsson, A.G. Hanssen, T. Børvik, and M. Langseth. A particle-based approach to close-range blast loading. *European Journal of Mechanics/A Solids*, 29(1):1–6.

[29] K.G. Rakvaag. *Master Thesis - Combined blast and fragment loading on plates*. NTNU, 2009.

[30] T.P. Slavik. A Coupling of Empirical Explosive Blast Loads to ALE Air Domains in LS-DYNA®. 2009.

[31] U.S. Army Engineer Waterways Experiment Station. *TM 5-855-1 - Fundamentals of Protective Design for Conventional Weapons.* U.S. Army, 1991.

[32] R.G Suavè and G.D. Morandin. Simulation of contact in finite deformation problems – algorithm and modelling issues®. 2004.

[33] LS-DYNA support. http://www.dynasupport.com/howtos/general/total-energy.

[34] G.I. Taylor. The pressure and impulse of submarine explosion waves on plates. *The scientific papers of GI Taylor*, 3:287–303, 1963.

[35] P.A. Urtiew and B. Hayes. Parametric study of the dynamic JWL-EOS for detonation products. *Combustion, Explosion, and Shock Waves*, 27(4):505–514, 1991.

[36] B. Van Leer. Towards the ultimate conservative difference scheme. IV. A new approach to numerical convection. *Journal of Computational Physics*, 23:276, 1977.

Appendix A

Matlab program used for mesh generation

```
%%%%%Ls-Dyna-Mesh-generator

%define position of node1$
x_0=0;
y_0=0;
z_0=0;

%number of elements%
n_nodes_x=75;
n_nodes_z=75;
n_nodes_y=75;

%connectivity_matrix%
c_matrix=zeros((n_nodes_x-1)*(n_nodes_y-1)*(n_nodes_z-1),10);
%part_id
P_id=2;
%lenght base element
base_lenght=0.002;
increment=1.03;
nodes=zeros((n_nodes_x)^3,6);
nodesnew=zeros((n_nodes_x)^3,6);
nodesnew2=zeros((n_nodes_x)^3,6);
x_vector=zeros(1,n_nodes_x);
y_vector=zeros(1,n_nodes_y);
z_vector=zeros(1,n_nodes_y);
nodesnew2s=zeros((n_nodes_x)^3,6);

%element_lenght_x%
for i=1:(n_nodes_x-1);
    if i == 1;
```

```
        x_vector(i+1)=x_vector(i)+base_lenght;
    else
        x_vector(i+1)=x_vector(i)+(x_vector(i)-x_vector(i-1))*increment;
    end
end

%element_lenght_x%
for i=1:n_nodes_x;
for j=0:n_nodes_y*n_nodes_z;
    nodes(i+(n_nodes_x*j),1)=i+n_nodes_x*j;
    nodes(i+(n_nodes_x*j),2)=x_vector(i);
end
end


%element_lenght_y%
for i=1:(n_nodes_y-1);
    if i == 1;
        y_vector(i+1)=y_vector(i)+base_lenght;
    else
        y_vector(i+1)=y_vector(i)+(y_vector(i)-y_vector(i-1))*increment;
    end
end

for h=0:n_nodes_y;
for i=1:n_nodes_y;
for j=1:n_nodes_y;
    nodes(h*(n_nodes_y)^2+j+(i-1)*(n_nodes_y),3)=y_vector(i);
end
end
end



for i=1:(n_nodes_x)^3;
    for j=1:6
        nodesnew2(i,j)=nodes(i,j);
    end
end

%element_lenght_z%
for i=1:(n_nodes_z-1);
    if i == 1;
        z_vector(i+1)=z_vector(i)+base_lenght;
    else
        z_vector(i+1)=z_vector(i)+(z_vector(i)-z_vector(i-1))*increment;
    end
end
```

```
for i=1:n_nodes_z;
for j=1:(n_nodes_z^2);
    nodesnew2(((i-1)*(n_nodes_z)^2)+j,4)=z_vector(i);
end
end

%connectivity%

for i=1:(n_nodes_x-1)*(n_nodes_y-1)*(n_nodes_z-1);
    c_matrix(i,1)=i;
    c_matrix(i,2)=2;
end

for i=1:(n_nodes_x-1)*(n_nodes_y-1)

    c_matrix(1+(n_nodes_x-1)*i,3)=1;
    c_matrix(1+(n_nodes_x-1)*i,4)=1;
    c_matrix(1+(n_nodes_x-1)*i,5)=1;
    c_matrix(1+(n_nodes_x-1)*i,6)=1;
    c_matrix(1+(n_nodes_x-1)*i,7)=1;
    c_matrix(1+(n_nodes_x-1)*i,8)=1;
    c_matrix(1+(n_nodes_x-1)*i,9)=1;
    c_matrix(1+(n_nodes_x-1)*i,10)=1;
end

for i=1:(n_nodes_x-1)

    c_matrix(1+(n_nodes_x-1)^2*i,3)=n_nodes_x+c_matrix(1+(n_nodes_x-1)^2*i,3);
    c_matrix(1+(n_nodes_x-1)^2*i,4)=n_nodes_x+c_matrix(1+(n_nodes_x-1)^2*i,4);
    c_matrix(1+(n_nodes_x-1)^2*i,5)=n_nodes_x+c_matrix(1+(n_nodes_x-1)^2*i,5);
    c_matrix(1+(n_nodes_x-1)^2*i,6)=n_nodes_x+c_matrix(1+(n_nodes_x-1)^2*i,6);
    c_matrix(1+(n_nodes_x-1)^2*i,7)=n_nodes_x+c_matrix(1+(n_nodes_x-1)^2*i,7);
    c_matrix(1+(n_nodes_x-1)^2*i,8)=n_nodes_x+c_matrix(1+(n_nodes_x-1)^2*i,8);
    c_matrix(1+(n_nodes_x-1)^2*i,9)=n_nodes_x+c_matrix(1+(n_nodes_x-1)^2*i,9);
    c_matrix(1+(n_nodes_x-1)^2*i,10)=n_nodes_x+c_matrix(1+(n_nodes_x-1)^2*i,10);
end

%initialization%
c_matrix(1,3)=1;
c_matrix(1,4)=2;
c_matrix(1,5)=c_matrix(1,4)+n_nodes_x;
c_matrix(1,6)=c_matrix(1,3)+n_nodes_x;
c_matrix(1,7)=c_matrix(1,3)+(n_nodes_x)^2;
c_matrix(1,8)=c_matrix(1,7)+1;
c_matrix(1,9)=c_matrix(1,8)+(n_nodes_x);
c_matrix(1,10)=c_matrix(1,7)+(n_nodes_x);

for i=1:(n_nodes_x-1)*(n_nodes_y-1)*(n_nodes_x-1)
c_matrix(i+1,3)=c_matrix(i+1,3)+c_matrix(i,3)+1;
c_matrix(i+1,4)=c_matrix(i+1,4)+c_matrix(i,4)+1;
```

```
c_matrix(i+1,5)=c_matrix(i+1,5)+c_matrix(i,5)+1;
c_matrix(i+1,6)=c_matrix(i+1,6)+c_matrix(i,6)+1;
c_matrix(i+1,7)=c_matrix(i+1,7)+c_matrix(i,7)+1;
c_matrix(i+1,8)=c_matrix(i+1,8)+c_matrix(i,8)+1;
c_matrix(i+1,9)=c_matrix(i+1,9)+c_matrix(i,9)+1;
c_matrix(i+1,10)=c_matrix(i+1,10)+c_matrix(i,10)+1;
end

%CONSTRAINTS%

for i=1:n_nodes_x*n_nodes_y*n_nodes_z;
    if nodesnew2(i,2)==0;
       nodesnew2(i,5)=1;
    end
    if nodesnew2(i,3)==0;
       nodesnew2(i,5)=2;
    end
    if nodesnew2(i,4)==0;
       nodesnew2(i,5)=3;
    end
end

for i=1:n_nodes_x*n_nodes_y*n_nodes_z;
    if nodesnew2(i,2)==0 & nodesnew2(i,3)==0;
       nodesnew2(i,5)=4;
    end
    if nodesnew2(i,2)==0 & nodesnew2(i,4)==0;
       nodesnew2(i,5)=6;
    end
    if nodesnew2(i,3)==0 & nodesnew2(i,4)==0;
       nodesnew2(i,5)=5;
    end
end
    nodesnew2(1,5)=7;

DLMWRITE('meshbias.txt',nodesnew2,'precision',9)
DLMWRITE('meshbias.txt',c_matrix,'-append','precision',9)
```

Appendix B

Keyword files

B.1 LS-DYNA keyword file for the load blast analysis in chapter 7 and 10

```
*keyword
$
$
$Includes plate mesh
*include
PlateShell60x60.k
$
$
*constrained_global
7,7,1,0.203,0,0
7,7,2,0,0.203,0
2,6,2,0,0,0
1,5,1,0,0,0
$
$
$Duration of incident
*control_termination
0.015
$
$
$Two random curves must be defined, for the LOAD_BLAST function to work
*define_curve
1
0,0
1,1
*define_curve
2
0,0
```

```
1,0
$
$
$Defines a set for load application
*set_shell_general
1
part,1
$
$
$Defines a blast curve
*load_blast
0.1785,0,0,0.15,0


$
$
$The blast curve is saved as -2, and is loaded to the shell
*load_shell_set
1,-2
$
$
$Global damping curve
*define_curve
5
0.005,1250
0.015,1250
$
$
*damping_global
5
$
$
$Parameters to the modified Johnson Cook Model
*mat_107
$MID RO E PR BETA XSI CP ALPHA
1,8060,1.95e11,0.3,0,0.9,500,1.5e-5
$EODOT Tr Tm TO FLAG1 FLAG2
1e-3,296,1700,293,0,1
$A B N C m
4.10e8,19.02e8,0.82,0.024,1.03
$Q1 C1 Q2 C2
0,0,0,0
$DC WC
1,235.7e6
$TC TAUC
1650,1e20
$
$
$Defines section, integration points, and thickness
*section_shell
1,,,5
```

```
3.4e-3
$
$
$Allows thinning of shell
*control_shell
,,,1
$
$
$Defines part and links it to section and material
*part
plate
1,1,1
$
$
$Output
*database_nodout
5e-6
$
$
*database_glstat
5e-6
$
$
*database_binary_d3plot
1e-4,0
$
$
$Hourglass energy computed
*control_energy
2
$
$
$Second order objective stress update
*control_accuracy
1,4
$
$
*end
```

B.2   LS-DYNA keyword file for the ALE analysis in chapter 8

```
*KEYWORD 400000000
$
$
$Includes plate mesh
*INCLUDE
PlateShell150Coarse.k
$
$
$Changes the node and element numbers
*INCLUDE_TRANSFORM
CubeCoarse.k
900000,900000


$Duration of incident
*CONTROL_TERMINATION
2E-3
$
$
$Scale factor 0.67 for high explosive
*CONTROL_TIMESTEP
 ,0.67
$
$
$Set global control parameters for the ALE calculations
*CONTROL_ALE
$Lagrange, 1 cycle between advections, Van Leer advection
0,1,2
 , , , , , ,1.013E5
$
$
*ALE_MULTI-MATERIAL_GROUP
$TNT: ID, part - AMMGID 1
2,1
$AIR: ID, part - AMMGID 2
3,1
$
$
$Allows the modelling of the detonation of C4
*MAT_HIGH_EXPLOSIVE_BURN
2,1601,8190,2.8E10,2,1,1
$
$
$Equation of state for C4
```

```
*EOS_JWL
2,5.9750E11,13.9E9,4.5,1.5,0.32,8.7E9
$
$
$Air at 20 degrees
*MAT_NULL
3,1.204
$
$
$Equation of state for Air
*EOS_LINEAR_POLYNOMIAL
3,0,0,0,0,0.4,0.4,0
2.5325E5,1
$
$
$Parameters to the modified Johnson Cook Model
*MAT_107
$MID RO E PR BETA XSI CP ALPHA
4,8060,1.95e11,0.3,0,0.9,500,1.5e-5
$EODOT Tr Tm T0 FLAG1 FLAG2
1e-3,296,1700,293,0,1
$A B N C m
4.10e8,19.02e8,0.82,0.024,1.03
$Q1 C1 Q2 C2
0,0,0,0
$DC WC
1,235.7e6
$TC TAUC
1650,1e20
$
$
$1 point ALE multi-material element C4
*SECTION_SOLID
2,11
$
$
$1 point ALE multi-material element Air
*SECTION_SOLID
3,11
$
$
$Defines number of integration points and thickness to the plate
*SECTION_SHELL
4,,,5
0.0034
$
$
$Allows thickness change
*CONTROL_SHELL
,,,1
```

```
$
$
$Assigns section, material, and EOS to C4
*PART

2,2,2,2
$
$
$Assigns section, material, and EOS to Air
*PART

3,3,3,3
$
$
$Assigns section and material to Plate
*PART

4,4,4
$
$
$Defines volume fractions of various ALE multi-material groups
*INITIAL_VOLUME_FRACTION_GEOMETRY
2,1,2
6,0,1
0,0,0,0.02818
$
$
$Defines the detonation of C4
*INITIAL_DETONATION
2,0,0,0,0
$
$
$Fluid-Structure Interaction
*CONSTRAINED_LAGRANGE_IN_SOLID
4,2,1,1,4,4,2


$
$
$Part set for springback function
*SET_PART
1
4
$
$
$Creates restart file for damping analysis
*INTERFACE_SPRINGBACK_LSDYNA
1,100,2
$
$
```

```
$Output
*DATABASE_BINARY_D3PLOT
1E-4
$
$
*DATABASE_GLSTAT
1E-6
$
$
*DATABASE_FSI
1E-6
2,4,1
$
$
*DATABASE_HISTORY_NODE
221
$
$
*DATABASE_NODOUT
1E-5
$
$
$Includes hourglass energy
*CONTROL_ENERGY
2
$
$
*END
```

B.3   IMPETUS keyword file for the analysis in section 9.2

```
Includes plate mesh
*INCLUDE
150plate30x30.k
$
$
$Duration of incident, and time step scale factor
*TIME
1.0e-3,0.67
$
$
$Output plots, ascii data, and restart file
*OUTPUT_INTERVAL
5.0e-5, 5.0e-6, 5.0e-5, 1
$
$
$Parameters to the modified Johnson Cook Model
*MAT_JC
1, 8060, 1.95e+11, 0.3
4.1e+8, 19.02e+8, 0.82, 0.024, 1.03, 293.0, 1700.0, 0.001
500,0.9, 0, 0, 0, 0, 0, 235.7e6
1
$
$
*SET_PART
1
1
$
$
$Links the part to the material
*PART
1, 1
$
$
$Changes element polynomial order
*CHANGE_P-ORDER
P, 1, 3
$
$
$Set up blast loading of a FE-structure with air, soil and high explosive
*PBLAST
P, 1, 300000, 0, 30000, 0, 1, 2
1, 0, 1, 0, 0, 0
1, 0, 2, 0.0, 0.0, 0.0, 0.0
$
$
```

```
$Global domain
*GEOMETRY
1, 1
0.0, 0.0, -0.3, 0.3, 0.3, 0.3
$
$
$High explosive domain
*GEOMETRY
2, 2
0.0, 0.0, 0.0, 0.0282
$
$
$Central node displacement
*OUTPUT_NODE
N,1
*END
```

B.4 IMPETUS keyword file for the analysis in section 9.3

```
Includes plate mesh
*INCLUDE
150plate30x30.k
$
$
$Duration of incident, and time step scale factor
*TIME
2.0e-3,0.67
$
$
$Output plots, ascii data, and restart file
*OUTPUT_INTERVAL
5.0e-5, 5.0e-6, 5.0e-5, 1
$
$
$Parameters to the modified Johnson Cook Model
*MAT_JC
1, 8060, 1.95e+11, 0.3
4.1e+8, 19.02e+8, 0.82, 0.024, 1.03, 293.0, 1700.0, 0.001
500,0.9, 0, 0, 0, 0, 0, 235.7e6
1
$
$
*SET_PART
1
1
$
$
$Links the part to the material
*PART
1, 1
$
$
$Changes element polynomial order
*CHANGE_P-ORDER
P, 1, 3
$
$
$Set up blast loading of a FE-structure with air, soil and high explosive
*PBLAST
P, 1, 0, 60000, 30000, 0, 1, 2
1, 0, 1, 0, 0, 0
1, 3, 2, 0.0, 0.0, 0.0, 0.0
$
$
```

```
$Global domain
*GEOMETRY
1, 1
0.0, 0.0, -0.3, 0.3, 0.3, 0.3
$
$
$High explosive domain
*GEOMETRY
2, 2
0.0, 0.0, 0.0, 0.0282
$
$
$Soil domain
*GEOMETRY
3, 2
0.0, 0.0, 0.0, 0.075
$
$
$Central node displacement
*OUTPUT_NODE
N,1
*END
```

B.5   ALE springback analysis in chapter10

```
KEYWORD 500000000
$
$
$Includes restart file
*INCLUDE
dynain.k
$
$
$Parameters to elastic model
*MAT_ELASTIC
$MID RO E PR
1,8060,1.95e11,0.3
$
$
*CONSTRAINED_GLOBAL
7,7,1,0.203,0,0
7,7,2,0,0.203,0
7,7,2,0,-0.203,0
7,7,1,-0.203,0,0
$
$
*CONTROL_TERMINATION
20E-3
$
$
*DAMPING_GLOBAL
0,1000
$
$
*SECTION_SHELL
1,,,5
0.0034
$
$
*CONTROL_SHELL
,,,1
$
$
$Assigns part to section and material
*PART

4,1,1
$
$
$Output
*DATABASE_HISTORY_NODE
```

```
221
$
$
*DATABASE_NODOUT
1E-4
$
$
*DATABASE_BINARY_D3PLOT
4E-3
$
$
*END
```

B.6   IMPETUS springback analysis in chapter10

```
$Includes the restart file from earlier analysis
*INCLUDE
impetus.restart1
$
$
$Duration of incident, and time step scale factor
*TIME
1.0e-6,0.9
$
$
$Output plots, ascii data
*OUTPUT_INTERVAL
1.0e-3, 1.0e-4
$
$
$Springback function that uses dynamic relaxation and explicit time integration
*SPRINGBACK
1.0e-5,5.0e-6,0.999
$
$
$Parameters to the modified Johnson Cook Model
*MAT_JC
1, 8060, 1.95e+11, 0.3
4.1e+8, 19.02e+8, 0.82, 0.024, 1.03, 293.0, 1700.0, 0.001
500,0.9, 0, 0, 0, 0, 0, 235.7e6
1
$
$
$Links the part to the material
*PART
1, 1
$
$
$Central node displacement
*OUTPUT_NODE
N,1
*END
```